Reconfigurable Satellite Constellations for Geo-spatially Adaptive Earth Observation Missions

by

Sung Wook Paek

Submitted to the Department of Aeronautics and Astronautics
in partial fulfillment of the requirements for the degree of

Master of Science

at the

Massachusetts Institute of Technology

May 2012

Reconfigurable Satellite Constellations for Geo-spatially Adaptive Earth Observation Missions

by

Sung Wook Paek

Bachelor of Science in Aerospace Engineering and
Electrical Engineering (2010)
Korea Advanced Institute of Science and Technology

Submitted to the Department of Aeronautics and Astronautics
in partial fulfillment of the requirements for the degree of

Master of Science in Aeronautics and Astronautics

at the

MASSACHUSETTS INSTITUTE OF TECHNOLOGY

May 2012

Author.....
Department of Aeronautics and Astronautics
May 24, 2012

Certified by.....
Olivier L. de Weck
Associate Professor of Aeronautics and Astronautics
Associate Professor of Engineering Systems
Thesis Supervisor

Accepted by.....
Eytan H. Modiano
Associate Professor of Aeronautics and Astronautics
Chair, Committee on Graduate Students

Reconfigurable Satellite Constellations for Geo-spatially Adaptive Earth Observation Missions

by

Sung Wook Paek

Submitted to the Department of Aeronautics and Astronautics
on May 24, 2012 in partial fulfillment of the requirements for the degree of
Master of Science in Aeronautics and Astronautics

Abstract

Continuously increasing demand for Earth observation in atmospheric research, disaster monitoring, and intelligence, surveillance and reconnaissance (ISR) has been met by responsive architectures such as unmanned aerial systems (UAS) or artificial satellites. Space-based architectures can provide non-dominated design solutions on the utility-cost curve compared to alternate architectures through the use of two approaches: (1) reducing satellite manufacturing and launch costs and (2) introducing reconfigurability to the satellite constellations. Reconfigurable constellations (ReCons) enable fast responses to access targets of interest while providing global monitoring capability from space. The wide-area coverage and fast responses provided ReCon can complement high-resolution imagery provided by UAS. A newly proposed ReCon framework improves the model fidelity of previous approaches by utilizing Satellite Tool Kit (STK) simulations and Earth observation mission databases.

This thesis investigates the design and optimization of ReCon in low Earth orbits. A multi-disciplinary simulation model is developed, to which optimization techniques are applied for both single-objective and multi-objective problems. In addition to the optimized baseline ReCon design, its variants are also considered as case studies. Future work will potentially co-optimize ReCon and UAS-like systems.

Thesis Supervisor: Olivier L. de Weck
Title: Associate Professor of Aeronautics and Astronautics and Engineering Systems

The author appreciates the financial support for this research from Samsung Scholarship.

Acknowledgments

First of all, I would like to express special gratitude to Professor Olivier de Weck and Professor David Miller for their guidance.

It was a great opportunity for me to participate in the ReCon project, which is a continuation of previous work initiated by Josef Bogosian, Rebecca Myers, and Benjamin Werner. In developing the "new" ReCon framework, Robert Legge and Matthew Smith did wonderful work and always inspired me.

Sydney Do has provided me with thoughtful advice and assistance throughout my graduate life at MIT. I owe Phillip Cunio and Erik Stockham special thanks for their help in preparing this project for the research evaluation part of my qualifying exams. I also thank Andre Chen, Hongseok Cho, Jeong Hwan Jeon, Been Kim, Jamin Koo, Hanbong Lee, In Hwan Lee, Sang-il Lee, Jun-Geun Park, and Rezy Pradipta for their support. Sunny Ahn, Mr. Robert Irwin, aforementioned Robert Legge, and Matthew Smith helped me finalize this thesis.

I also feel grateful to Professor Jaemyung Ahn, Professor Hyochoong Bang, and Professor Han-Lim Choi who have encouraged me since the beginning of my master's program.

My master's program was supported by the Samsung Scholarship, and I truly appreciate the sponsorship that enabled me to accomplish the first half of my graduate program without financial difficulties. Also, the Educational Partnership Agreement between MIT and Analytical Graphics, Inc. was crucial in allowing the capabilities of Satellite Tool Kit to be used in this research.

Last but not least, I would like to thank my parents, Mr. Bong Hyun Paek and Ms. Bong Sun Moon, and my brother, Sung Hoon Paek, for their unconditional love and support. I dedicate my thesis to them.

Contents

List of Figures

List of Tables

Nomenclature

Abbreviations

ATK	Alliant Techsystems Inc.
AWS	Adaptive Weighted Sum
COPV	Composite Overwrapped Pressure Vessel
DMC	Disaster Monitoring Constellation
DOE	Design of Experiment
DSM	Design Structure Matrix
EADS	European Aeronautic Defense and Space Company
EELV	Evolved Expendable Launch Vehicle
ESPA	EELV Secondary Payload Adapter
FoR	Field of Regard
GA	Genetic Algorithm
GEO	Geostationary Earth Orbit
GLONASS	Global Navigation Satellite System
GOM	Global Observation Mode
GPS	Global Positioning System
GSD	Ground Sample Distance
HEO	Highly Elliptical Orbit
IGSO	Inclined Geosynchronous Orbit
ISL	Inter-Satellite Link
ISR	Intelligence, Surveillance and Reconnaissance
KH	Key Hole (reconnaissance satellites)
LEO	Low Earth Orbit
LFC	Lattice Flower Constellation
LHS	Latin Hypercube Sampling
MATLAB	Matrix Laboratory

MEO	Medium Earth Orbit
MOGA	Multi-objective Genetic Algorithm
MOO	Multi-objective Optimization
MSDO	Multidisciplinary System Design Optimization
NASA	National Administration of Space and Aeronautics
NRGT	Non-repeating Ground Track
NSGA-II	Non-dominated Sorting Genetic Algorithm-II
OTA	Optical Telescope Assembly
PMD	Propellant Management
PSF	Point Spread Function
ReCon	Reconfigurable Constellation
RAAN	Rising Ascension of Ascending Mode
RGT	Repeating Ground Track
ROM	Regional Observation Mode
SA	Simulated Annealing
SAR	Synthetic Aperture Radar
SMAD	Space Mission Analysis and Design
SOC	Streets of Coverage
SOO	Single Objective Optimization
SRP	Solar Radiation Pressure
SSO	Sun-synchronous Orbit
SSRGT	Sun-synchronous Repeating Ground Track
STK	Satellite Tool Kit
UAS	Unmanned Aerial System
UAV	Unmanned Aerial Vehicle

Roman Symbols

a	Semi-major axis (km)
A	Satellite cross section area (m^2); Altitude difference (km)
C	Refinement coefficient (AWS)
C_D	Drag constant (-)

c	Scale factor for constraint violations in fitness function (-)
d	Orbit plane regression in a single satellite period (km)
D	Distance between closest equator crossings of RGT and NRGT orbits (km)
e	Orbit eccentricity (-)
E	Intermediate variable for Lattice Flower Constellations (-); System energy in simulated annealing (J)
f	Fitness or objective
F	Phasing parameter for Walker Constellations and Flower Constellations; Fitness or objective
g	Gravitational acceleration (m/s^2); Global gain for constraint violations in fitness function (-)
G	Universal gravitational constant ($m^3kg^{-1}s^{-2}$)
h	Altitude (km)
i	Orbit inclination (°)
I	Sorted set (NSGA-II)
I_{sp}	Specific impulse (s)
J	Figure of merit (-)
J_2	Gravity model coefficient (-)
L	Latitude (°); Design life (year)
m	Satellite subsystem mass (kg)
M	Mean anomaly (°)
n	Mean motion (rad/s)
N	RGT ratio (-)
P	Number of orbit planes (-); Acceptance probability in simulated annealing (-)
R	Angle of regard (°)
R_E	Earth radius (km)
R_S	Slant range (km)
s	Scale factor for objectives in fitness function (-)
S	Number of satellites per plane (-)
T	Period (second for nodal period; day for reconfiguration time); Total number of satellites in Walker constellations (-); System temperature in simulated annealing (K)

V	Orbital velocity (km/s); Satellite volume (m^3)
w	Weight for objectives in fitness function (-)

Greek Symbols

α_i	Relative weighting for objectives in adaptive weighted sum at the i^{th} point
δ_j	Offset distance in normalized objective space (-)
ε	Propulsion subsystem non-tank mass to propellant mass ratio (-)
ϵ_Θ	Resonance parameter (-)
ζ	Propellant mass to satellite mass ratio (-)
η	Field of regard (°)
θ_r	Angular resolution (rad)
λ	Wavelength (m)
μ	Gravitational constant (km^3/s^2)
ν	True anomaly (rad)
ξ	Intermediate variable for J_2 perturbation
τ	RGT period ratio (-)
Υ	Vernal equinox
φ	Longitude (°)
ϕ_{fpa}	Flight path angle (rad)
ω	Argument of perigee (°)
Ω	Rising ascension of ascending node (°)

Subscripts, Superscripts, and Operators

$(\cdot)_D$	Day
$(\cdot)_E$	Earth
$(\cdot)_G$	Greenwich
$(\cdot)_k$	Iteration step
$(\cdot)_P$	Period
$(\cdot)_S$	Satellite
$(\cdot)^U$	Utopia point
$(\cdot)^N$	Non-utopia point

$(\cdot)^*$	Optimal value
$(\cdot)'$	First derivative
$\dot{(\cdot)}$	First derivative with respect to time
$\overline{(\cdot)}$	Normalized value
$A \circ B$	Entrywise product in matrix multiplication

Definitions

Model

A model is a mathematical construct that has the ability to predict the behavior of a real system under a set of defined operating conditions and simplifying assumptions.

Forward Problem

A forward problem is a model that relates a design vector to a scalar objective or an objective vector.

Figure of Merit

A figure of merit is a quantity that characterizes the performance of a design solution.

Penalty

A penalty is a "handicap" added to the figure(s) of merit, and its proportional to the magnitude of a given constraint violation. The penalty accounts for the fact that the performance of a design solution exceeding the constraint boundaries are either undesirable or difficult to predict with the given forward problem.

Objective

An objective is a quantity that an optimizer tries to minimize or maximize. The term "fitness" is used interchangeably here. An objective is obtained from a fitness function that is a summation of the scaled/weighted figure(s) of merit and the penalty.

Chapter 1

Introduction

Earth observation, also called Earth remote sensing, has made it possible to collect information about objects or areas which are inaccessible or dangerous without direct contacts with them [1, 2] by means of active or passive sensors operating in various wavelengths of the electromagnetic spectrum. Continuously increasing demand for Earth observation in atmospheric research, disaster monitoring, and intelligence, surveillance and reconnaissance (ISR) can be met by responsive architectures such as unmanned aerial systems (UASs) or artificial satellites. The two architectures, air-based and space-based, have distinguishing characteristics in terms of access and imagery, so they have the potential to complement each other. This thesis focuses on optimization of the space-based architecture, by means of a reconfigurable constellation (ReCon) where satellites can change their orbital characteristics to adjust global and regional observation performance. The framework and conclusions will form one building block of a greater study in future, namely co-optimization of space-based architecture and air-based architecture.

1.1 Background and Motivation

Compared to the capability of UAS to continuously acquire high resolution imagery, satellite constellations can provide the following advantages [3].

1) Wide global coverage: A satellite in low Earth orbit (LEO) completes an orbit around the Earth on the order of hours and within several days a constellation of satellites

can cover the entire portion of the Earth's surface whose latitude is less than or equal to the orbit inclination.

2) Frequent regional access: If a satellite has repeating ground tracks (RGT), it repeatedly follows paths stationary relative to the Earth, drastically increasing coverage over a specific location. Although the coverage is not continuous, the duration of regular accesses can be readily extended as long as weeks or months, which would demand considerable overhead for UAS due to survivability issues, frequent mission handovers, and finiteness of on-board consumables such as fuel.

These dual objectives of global coverage and targeted coverage can be met by a single system by introducing reconfigurability to satellite constellations, leading to the concept of a reconfigurable constellation (ReCon). Wide global coverage is obtained when satellites are in non-repeating ground track (NRGT) orbits in the global observation mode (GOM); frequent regional access is obtained when satellites are in repeating ground track (RGT) orbits in the regional observation mode (ROM). The ground tracks of two modes are depicted Figure 1-1, which was generated using Satellite Tool Kit (STK) [4]. For an orbit with 28.5° inclination, a 482 km altitude achieves a "15/1" RGT where a satellite orbits around the Earth 15 times a day, visiting anywhere along its path at least once a day, as shown Figure 1-1(b). If the altitude is deviated from the baseline RGT, ground tracks are evenly spread out to cover the latitude band between 28.5°N and 28.5°S, as shown Figure 1-1(a). Satellites can change altitudes efficiently by the Hohmann transfer and can change planes naturally by orbital precession.

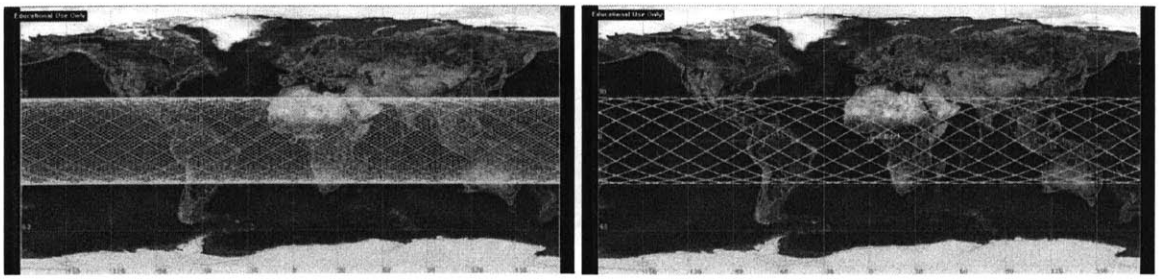

(a) Non-repeating ground track (b) 15/1 Repeating Ground Track

Figure 1-1: Paths of Non-repeating Ground Track and Repeating Ground Track of a Satellite Propagated over One Week [4]

There are several Earth observation constellations currently deployed on orbit. Figure 1-2 illustrates NASA's A-Train that observes the atmosphere and surface of Earth [5]; it name comes from the fact that these satellites crosses the equator around 1:30 in the "afternoon" local time. They observe the same location at same time in different spectra to create synergic effects, but their responsiveness to unexpected events is still limited because of fixed orbital elements. In other words, the satellites in a "static" constellation can only follow the path defined by physics and cannot promptly access targets away from their paths. They don't have enough propellant to do many frequent maneuvers because reconfigurability was not considered in the design phase. Therefore, this thesis aims at increasing the responsiveness of Earth observation constellations by introducing reconfigurability.

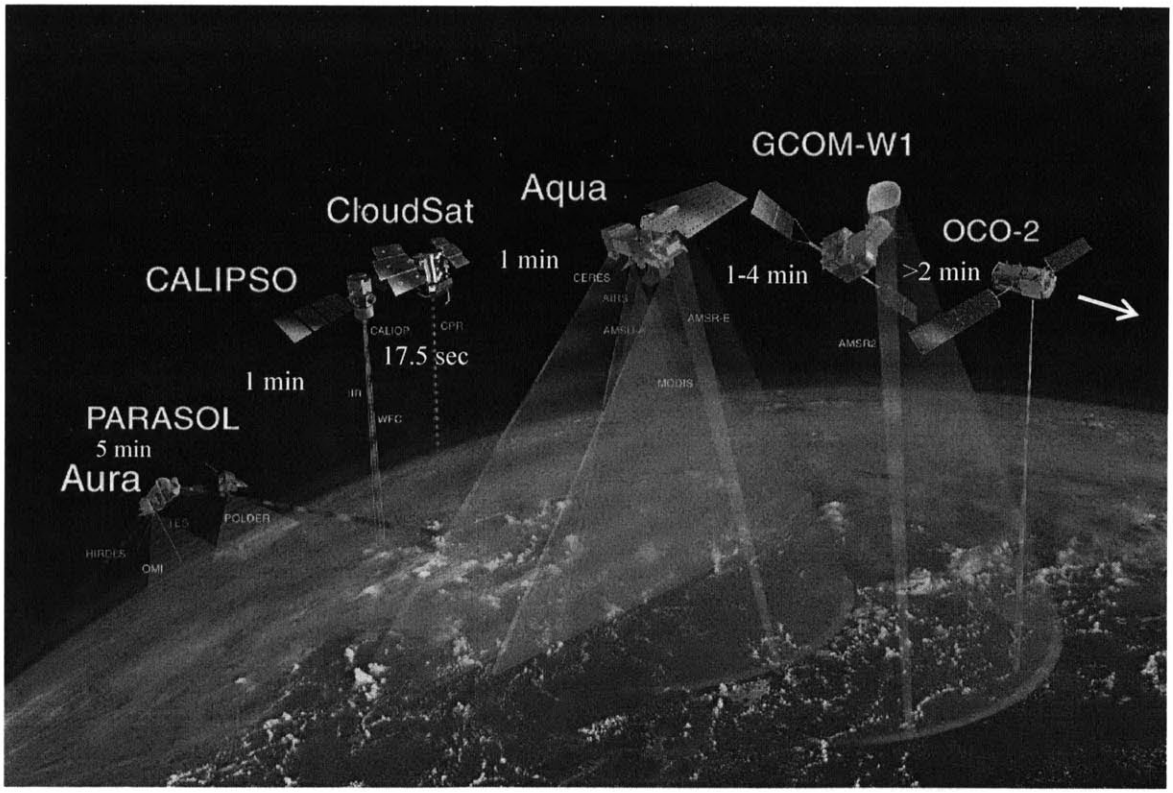

Figure 1-2: NASA A-Train [5]

1.2 Objective and Approach

The problem of ReCon design is well-suited for multidisciplinary system design optimization (MSDO) due to the following reasons.

1) Duality of the concept of operations: The ReCon is designed to reconfigure, or "toggle" between GOM and ROM, so its performance must be balanced between the two modes.

2) Multidisciplinary nature of satellite engineering: Spacecraft subsystems are highly coupled with each other as well as space environments in which the spacecraft is operating.

Therefore, the objective of this thesis can be formulated as:

> ***To*** *(1) minimize reconfigurable satellite constellation (ReCon) revisit time in both global observation and regional observation modes at given locations on the Earth, (2) minimize total system mass, and (3) minimize reconfiguration time* ***by*** *systematically changing orbit geometry design variables and satellite design variables* ***using*** *MSDO techniques* ***while*** *satisfying given resolution requirements for a given lifetime.*

The ReCon design problem consists of two fundamental questions:

- What should a ReCon geometry be? Specifically, what are the optimal baseline RGT altitude, altitude deviation, the number of orbit planes, and the number of satellites per plane?

- What is the satellite design that can achieve the mission objectives in a given ReCon configuration? What is the satellite mass allocation in relation to the optical payload, satellite bus, and propellant?

To answer these questions, this research aims to find optimal ReCon designs in terms of both constellation and satellite design. First, a high-fidelity model was constructed using MATLAB [6] and STK. Then a Design of Experiment (DoE) was performed to gain insight into the design space. This knowledge obtained from initial exploration was then used as a first guess in optimization algorithms to find optimal ReCon designs.

1.3 Thesis Outline

In order to address the ReCon design optimization problem, this thesis follows the steps illustrated in Figure 1-3.

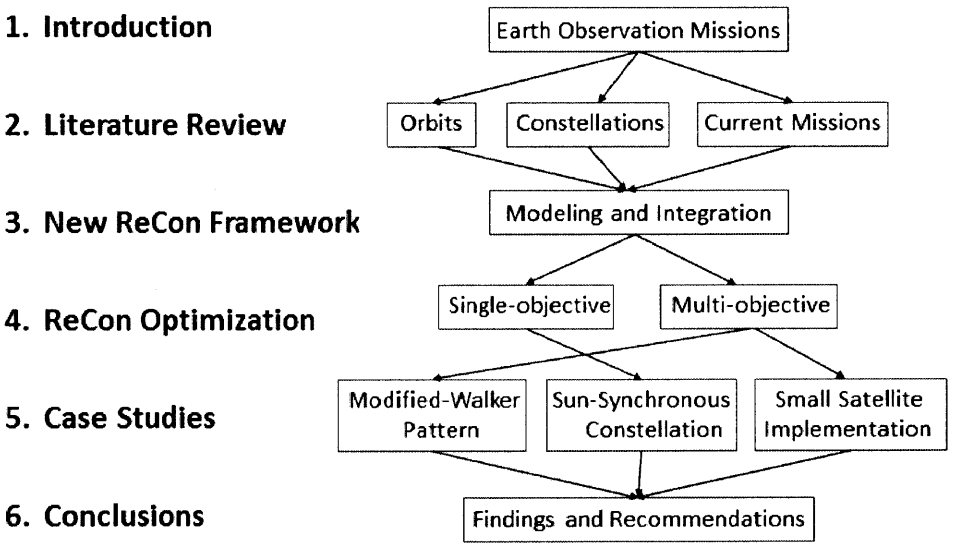

Figure 1-3: Thesis Roadmap

Chapter 2 provides the theoretical background of satellite orbits and constellations as well as classification of currently deployed satellite constellations. Through this, the relationship between the user requirements and the resulting constellation design can be identified. Also, previous research on reconfigurable constellations is revisited.

Chapter 3 describes the modeling of the ReCon problem, which is formulated as an MSDO problem. Both the satellite design and the constellation geometry are considered in

the design space, and they are evaluated with respect to coverage, revisit time, reconfiguration time, and launch mass.

Chapter 4 applies various optimization techniques to this ReCon framework in order to find optimal ReCon designs. Both single-objective and multi-objective cases are considered.

Chapter 5 focuses on case studies including the further tuning of optimal designs and implementation with small satellites.

Finally, Chapter 6 concludes with the key findings, and recommendations are made to further refine the ReCon model.

Chapter 2

Literature Review

In this chapter, fundamentals of orbital mechanics are first revisited and various designs of satellite constellations are presented along with their nomenclatures and characteristics. In light of this background, examples of currently deployed satellite constellations are discussed. Finally, research on reconfigurable satellite constellations is discussed.

2.1 Satellite Orbits

This section discusses the basic definitions of satellite orbits, especially in terms of classic orbital elements of Kepler orbits. A Kepler orbit can be any conic-section such as an ellipse, parabola, or hyperbola, among which an elliptical (or circular) orbit is of interest for Earth Observation missions. In this ReCon framework, the GOM orbit is assumed to be circular, which is a special case of an ellipse whose eccentricity is zero; the ROM orbit can be either circular or elliptical. In particular, the ROM orbit exploits the characteristics of repeating ground tracks, so their derivation is provided. Lastly, Sun-synchronous orbits are discussed, which are frequently utilized in Earth observation missions.

2.1.1 Kepler Orbits

A Kepler orbit is most widely used to describe the motion of an orbiting body. In this case, the orbiting object is a satellite that follows an elliptical orbit around the Earth. The motion of a satellite is confined in a two-dimensional orbit plane in three-dimensional space [7]. To describe this geometry, the Kepler orbit is specified by six orbit elements: semi-major axis (a), eccentricity (e), inclination (i), right ascension of the ascending node (Ω), argument of

perigee (ω), and true anomaly (v). These elements specify orbit size and shape (semi-major axis and eccentricity), the orientation of orbit plane (inclination, right ascension of the ascending node, and argument of perigee), and the position of the satellite within the orbit plane (true anomaly). Figure 2-1 illustrates a planar view of an elliptical orbit with relevant parameters [7, 8, 9]. Table 2.1 explains the definitions of these parameters and the relationship amongst them in more detail [10].

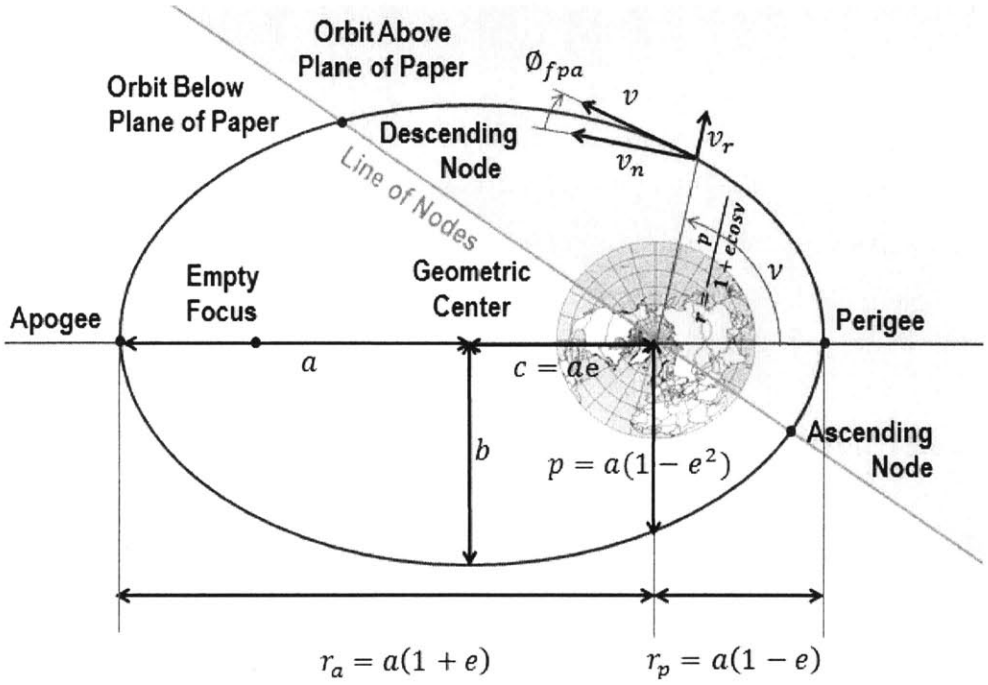

Figure 2-1: Elliptical Orbit Size and Shape Parameters [8, 9]

Table 2.1: Elliptical Orbit Geometry Parameters [10]

	Symbol	Definition	Relationship
Semi-major axis	A	One half of the major axis which is the longest diameter through the geometric center and the two foci	$a = (r_a + r_p)/2$
Semi-minor axis	B	One half of the minor axis which is the diameter through the geometric center perpendicular to the semi-major axis	$b = a\sqrt{1-e^2}$
Linear eccentricity	C	Distance between the geometric center and one of the two foci	$c = ae$
Eccentricity	E	A measure of orbital deviation from a perfect circle	$e = \sqrt{1-\frac{b^2}{a^2}}$

Semi-latus rectum	P	A half of latus rectum which is a chord perpendicular to one of the two foci	$p = a\sqrt{1-e^2}$
Focal parameter	L	Distance from one of the two foci to its nearest directrix (not shown in figure)	$l = p/e$
Perigee distance	r_p	Distance from perigee to the Earth's center of mass	$r_p = a(1-e)$
Apogee distance	r_a	Distance from apogee to the Earth's center of mass	$r_a = a(1+e)$
Perigee height	h_p	Distance from perigee to the Earth's surface	$h_p = r_p - R_E$
Apogee height	h_a	Distance from apogee to the Earth's surface	$h_a = r_a - R_E$

When a satellite is in an elliptical orbit, the Earth occupies one of its two foci and the other focus is left empty. If the geometric center of the ellipse is set to be the origin, then the (x, y) coordinates of any point on the orbit satisfy:

$$\frac{x^2}{a^2} + \frac{y^2}{b^2} = 1 \tag{2.1}$$

The equation above is derived from the mathematical definition of an ellipse - that the sum of distances from the two foci, located at (-c, 0) and (c, 0), is constant at any point on the elliptic path:

$$\sqrt{(x+c)^2 + y^2} + \sqrt{(x-c)^2 + y^2} = 2a \tag{2.2}$$

Instead of Cartesian coordinates with an origin at the center of the ellipse, we can also use polar coordinates with an origin at the Earth when the parametric equation of the elliptic path becomes

$$r = \frac{p}{1+e\cos\nu} \tag{2.3}$$

where the radial distance r is measured from the Earth center to the satellite and the true anomaly ν is measured from the perigee in radians. Also of importance in the maneuver analysis is the flight path angle, ϕ_{fpa}, defined as the angle between the velocity vector tangential to the elliptic path and the line perpendicular to the radius vector.

Because the true anomaly is usually difficult to calculate, the mean anomaly is often used as an equivalent counterpart in the corresponding circular orbit, as illustrated in Figure 2-2 [9, 11].

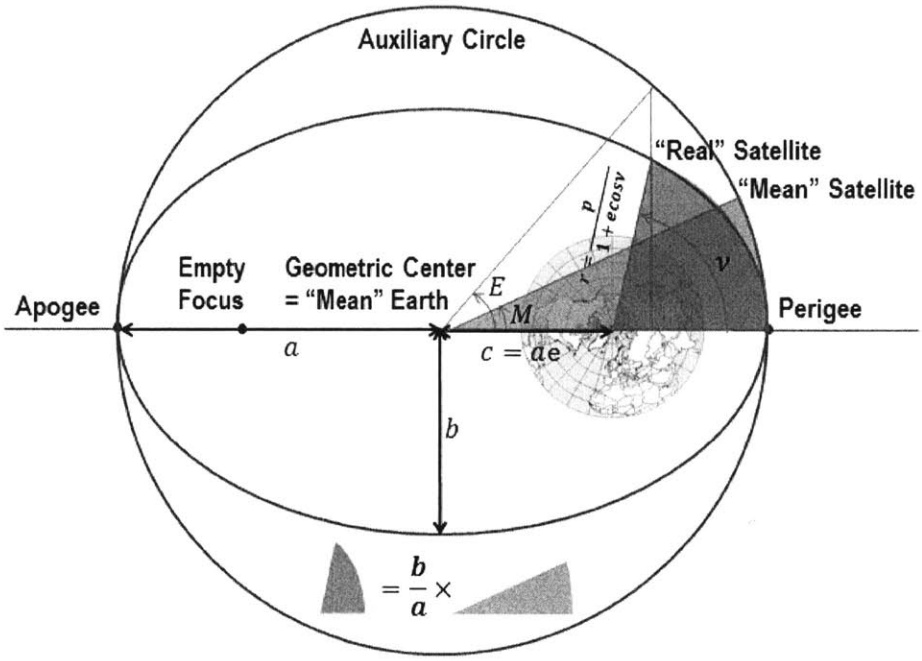

Figure 2-2: Anomalies in Kepler Orbit [9, 11]

The mean anomaly is easier to deal with because it increases linearly with time. Therefore, given the initial value and the rate of change, the mean anomaly at any time can be readily calculated as in Equation (2.4).

$$M = M_0 + n(t - t_0) \tag{2.4}$$

where M_0 is the mean anomaly at time t_0 (epoch) and n is the mean angular rate or the mean motion measured in rad/s given by Equation (2.5).

$$n = \sqrt{\mu_E / a^3} \tag{2.5}$$

In Equation (2.5), $\mu_E \equiv Gm_E$ is the Earth's gravitational constant and has a value of μ_E = 398,600km^3/s^2. The mean anomaly, M, is then converted to an intermediate variable, the eccentric anomaly, E, which is again converted to the true anomaly, ν.

First, the mean anomaly (M) is related to the eccentric anomaly (E) by Kepler's equation:

$$M = E - e\sin E \tag{2.6}$$

The eccentric anomaly (E) obtained from above is then related to the true anomaly (ν) by Gauss' equation in Equation (2.7).

$$tan\frac{\nu}{2} = \sqrt{\frac{1+e}{1-e}}tan\frac{E}{2} \tag{2.7}$$

Note that Kepler's equation in Equation (2.6) is transcendental and can only be solved numerically. Feinstein and McLaughlin (2006) discuss a variety of historical or modern numerical methods [11]. Also, it is noteworthy that the flight path angle can be related to the eccentric anomaly by Equation (2.8) [8]. The function atan2 refers to the inverse tangent which accounts for which quadrant a coordinate (x, y) lies in [13].

$$\begin{aligned} \emptyset_{fpa} = atan2\left(cos\emptyset_{fpa}, sin\emptyset_{fpa}\right) &= \cos^{-1}\left(\frac{\sqrt{\mu_E p}}{rv}\right) \\ sin\emptyset_{fpa} &= \frac{e\,sinE}{\sqrt{1-e^2cos^2E}} \\ cos\emptyset_{fpa} &= \frac{\sqrt{1-e^2}}{\sqrt{1-e^2cos^2E}} \end{aligned} \tag{2.8}$$

Hitherto, discussion was confined to two-dimensional space of the orbit plane, and only the size and shape of the elliptic orbit was specified by semi-major axis and eccentricity. In order to define the orbit orientation in three-dimensional space, rising ascension of the ascending node (RAAN), inclination, and argument of perigee, are required as illustrated in Figure 2-3 [14]. The intersection of the orbit plane and the equatorial plane is called the line of nodes (see Figure 2-1) and its relative angle from the vernal equinox or first point of Aries is defined as RAAN, Ω. The inclination, i, is the angle between the orbit plane and the equatorial plane, and the argument of perigee, ω, is the angular distance of the perigee from the line of nodes along the orbit plane.

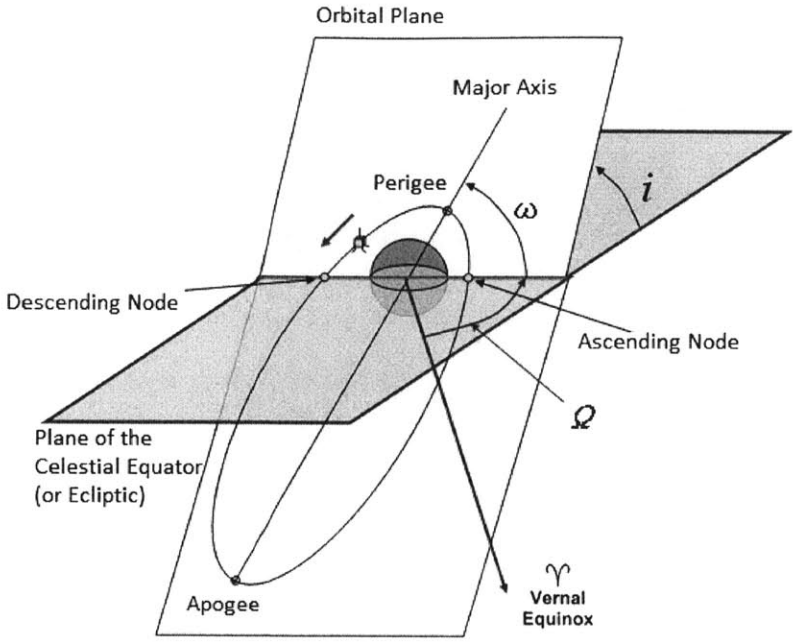

Figure 2-3: Elliptic Orbit Orientation Parameters [14]

2.1.2 Repeating Ground Track (RGT) Orbits

A satellite ground track is the path on the surface of the Earth directly below the satellite [15]; alternatively, it can be understood as the projection of the satellite's orbit onto the Earth's surface obtained by connecting all points of the orbit with the center of the Earth. As the satellite moves along the orbit, the corresponding point on the surface of the Earth also moves along its ground track.

Of special interest in the ReCon is a *repeating round track* (RGT), where the ground track of a satellite repeats exactly after one complete orbit around the Earth. This repeating pattern allows a satellite to frequently visit any targets along the ground track on a regular basis, as illustrated in Figure 1-1. RGT orbits can be achieved by matching the nodal period of a satellite (T_S) and the nodal period of Greenwich (T_G) to a ratio of two integers as in Equation (2.9) [16]. That is, a satellite in an RGT orbit with a RGT ratio equal to N_P/N_D orbit revolves around the Earth N_P times in N_D days.

$$T_{Total} = N_D T_S = N_P T_G \tag{2.9}$$

where T_{Total} is also called the repeat cycle [17]. The equation above can be rearranged to define an RGT period ratio, τ, where perturbation terms are included as seen in Equation (2.10):

$$\tau = \frac{N_P}{N_D} = \frac{T_G}{T_S} = \frac{2\pi/(\omega_E - \dot{\Omega})}{2\pi/(\dot{M}+\dot{\omega})} = \frac{2\pi/(\omega_E - \dot{\Omega})}{2\pi/(n+\Delta n+\dot{\omega})} = \frac{\dot{M}+\dot{\omega}}{\omega_E - \dot{\Omega}} \tag{2.10}$$

In the equation above, n denotes a satellite's mean motion; $\dot{M}$ denotes the perturbed mean motion (n+Δn) due to perturbations; ω_E is the rotation rate of the Earth; $\dot{\omega}$ is the drift rate of the argument of perigee due to perturbations; and $\dot{\Omega}$ is the orbit's nodal regression rate due to perturbations.

Synchronization with multiple sidereal days can reduce geo-potential resonances [18]. Resonance is unusual long-periodic motions caused by the exposure of a satellite to the Earth in a repeating orientation [19]. This happens when the frequencies of the satellite motion and the Earth's rotation are commensurate, or synchronized to a ratio of integers. The satellite "sees" a specific aspect of the Earth gravity field repeatedly, and the dynamical effects build up over time. The period of the variation in motion may be short (weeks) for shallow resonance or long for deep resonances (months or years) with a wide range of amplitudes from meters to hundreds of kilometers. Equation (2.11) defines the resonance parameter, ϵ_Θ, a measure of the resonance strength for RGTs; deep resonance corresponds to a strongly resonant case when $|\epsilon_\Theta|$ is very small whereas shallow resonance corresponds to a weaker case when $|\epsilon_\Theta|$ is larger. Small values of N_D and N_P correspond to higher gravitational coefficients and the amplitude of resonance is also proportional to the reciprocal of $|\epsilon_\Theta|$. Therefore, placing satellites in an RGT synchronized with multiple days can reduce the amount of propellant to correct deviations in orbit due to resonance. For example, the GPS constellation has $N_D = 1$ and $N_P = 2$, so its satellites rotates around the Earth twice a day with an orbit period of approximately 12 hours. The GLONASS constellation has $N_D = 8$ and $N_P = 17$; it can reduce the amount of propellant for orbit maintenances with a similar orbit period.

$$\epsilon_\Theta = N_D(\dot{M} + \dot{\omega}) - N_p(\omega_E - \dot{\Omega}) \tag{2.11}$$

$$P_{res} = 2\pi/|\epsilon_\Theta| \tag{2.12}$$

If perturbing forces up to second-order zonal effects are considered, the perturbed terms are expressed as follows [16].

$$\Delta n = \xi n\sqrt{1-e^2}(2-3\sin^2(i))$$
$$\dot{\omega} = \xi n(4-5\sin^2(i))$$
$$\dot{\Omega} = -2\xi n\cos(i)$$
$$\text{where } \xi = \frac{3R_E^2 J_2}{4a^2(1-e^2)^2} \tag{2.13}$$

In the equations above, J_2 is a zonal harmonic coefficient in an infinite series representing the Earth's gravity potential. J_2 corresponds to the equatorial bulging of the Earth and its value is approximately 0.00108263; i is the orbit inclination; and e is the orbit eccentricity. The RGT altitude h for a given synchronization ratio τ and inclination i can be calculated by solving the Equation (2.10). When J_2 perturbations are considered, a function of h in Equation (2.14) can be obtained and solved with the Newton-Raphson method.

$$f(h) = \frac{3J_2R_E^2\sqrt{\mu_E}}{2(R_E+h)^{7/2}}(4cos^2(i)-1) + \sqrt{\frac{\mu_E}{(R_E+h)^3}} - \frac{3J_2R_E^2\,\tau\sqrt{\mu_E}cos(i)}{2(R_E+h)^{7/2}} - \omega_E\tau \tag{2.14}$$

The first derivative of Equation (2.14) becomes:

$$f'(h) = \frac{3\sqrt{\mu_E}}{4}\frac{7J_2R_E^2(1+\tau cos(i))-28J_2R_E^2cos^2(i)-2(R_E+h)^2}{(R_E+h)^{9/2}} \tag{2.15}$$

An initial guess can be made by replacing J_2 with zero in order to neglect J_2 perturbations and make a two-body assumption. Thus, the initial guess, h_0, is obtained by Equation (2.16), which is recursively plugged into Equation (2.17) until the solution converges within desired tolerances [20].

$$h_0 = \sqrt[3]{\frac{\mu_E}{\tau^2\omega_E^2}} - R_E \tag{2.16}$$

$$h_{n+1} = h_n - \frac{f(h_n)}{f'(h_n)} \tag{2.17}$$

For example, the RGT altitude where a satellite orbits the Earth 15 times a day (τ = 15/1) is plotted as a function of inclination. It can be seen that consideration of J_2 perturbations significantly alters the RGT altitude compared to when J_2 perturbations are ignored. Also, a general tendency is that the RGT altitude gets higher as inclination increases.

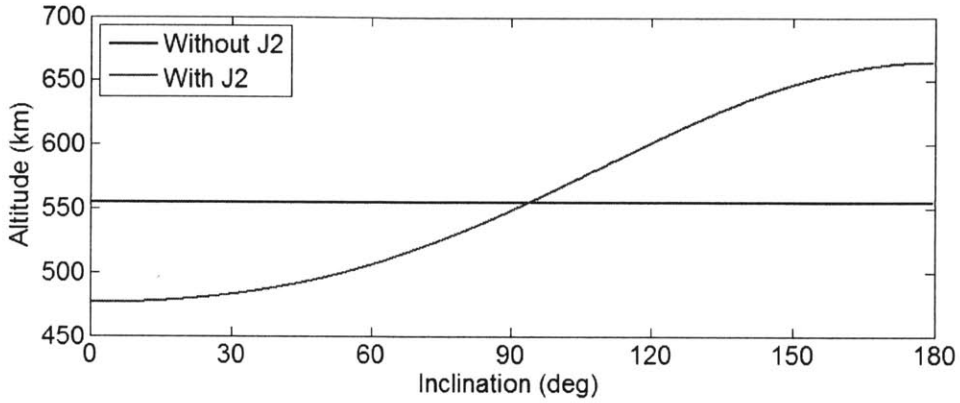

Figure 2-4: RGT Altitude with RGT Ratio τ = 15/1

2.1.3 Sun-synchronous Orbits

A Sun-synchronous orbit is an orbit in which the perturbation due to the oblateness of the Earth causes the orbit to regress at a rate equal to the average rate of the Earth's rotation around the Sun [21]. In other words, the orientation of the orbit plane will remain nearly fixed with respect to the Sun throughout a year, and the satellite will pass the equator (and any non-zero latitude within inclination) at the same local mean solar time, as shown in Figure 2-5 [21]. For example, a satellite in a "twilight" orbit may cross the equator 15 times a day at 6:00am/pm local time; however, the satellite period and the Earth day need not be always synchronized. Figure 2-6 illustrates the Sun-synchronous orbits synchronized with different local times.

The equatorial bulge of the Earth tries to pull the satellite toward the equatorial plane, but the satellite orbiting the Earth has gyroscopic stiffness. Therefore, the orbit inclination does not change, but the nodes regress instead. Figure 2-7 shows this phenomenon where the orbit plane migrates westward ($\dot{\Omega} < 0$) for a prograde orbit whose inclination is less than 90 °.

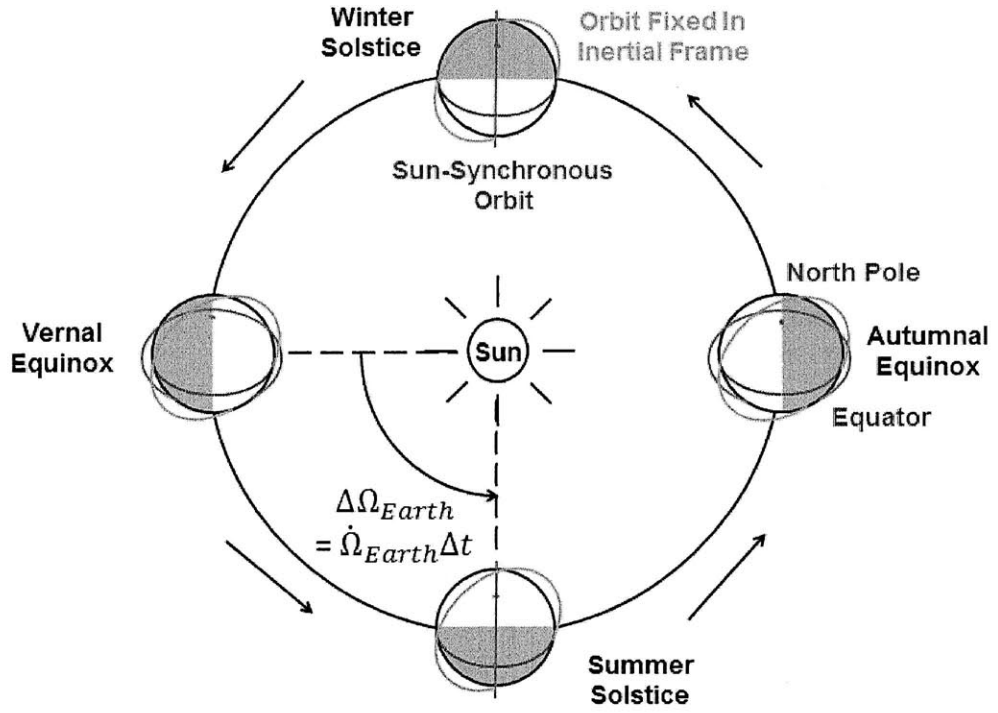

Figure 2-5. Orbit Fixed in Inertial Frame (Green) and Sun-synchronous Orbit (Blue) [21]

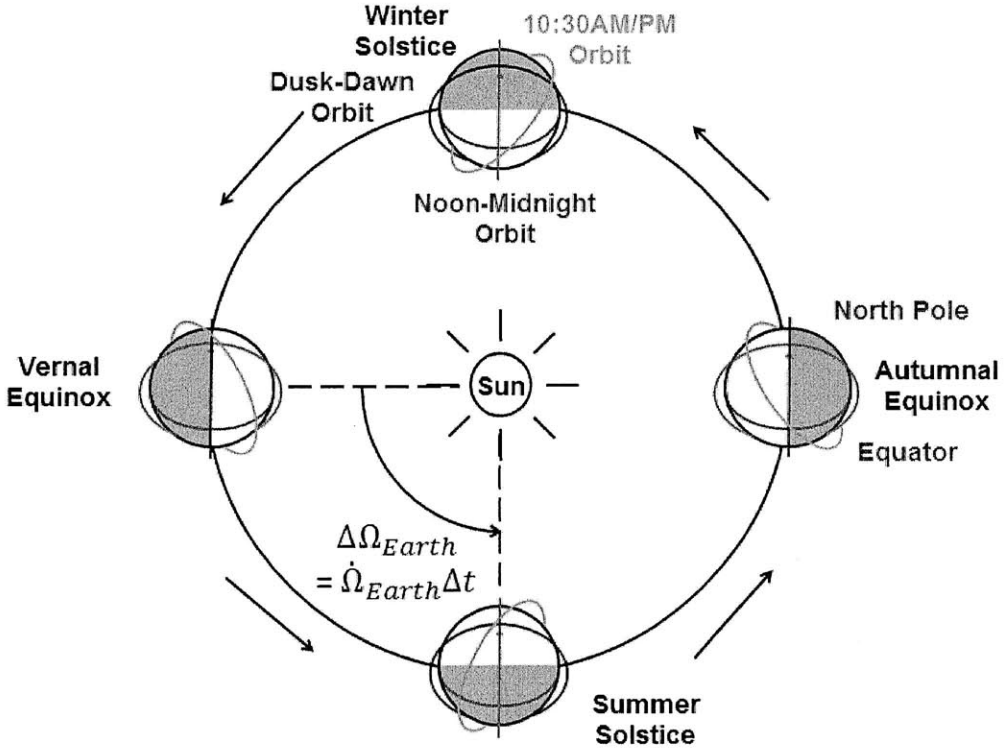

Figure 2-6: Types of Sun-synchronous Orbits [22, 23]

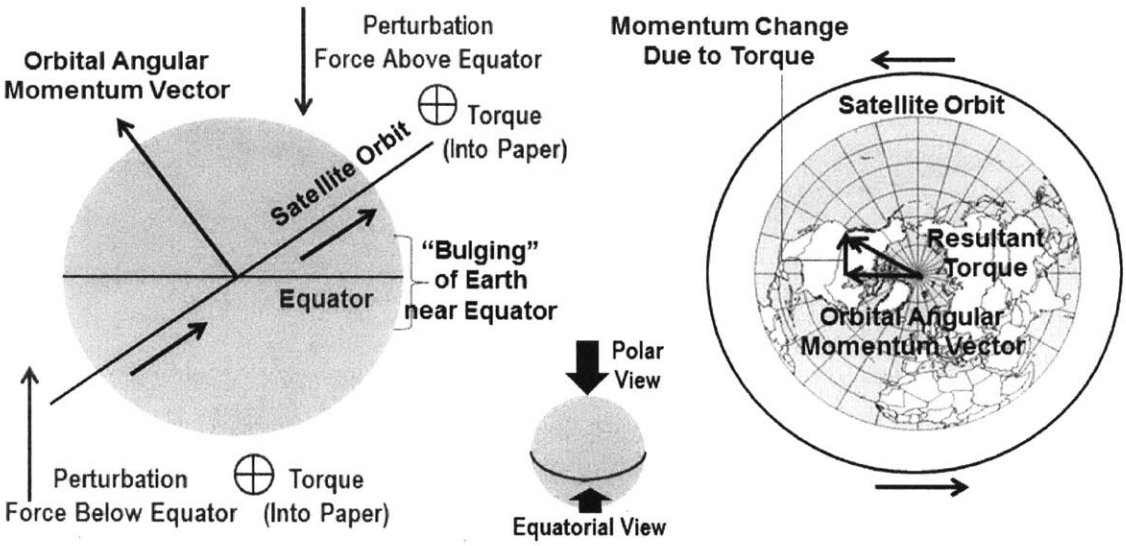

Figure 2-7: Orbit Plane Torque Diagram [13]

Rearranging Equation (2.11) reveals that the nodal regression rate is a function of semi-major axis, eccentricity, and inclination as shown in Equation (2.18).

$$\dot{\Omega} = -\frac{3R_E^2 J_2 \sqrt{\mu_E}}{2a^{7/2}(1-e^2)^2}\cos(i) \tag{2.18}$$

Figure 2-8 illustrates this relationship for circular orbits (e=0); the red line corresponds to the inclination of 90°such that $\dot{\Omega}$=0. The nodal regression rate is positive if the inclination is greater than 90° (retrograde), which corresponds to the right side of the red line. For an orbit to be sun-synchronous, this rate must equal the Earth's rotation rate around the Sun, or $\dot{\Omega}$ equals 360° ÷ 365.2422day = 0.9856°/day; therefore, all sun-synchronous orbits are retrograde.

The Sun-synchronous orbit has a number of interesting characteristics. As mentioned earlier, its same local mean solar time guarantees an approximately constant angle of solar illumination which is especially useful for Earth observation missions utilizing visible or infrared wavelengths. Also, the satellite in a dawn-dusk (twilight) orbit has very short eclipses, which may reduce power subsystem requirements. However, launching into a retrograde orbit disables launch vehicles from taking advantage of the Earth's spin, so an increased fuel requirement results in an additional launching cost of 30% [8].

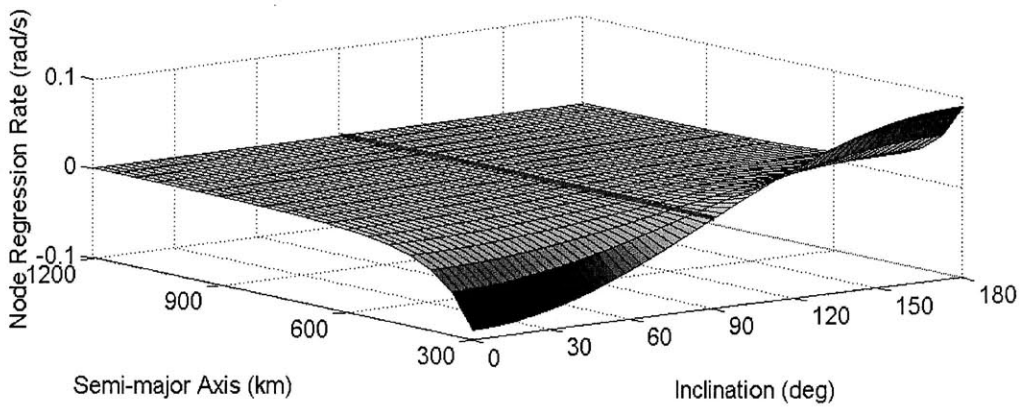

Figure 2-8: Regression of the Nodes

2.2 Satellite Constellations

From a designer's perspective, satellite constellations can be largely subdivided into homogeneous patterns and heterogeneous patterns. Homogeneous patterns have a finite number of possible designs, so their design space can be fully exploited [8]. On the other hand, heterogeneous patterns have much higher variability, which prevents a full investigation of their design space. Homogeneous patterns include Walker Delta Pattern constellations, near-polar (Walker Star) constellations, and elliptical orbit constellations [24]; heterogeneous patterns are combinations or variations of homogeneous patterns. Both homogeneous and heterogeneous constellations can be described with a single notation called Flower Constellation. This categorization of homogeneous patterns and heterogeneous patterns is valid from a mathematical viewpoint, but constellations which are homogeneous in principle are implemented heterogeneously in practice due to mission requirements. Therefore, instead of this classification according to homogeneity, this section discusses five conventional types of constellations: geosynchronous constellations, polar (or near-polar) constellations, elliptical constellations, non-uniform elliptical constellations, and Flower constellations. This section then concludes with ongoing research on reconfigurable constellations.

2.2.1 Geosynchronous Constellations

Geosynchronous constellations consist of satellites in a geosynchronous orbit, or Geostationary Earth Orbit (GEO), and require the fewest number of satellites for a near-global coverage. Three satellites can cover the entire equatorial and mid-latitude regions. Furthermore, each satellite appears stationary relative to the surface of the Earth and guarantees a continuous coverage and fixed-orientation of antennas [25], both of which provide great advantages for communications. However, reaching geosynchronous orbits is fuel-expensive and there are limited longitudinal slots where geosynchronous satellites can be located. Also, high latitude regions cannot be covered well and the distance is too far from the Earth to obtain high-quality imagery of the Earth's surface. Examples include Tracking and Data Relay Satellite System (TDRSS) for space communications and InmarSat for commercial telephony services [26, 27]. Although a minimum of three satellites are required for a near-global coverage, the number or/and phasing of GEO satellites are oftentimes tailored according to the mission requirements such as service demands, as shown in the InmarSat constellation in Figure 2-9 [9, 26, 27].

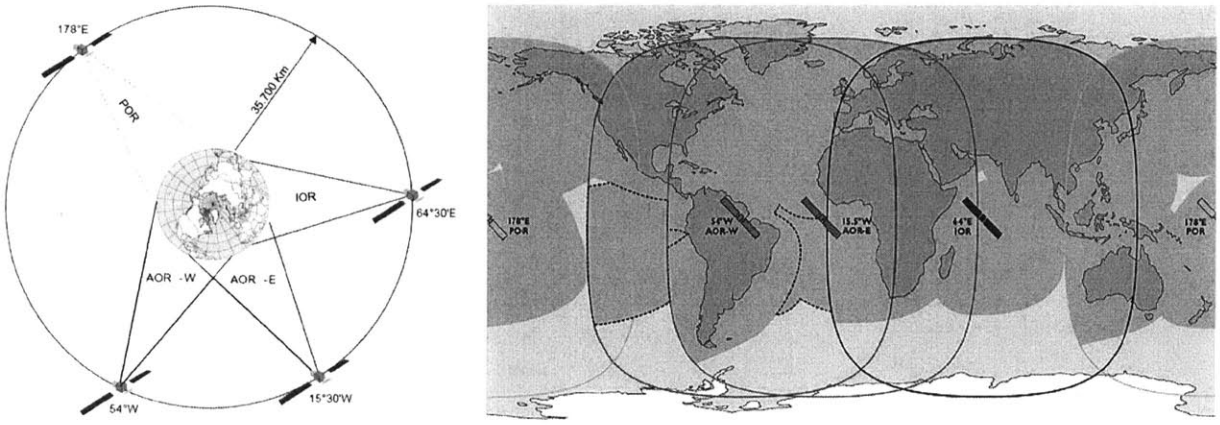

(a) Polar View (b) Ground Coverage

Figure 2-9: InmarSat Constellation [9, 26, 27]

2.2.2 Polar and Near-polar Constellations

Polar constellation consist of orbits with an inclination of exactly 90° and near-polar constellations have an inclination which is slightly greater or smaller than 90°in accordance with specific mission requirements. "Streets of coverage (SOC)" methods are often used to fill the gaps between adjacent orbit planes and to provide a global continuous coverage, as illustrated in Figure 2-10. On a global scale, half of the satellites are moving northward and another half are moving southward at any given time. These satellites moving opposite to each other form a boundary called a seam [28].

Because a sustainable inter-satellite link (ISL) cannot be established across the seam, data should be relayed through Polar Regions as illustrated in Figure 2-11 [28, 29]. The near-polar constellation is also called the Walker Star pattern because it looks like a star when seen from one of the Poles due to plane intersections.

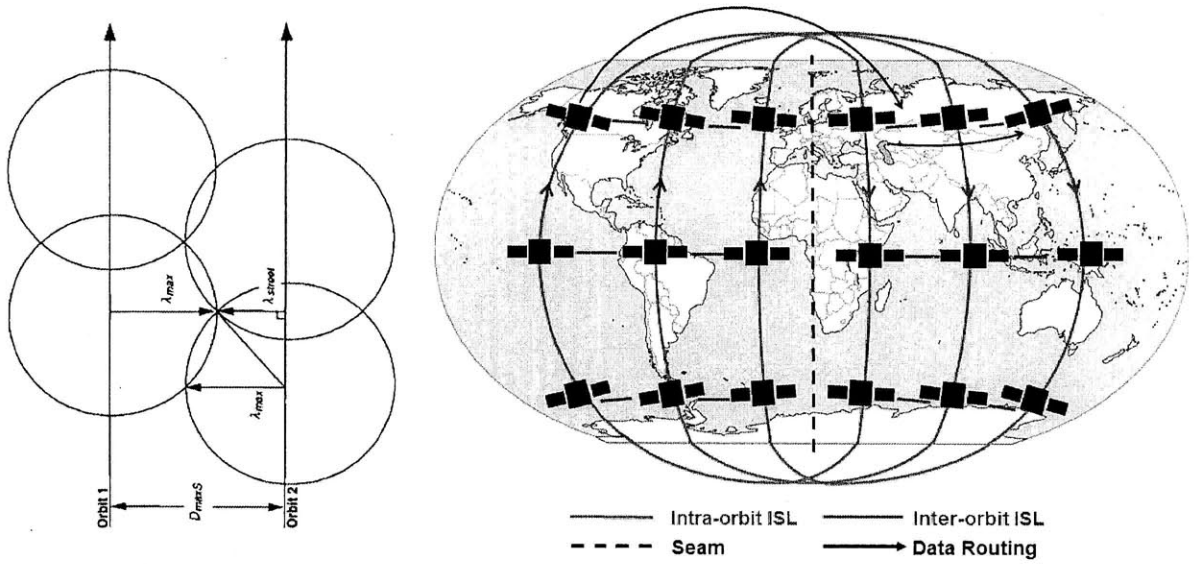

(a) Streets of Coverage (b) Global View

Figure 2-10: Polar Constellation [8, 28, 29]

Adams and Lang (2004) compared the Walker constellations and SOC in terms of the overlap of coverage, coverage requirement, and the launch vehicle capability [30]. Walker constellations are more efficient for single-fold (without overlaps) global coverage with T<20 (T is the total number of satellites), whereas SOC constellations are more efficient for lower altitudes with T>20.

Polar or near-polar constellations have two major drawbacks [8]. First, satellites on either side of the seam must operate differently to account for asymmetry of coverage and relative motion in the seam compared to those of other planes. Second, the greatest coverage is achieved near Polar Regions where the demand for communication services is the smallest. This coverage mismatch with the service demand is mitigated by reducing the inclination of orbits, which introduces Walker Delta constellations, covered in the next section.

2.2.3 Walker Delta Constellations

A class of popular circular orbit constellations is the Walker Delta constellation (termed Walker constellation hereafter), which provides the most symmetry by having similar orbits amongst satellites [24]. This symmetry not only enables a thorough search of a finite design space, but also provides advantages in orbital constellation management because any satellite in a constellation undergoes similar effects from perturbations. John Walker did an extensive study of this type of constellations and proposed a notation of $i: T / P / F$, where a total of T satellites are evenly distributed in P orbit planes with an inclination i (°) and a phase difference of $360/T \times F$ (°) between adjacent planes [31]. Figure 2-11 shows a Globalstar constellation which uses a 48/8/1 Walker pattern.

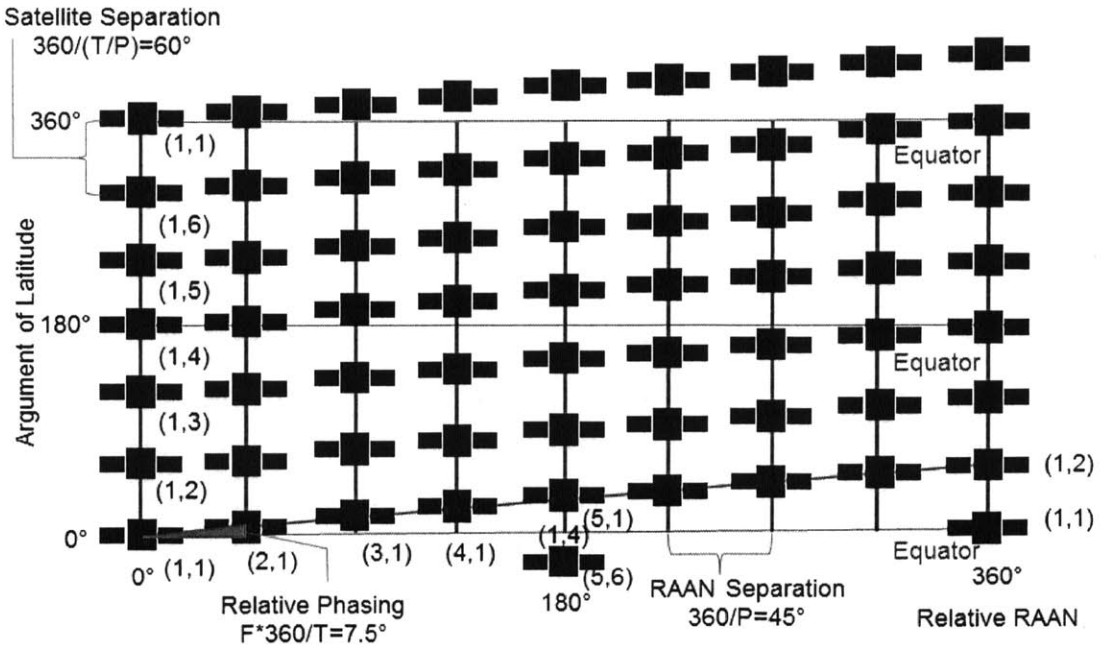

Figure 2-11: GlobalStar Constellation with a 48/8/1 Walker Pattern [31]

The phasing parameter F can take integers from 0 to P-1. Lang [32] found an empirical relationship that the optimal coverage occurs if the phasing parameter F satisfies the Equation (2.19); if F is negative, P is added to F repeatedly until F becomes positive.

$$F = P - 1 - T/P \tag{2.19}$$

2.2.4 Elliptical Orbit Constellations

Introducing a non-zero eccentricity in constellation designs increases the design complexity and manufacturing cost of satellites because they have to operate in a wide range of altitudes with varying space environments. Nonetheless, elliptical orbits can reduce the number of satellites in a constellation and increase coverage over specific areas of interest which can compensate for increased costs in certain cases [8].

Rearranging Equation (2.11) gives the rotation rate of argument of perigee in terms of semi-major axis, eccentricity, and inclination:

$$\dot{\omega} = \frac{3R_E^2 J_2 \sqrt{\mu_E}}{4a^{7/2}(1-e^2)^2}\left(4 - 5\sin^2(i)\right) \tag{2.20}$$

Figure 2-12 plots the perigee rotation rate when eccentricity is zero; for elliptical orbits, the amplitude is multiplied by a constant, but the overall tendency is the same. For a highly elliptical orbit (HEO), coverage conditions differ drastically between the apogee and the perigee, so it is useful to fix the argument of perigee. In order to make the perigee rotation rate zero, the orbit should be inclined at a "critical" angle, either 63.4°or 116.6°, represented by red lines in Figure 2-12.

Many prograde HEOs have an inclination of 63.4°; Molniya orbits have a period of one half of a sidereal day and Tundra orbits have a period of one sidereal day. A constellations consisting of three satellites with either orbit provides a continuous coverage over certain regions by means of apogee dwelling; from Kepler's second law, the satellite moves at a slower speed near the apogee and remains visible over the servicing area for most of the time of its orbit period. Figure 2-13 shows examples of a Molniya constellation and a Tundra constellation which provide communications services over Russia and Japan, respectively [33, 34].

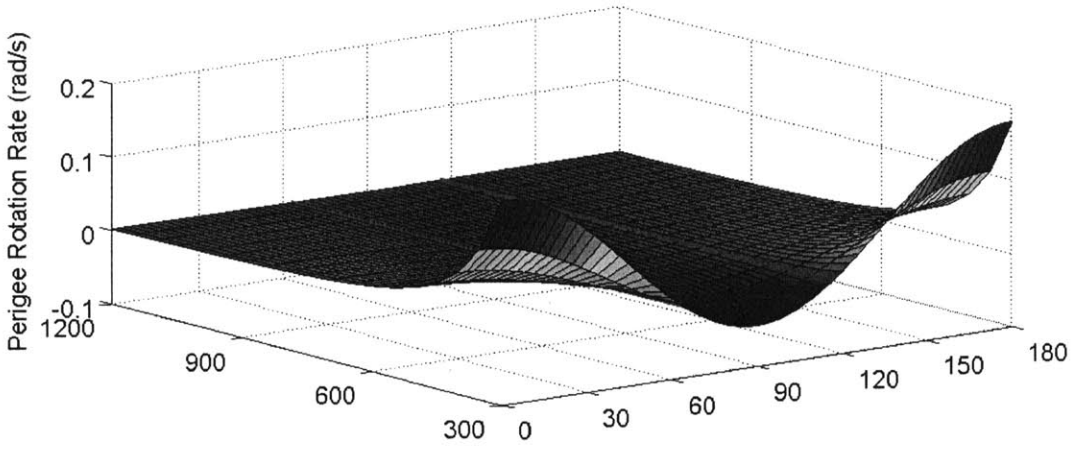

Figure 2-12: Argument of Perigee Regression

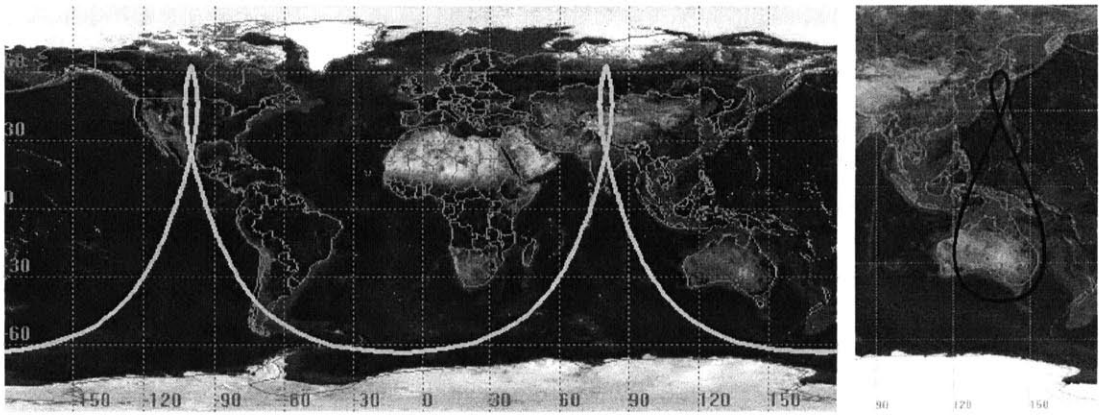

(a) Molinya (b) Tundra

Figure 2-13: Highly Elliptical Orbit [33, 34]

Although the Walker constellation assumes zero eccentricity, its notation $i: T / P / F$ is still useful to categorize many elliptical orbit constellations. The Walker constellation for a regional coverage can be represented by T/P/F = N/N/(N-Q), where the number of distinct regions serviced equals Q [32]. Consequently, a Molniya constellation with three satellites is a 3/3/2 Walker constellation and a Tundra constellation with three satellites is a 3/3/1 Walker constellation.

2.2.5 Non-uniform Elliptical Constellations

Non-Walker constellations can provide improved regional access over Walker constellations specified by longitude, latitude, and time. These constellations have non-uniform inclination, altitude, or eccentricity.

The Ellipso constellation for personal communications consists of a Molniya orbit with 63.4° inclination, a Molniya orbit with 116.6° inclination, and an equatorial circular orbit [35]. This combination provides high coverage over both high-latitude and low-latitude regions, as illustrated in Figure 2-14.

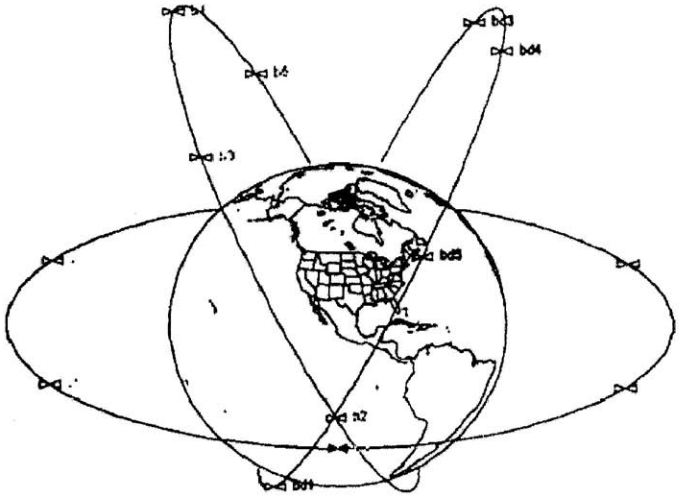

Figure 2-14: Baseline Ellipso Three-Plane Constellation [35]

The Communications Orbiting Broadband Repeating Array (COBRA) consists of a critically inclined (inclination of either 63.4° or 116.6°) 8-hour elliptical orbit. The "teardrop" variant of the COBRA array employs both the left-inclined orbit (inclination of 116.6°) and the right-inclined orbit (inclination of 63.4°) so that satellites in two orbit planes can provide a continuous coverage by performing seamless handovers at two ends of the teardrop patterns, denoted as high latitude and low latitude handover points (HLHOs and LLHOs) in Figure 2-15. The satellites are active when they are in the Northern Hemisphere near the apogee and inactive otherwise [36].

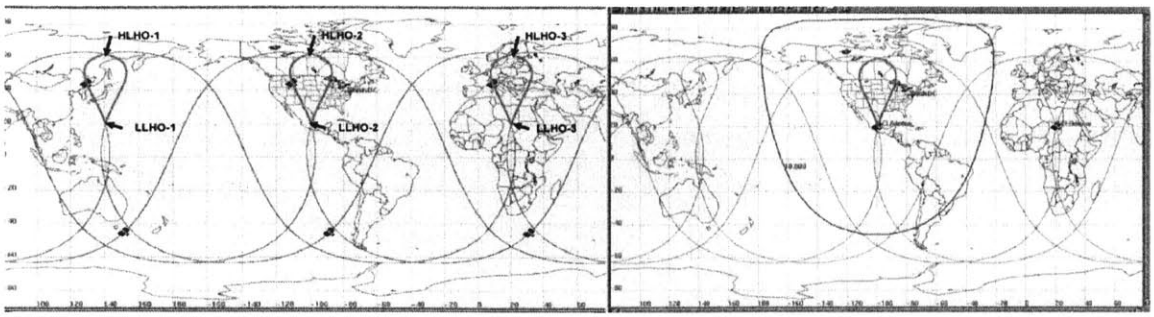

(a) Six-satellite Baseline Array and Hand-over Points

(b) Snapshot Coverage with Alternating Handovers between HLHO and LLHO

Figure 2-15: COBRA Teardrop Constellation [36]

Wertz analyzed a number of responsive orbits or constellations into which Earth observation satellites can be promptly launched upon identification of targets [37]. Figure 2-16 shows sample responsive orbits. A LEO Fast Access Orbit provides the first access to a designated target in one orbit period or two. A LEO Repeat Coverage Orbit provides four or five consecutive revisits a day by adjusting the orbit inclination and the satellite swath width such that $i \cong L + \theta_{max}$, where L is the latitude of a target and θ_{max} is the maximal Earth-centered half-cone angle of the satellite sensor.

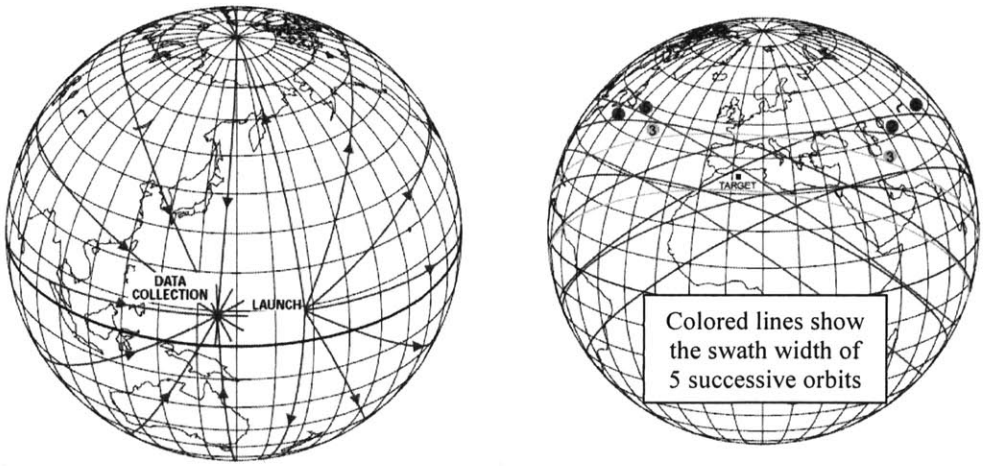

(a) Fast Access Orbit

(b) Repeat Coverage Orbit

Figure 2-16: Responsive Orbits [37]

2.2.6 Flower Constellations

Flower Constellations provides a generalized framework capable of describing non-uniform constellations as well as uniform constellations such as Walker patterns and Polar constellations. All satellites are assumed to have identical semi-major axis, eccentricity, inclination, and argument of perigee. The Flower Constellations framework uses six additional parameters to complete the constellation description in addition to semi-major axis, eccentricity, and inclination [38]:

- N_d – Number of days to repeat
- N_p – Number of petals
- F_d – Phase denominator (Number of inertial orbit planes)
- F_n – Phase numerator Spacing around central body
- F_h – Phase Step
- N_s – Number of satellites

N_d and N_p define the orbit period and the semi-major axis, as discussed earlier. The shape and orientation can be further defined from eccentricity, inclination, and argument of perigee. F_n, F_d, and F_h are additional phasing parameters which define satellite distribution; in the Flower Constellations methodology, all satellites follow the same three-dimensional trajectory in the rotating reference frame, which dictates a phasing rule in terms of ascending node and mean anomaly [38].

$$\Omega_k = 2\pi \frac{F_n}{F_d}(1-k)$$

$$M_i = 2\pi \frac{F_n N_p + F_d F_h}{F_d N_d}(k-1)$$

$$\text{where } k = 1, 2, \ldots, N_s \text{ and } F_h = 0, 1, \ldots, N_d - 1 \qquad (2.21)$$

When a Flower Constellation distributes its satellites evenly in ascending node and mean anomaly, it is called a Lattice Flower Constellation (LFC). It can be shown that LFCs and Walker constellations are equivalent, and the relationship between the two notations is shown in Table 2.2 [39]

Table 2.2: Comparison of LFCs and Walker Constellations [39]

	LFC	Walker
Number of planes	F_d (=P)	P (= F_d)
Number of satellites per plane	N_s/F_d (=S)	S (= N_s/F_d)
Phasing parameter	N_c (=$-F \bmod F_d$)	F (= $-N_c \bmod F_d$)

The variable N_c in a LFC is defined by the following set of equations with integer variables including intermediate variables E_n and E_d.

$$N_c = E_n \frac{N_p N_c + F_d F_h}{G} \bmod F_d$$
$$G = \gcd(N_d, N_p F_n + F_d F_h)$$
$$E_n F_n + E_d F_d = 1 \tag{2.22}$$

For example, a T/P/F = 48/8/1 Walker constellation whose orbits have an RGT with τ=1/15 is identical to an LFC with $(N_d, N_p, F_d, F_n, F_h, N_s)$ = (1,15,8,1,0,48). It is notable that the representations of LFCs corresponding to a specific Walker constellation may not be unique. Figure 2-17 illustrates that the same constellation can be represented by either (N_d, N_p) = (5, 8) or (N_d, N_p) = (1, 17), which resembles aliasing effects.

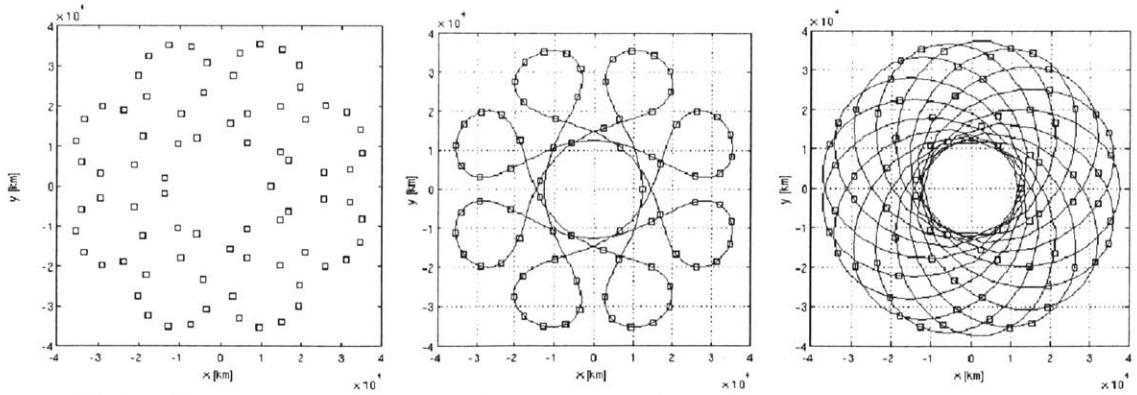

(a) Satellite Locations (b) Representation 1 : (N_d, N_p) = (5, 8) (c) Representation 2 :(N_d, N_p) = (1, 17)

Figure 2-17: Lattice Flower Constellation [38]

2.3 Currently Deployed Satellite Constellations

Based on previous discussions of satellite orbits and constellations, currently deployed satellite constellations can be categorized in terms of mission types: communications, navigation, and Earth observation. Also, design rationales and characteristics can be compared amongst different types of missions by relating them to mission requirements.

2.3.1 Satellite Constellations for Communications

Satellite constellations for communications were deployed earlier than constellations for other purposes. Also, communications constellations still include more satellites than those for other purposes. Table 2.3 lists the representative satellite constellations for telephony or messaging services providing a global coverage [40, 41, 42, 43, 44]. The constellation design varies widely from LEO to GEO, but only the Iridium satellite constellation can cover the Polar Regions well.

Table 2.3: Satellite Constellations for Communications [40, 41, 42, 43, 44]

System	Globalstar	Orbcomm	Iridium	Inmarsat	TDRSS
Altitude	1,414km	720km (Gen-1) 661km (QL) 750km (Gen-2)	780km	35,786km	35,786km
Inclination	52°	45° 48.45° 52°	86.4°	0°	0°
Number of Satellites	48	35 6 18 (planned)	66	5	9
Status	Operational	Gen-1 and QL active, Gen-2 to be launched between 2012 and 2014	Operational	Operational	Operational

2.3.2 Satellite Constellations for Navigation

Satellite constellations for navigation and geodesy are actively being deployed by several nations: Global Positioning System (GPS), Global Navigation Satellite System (GLONASS),

BeiDou (Compass) Navigation Satellite System, and Galileo to name a few that provides a global coverage. Table 2.4 compares the orbit architectures of these constellations [43, 44, 45, 46, 47]. Most of them utilize medium Earth orbits (MEOs), arising from a trade-off mainly between the signal power requirement and coverage. Also, the orbit periods are synchronized with Earth's sidereal days with a ratio of two integers.

Table 2.4: Satellite Constellations for Navigation [45, 46, 47, 48, 49]

System	GPS (United Sates)	GLONASS (Russia)	COMPASS (China)	Galileo (European Union)
Altitude	20,180km	19,130km	21,150km	23,220km
Period	11h 58m	11h 16m	12h 38m	14h 5m
Revolution per sidereal day	2	17/8	1(GEO), 36/19(MEO)	17/10
Inclination	Near 55°	64.8°	55.5°	56°
Constellation Geometry	24+3 MEO (Total 30)	24 MEO (24/3/2 Walker)	5 GEO + 3 IGSO + 27 MEO	27 MEO (27/3/1 Walker)
Status	Operational	Operational	10 satellites operational (+ 25 planned)	2 test bed satellites in orbit (+ 22 in preparation)

2.3.3 Satellite Constellations for Earth Observation

Table 2.5 lists the representative satellite constellations for Earth observation. Because of Earth observation requirements in terms of ground resolution and illumination conditions, they are all in low-Earth sun-synchronous orbits. The number of satellites in each constellation is also fewer than in the aforementioned constellations.

Table 2.5: Satellite Constellations for Earth Observation [50, 51, 52, 53]

System	A-Train	Disaster Monitoring Constellation (DMC)	RapidEye	KeyHole-11
Altitude	690km	675km	630km	300km × 1000km (approximation)
Inclination	98.1°*	98.2°*	97.8°*	97.9°*
Number of satellites	4	4 (1st Gen) 4 (2nd Gen)	5	5
Status	Operational	Operational	Operational	Operational

*: Sun-synchronous orbit

2.4 Reconfigurable Satellite Constellations

Conventional satellite constellation designs discussed so far have focused on optimizing global, zonal, or regional coverage [29] under an assumption that the satellites are deployed simultaneously and the constellation remains static afterwards. Here the term "static" refers to the condition that altitude and relative slots remain constant over time [29]. However, it can be helpful to expand a satellite constellation gradually in order to reduce risks such as launch failures or uncertainties in market demands. Also, an operationally reconfigurable constellation aims to perform reconfigurations throughout its lifetime to switch between modes - one optimized for global observations and the other optimized for regional observations.

2.4.1 Staged Deployment of Constellations

Commercial LEO constellations for personal communications such as Iridium and Globalstar were a success from a technical viewpoint, but were a failure from a business perspective due to market changes which had occurred between the conceptual design phase and commissioning [54]. Therefore, a "staged deployment" strategy has been proposed as an alternative approach to reduce uncertainties and accompanying risks [54, 55].

Figure 2-18 further elaborates the staged deployment concept. Only part of the constellation is deployed at first and the altitude is relatively high to provide global coverage with a limited number of satellites. The satellites can be added to the constellation later in accordance with the market demand, and the altitude can be adjusted to be lower in order to increase the service capacity by reducing signal losses. Scialom et al. (2004) devised a reconfiguration map that provides optimized paths along which a communications constellation can evolve, as shown in Figure 2-19.

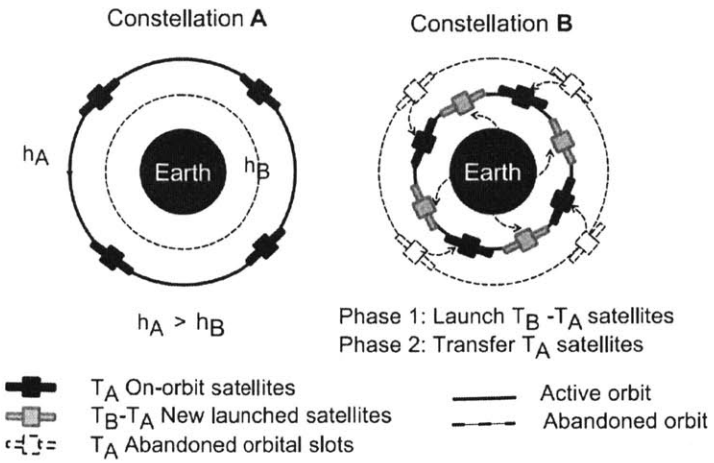

Figure 2-18: Staged Deployment Concept with Two-phase Reconfigurations [54]

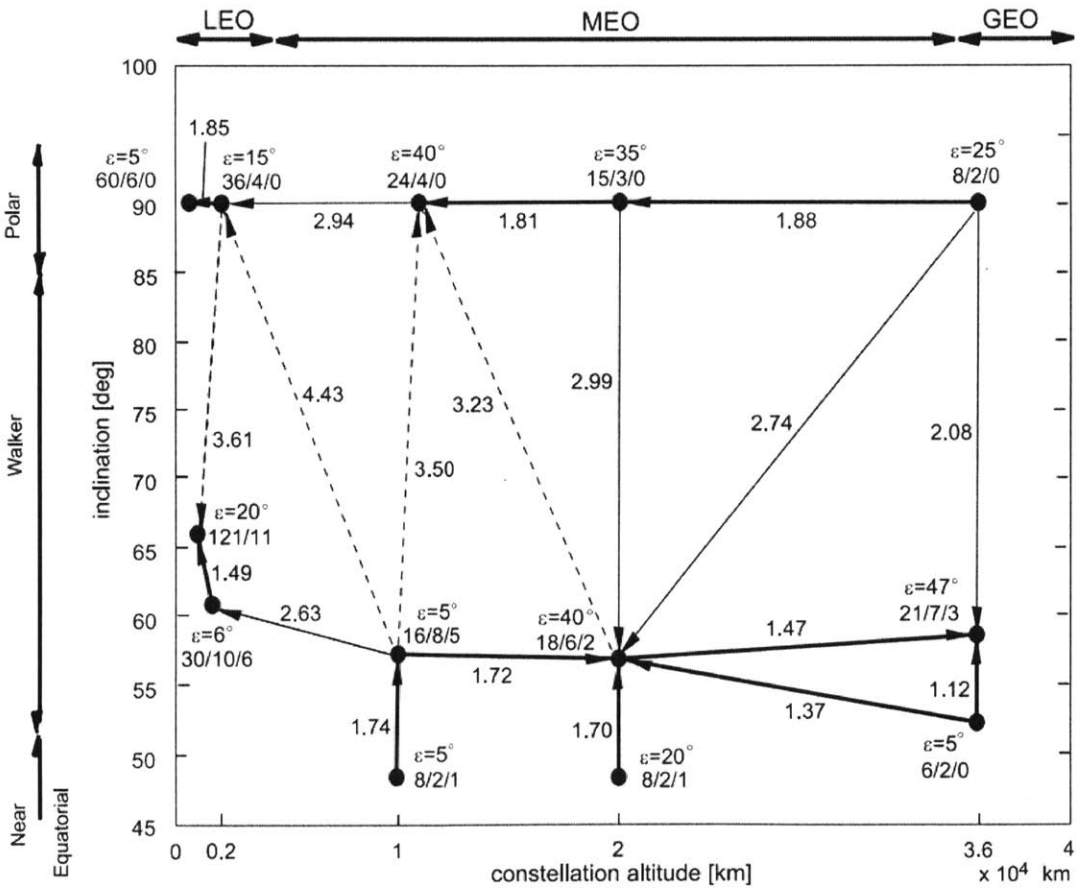

Figure 2-19: Reconfiguration Map of Delta-V per Satellite [54]

2.4.2 Operationally Responsive Constellations

A satellite has to make delta-V burns with its propulsion system in order to fight the forces that perturb the satellite from its designed path. Although this station-keeping can also be viewed as reconfiguration, some satellites perform more active maneuvers frequently throughout design life. For example, surveillance satellites carry extra fuel to change their altitude and orbit planes to access ground targets. The Key Hole (KH) satellite constellation is a good example of operationally responsive constellations, which consists of four satellites. As can be seen in Figure 2-20(a) [51], the KH-11 satellites are all in Sun-synchronous orbits to provide consistent illumination conditions for optical imaging. Of interest in their satellite bus design is the propulsion subsystem to maneuver and change orbits, as illustrated in Figure 2-20(b) [53].

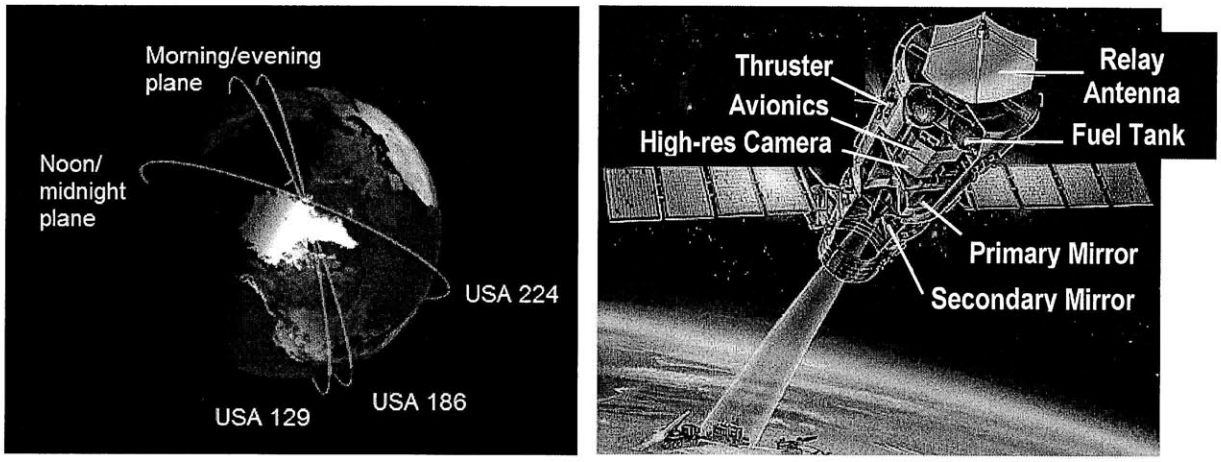

(a) KH-11Constellation (August 2011) (b) KH-11 Payload and Bus Design

Figure 2-20: Key Hole-11 Reconnaissance Satellites [53, 56]

On the academia side, Bogosian (2008) studied optimization of reconfigurable satellite constellations (ReCons) by balancing the performance of two operational modes, a global observation mode (GOM) and a regional observation mode (ROM) [3]. The orbits in two modes are both circular but have different altitudes, and the orbit can be switched via Hohmann transfers, as seen in Figure 1-1. Operational reconfiguration is distinct from staged deployment in that it happens after the constellation deployment is complete; therefore, the number of satellites remains constant and reconfiguration maneuvers happen throughout the satellite lifetime defined by the amount of carried fuel.

2.5 Chapter Summary

Throughout this chapter, the theories and applications of satellite orbits and constellations, in addition to previous research on reconfigurable constellations, were reviewed to obtain insights regarding the baseline ReCon concept. From the literature review, the following high-level decisions were made regarding the baseline ReCon architecture.

B-1 **ReCon Modes** - The ReCon shall have two modes, consisting of the global observation mode (GOM) and the regional observation mode (GOM).

B-2 **Global Observation Mode** - The GOM configuration shall be a Walker constellation consisting of circular orbits at non-repeating ground track (NRGT) altitudes.

B-3 **Regional Observation Mode** - The ROM configuration shall be circular orbits in repeating ground track (RGT) altitudes whose calculation shall include J_2 effects.

In addition to the baseline ReCon above, the following variants will also be considered as case studies to make the Earth observation more effective.

V-1 **Modified Walker Pattern** - The GOM configuration is assumed to be a non-uniform Walker constellation in order to reduce the reconfiguration time from GOM to ROM.

V-2 **Sun-synchronous ReCon** - The ROM configuration is assumed to be in sun-synchronous orbits to provide uniform lighting conditions at each revisit.

The baseline ReCon architecture will be described in Chapter 3, along with its optimization process in Chapter 4. The ReCon variants are discussed in Chapter 5.

Chapter 3

New ReCon Framework

In this chapter, a framework for modeling a ReCon design is established and evaluated. This framework consists of MATLAB modules and also interfaces with Satellite Tool Kit (STK) to improve accuracy of coverage calculations. To reiterate, the objective of optimizing a ReCon is:

> ***To*** *(1) minimize reconfigurable satellite constellation (ReCon) revisit time in both global observation and regional observation modes at given locations on the Earth, (2) minimize total system mass, and (3) minimize reconfiguration time* ***by*** *systematically changing orbit geometry design variables and satellite design variables* ***using*** *MSDO techniques* ***while*** *satisfying given resolution requirements for a given lifetime.*

In order to achieve this objective, the forward problem needs to be formulated first to which a wrapper optimization code can be applied. This can be done by defining appropriate variables and modules of ReCon as a system.

3.1 Model Overview

This section provides an overview of a simulation model for the ReCon optimization problem by listing its variables and modules. The types of variables include design variables, parameters, internal variables, constraints, and objectives. These variables are evaluated in each module and passed between the modules of the simulation model, whose flows can be better visualized by means of a block diagram and a design structure matrix (DSM).

3.1.1 Variables

Five types of variable have been identified for the Recon optimization problem in terms of their data type: design variables, internal variables, parameters, constraints, and objectives. The design variables define the satellite dimensions and the constellations geometry. Parameters are also related to the ReCon design, but their values are fixed under valid assumptions to simplify the problem. Internal variables are calculated from design variables and parameters inside a simulation module, which are then passed to other modules. Constraints are equalities or inequalities amongst design variables, internal variables, and parameters. Objectives are the figures of merit which measure the system performance of a ReCon design. These variables are summarized in Table 3.1.

Table 3.1: ReCon Variable List

	MATLAB Name	Description	Range	Units
Design Variables	nk	RGT ratio (τ)	[31/2, 15/1, 29/2, 14/1, 27/2, 13/1]	-
	delta_alt	Walker altitude difference from RGT	Governed by Altitude Constraints	km
	n_planes	# of planes in Walker constellation	[2, 3, 4, 5, 6, 7, 8, 9]	-
	n_sats	# of satellites per Walker plane	[1, 2, 3, 4, 5]	-
	regard	Field of regard	5 to 50	°
	prop	Propulsion type	[cold gas, monoprop, biprop]	-
Internal Variables	aperture	Optical telescope aperture diameter	Driven	m
	Fl	Optical telescope focal length	Driven	m
	prop_dry_mass	Propulsion system dry mass	Driven	kg
	propellant_mass	Propellant mass	Driven	kg
	optics_mass	Optical subsystem mass	Driven	m
	rgt_alt	Repeating ground track altitude	Driven	km
	delta_v	Total lifetime ΔV	Driven	m/s
	sat_dry_mass	Satellite dry mass	Driven	kg
Parameters	life	Orbit lifetime	5	years
	E	Orbit eccentricity	0 (circular)	-
	walker_phase	Satellite phasing between Walker planes	1 (equal)	-
	Inc	Orbit inclination	60	°
	n_recons	# of reconfigurations over lifetime	10	-
	gsd	Ground sample distance	1	m
	regional_lat	Regional Latitude of Interest	55	°
	global_lat_band	Global Latitude Band of Interest	0 to 60	°
	solar_case	Solar Case (min, mean, max)	2	-

Constraints	min_alt	Minimum altitude	350	km
	max_alt	Maximum altitude	1200	km
	max_regard	Maximum field of regard	50	°
	max_aperture	Maximum aperture diameter	1.8	m
	max_prop_frac	Maximum propellant mass fraction	0.3	-
Objectives	rom_revisit	ROM revisit time	Driven	s
	gom_coverage	GOM percent coverage	Driven	%
	const_mass	Constellation mass	Driven	kg
	reconfig_time	Reconfiguration time	Driven	days

First of all, design variables fall into two categories: orbit/constellation design and satellite subsystem design. The dual-configuration of a ReCon necessitates that orbits will be either GOM or ROM, so the orbit/constellation design variables are relevant to either of the two modes. It is assumed that the GOM configuration is a Walker constellation and ROM is accomplished by changing altitude from the default Walker constellation through a Hohmann transfer. The orbit/constellation design variables are as follows.

- $\tau = N_P/N_D$, or RGT ratio (ROM)
- Altitude difference from Walker constellation (GOM)
- Number of planes in the Walker constellation (GOM)
- Number of satellites per plane in the Walker constellation (GOM)

The RGT ratio can be interpreted as the number of satellite revolutions per day. The satellite subsystem design variables are as follows:

- Field of regard
- Propulsion type

In addition to design variables (quantities passed from the optimizer to the model), there are also internal variables passed between discipline-specific modules inside the model. The internal variables are listed in Table 3.1, including quantities related to optics subsystem sizing (aperture, focal length, payload mass) and propulsion subsystem sizing (delta-v, tanks mass, propellant mass). Note that the internal variables are driven by the choice of parameters and constraints.

Parameters are assumed values regarding the ReCon configuration and system operations. Specifically, our parameters are:

- ReCon lifetime (i.e., design life of the individual satellites, 5 years)
- Orbit eccentricity (assumed to be zero)
- Satellite phasing between Walker planes (assumed to be equally distributed, F=1 in Walker notation)
- Orbit inclination (limits the latitude bands of coverage, 60°)
- Number of reconfigurations over the system lifetime based on envisioned user needs, 10 times in 5 years)
- Ground sample distance (based on envisioned user needs, 1m)

Constraints reflect physical or technological limitations imposed on the aforementioned design variables and internal variables:

- Minimum altitude: The RGT altitude plus the Walker altitude difference must be greater than the minimum altitude threshold, i.e., `rgt_alt + delta_alt > alt_min`. As a practical matter, this will constrain the allowable range for the Walker altitude difference, since the RGT altitude is set based on what the n/k ratio is. The quantity `alt_min` was set to 350km from aerodynamic drag considerations.
- Maximum altitude: The RGT altitude plus the Walker altitude difference must be less than the maximum altitude threshold, i.e. `rgt_alt + delta_alt < alt_max`. The quantity `alt_max` was set to 1,200km based on considerations of the radiation environment at the higher LEO altitudes.
- Maximum field of regard: For a given altitude, the maximum field of regard (`max_regard`) is set as the angle at which the sensor image swath reaches the horizon. In this simulation, its value is 50°.
- Maximum aperture diameter: The telescope aperture diameter has to be constrained to maintain the satellite mass under the capacity of candidate launch vehicles. In this simulation, the maximum value has been set to 1.8m.

- Maximum propellant mass fraction: Technological constraints (e.g., material strength-to-weight ratios) will impose a maximum propellant mass fraction whose value is 0.3 in this simulation.

Our objectives vector consists of performance and cost quantities that we seek to balance via the proposed optimization. Amongst the performance metrics below, the designer can choose which metrics to use.

- Revisit time in regional observation mode (ROM)
- Revisit time in global observation mode (GOM)
- Area coverage in regional observation mode (ROM)
- Area coverage in global observation mode (GOM)
- Reconfiguration time (i.e., time to transition from GOM to ROM assuming Hohmann transfer)

As a cost metric, the mass of the entire constellation has been selected. Constellation mass has been selected as the first-order cost metric because it is closely related to manufacturing cost and launch cost.

- Constellation mass (i.e., wet mass of all the satellites in the constellation)

3.1.2 Modules

Table 3.2 shows the list of modules in the ReCon simulation model as well as the major inputs and outputs corresponding to each module. There are five modules which have been implemented and each module will be discussed in the following sections. Figure 3-1 shows the block diagram of the implemented simulation model along with inter-modular data flows. The black arrows represent the internal variables; the red arrows denote the objectives; and the other colors are design variables.

Table 3.2: ReCon Module List

Module	Inputs	Outputs
Astrodynamics	nk delta_alt n_planes n_sats regard e walker_phase inc	rgt_alt rom_revisit* gom_revisit*
Optics	regard delta_alt fov gsd rgt_alt	optics_mass aperture
Maneuvers	prop delta_alt life n_recons rgt_alt area	delta_v reconfig_time*
Propulsion	prop sat_dry_mass delta_v	prop_dry_mass propellant_mass
Constellation Properties	n_planes n_sats optics_mass aperture prop_dry_mass propellant_mass	sat_dry_mass const_mass* area

* Indicates objective vector output

This block diagram can also be represented as a DSM in Figure 3-2. It becomes more obvious that there are two nested iterative loops:

- First loop: between Constellation Properties and Propulsion modules
- Second loop: between the first loop and the Maneuvers module.

This coupling did not pose a problem in terms of computation because the execution time of these modules is orders of magnitude less than the computation time for the most demanding Astrodynamics module which runs STK simulations.

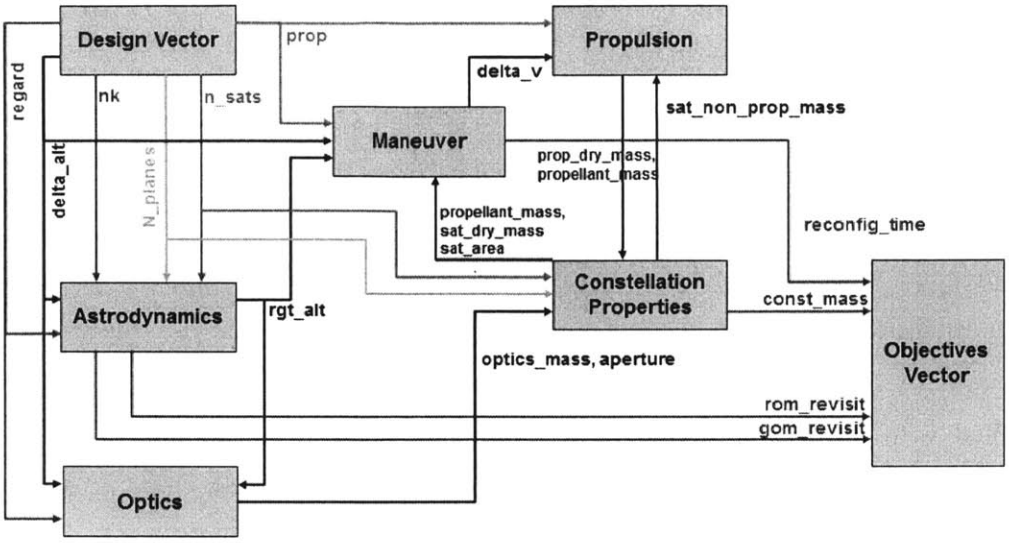

Figure 3-1: ReCon Simulation Model Block Diagram

Design Vector		nk, delta_alt, n_planes, n_sats, regard	regard, delta_alt	prop, delta_alt	prop	n_planes, n_sats	
	Parameters	e, walker_phase, inc	fov, gsd	life, n_recons			
		Astrodynamics	rgt_alt	rgt_alt			rom_revisit, gom_revisit
			Optics			optics_mass, aperture	
				Maneuvers	delta_v		reconfig_time
					Propulsion	prop_dry_mass, propellant_mass	
				area	sat_dry_mass	Constellation Properties	const_mass
							FOMs (Out)

Figure 3-2: ReCon Simulation Model DSM

3.2 Astrodynamics Module

The Astrodynamics module is the first module to be executed during a simulation run and is responsible for the following tasks:

- Generation of the constellation
- Propagation of the constellation in time to generate coverage statistics
- Computation of the observation duration and revisit time in GOM and ROM

The propagator currently includes up to J_4 effects of the local gravity of the Earth, but can be easily modified in STK to account for higher-order terms. Figure 3-3 shows the DSM again, but the Astrodynamics module is marked with bold edges and its direct data flows are represented with arrows. From the design variables (RGT ratio, altitude difference, the number of orbit planes, the number of satellites per orbit plane, and the field of regard) and the parameter values (eccentricity, walking phase parameter, and inclination), the module first calculates the RGT altitude with its iterative routines. The Astrodynamics module interfaces with STK to set up GOM/ROM constellations and retrieve the average revisit time in both modes.

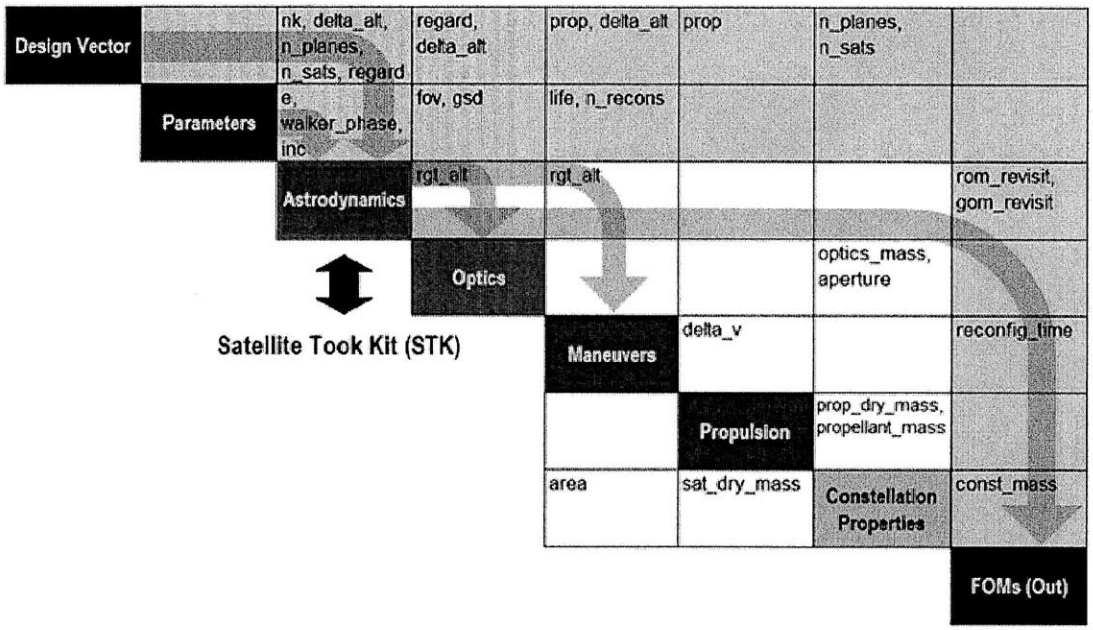

Figure 3-3: Astrodynamics Module in the ReCon DSM.

The interface between MATLAB and STK is described in more detail in Figure 3-4. The module starts out by computing the altitudes of both the ROM and GOM constellations given the design vector values as well as a number of parameters. Based on the given inclination

and calculated altitudes, the module then initializes the orbital elements of ROM and GOM constellations in STK using the stkConnect interface. After the setup is complete, MATLAB iterates time-based simulations on STK and retrieves figures of merit (FOM). STK was chosen to generate the constellation coverage statistics for its validated and accurate orbital propagation as well as its extensive library of built-in coverage functions.

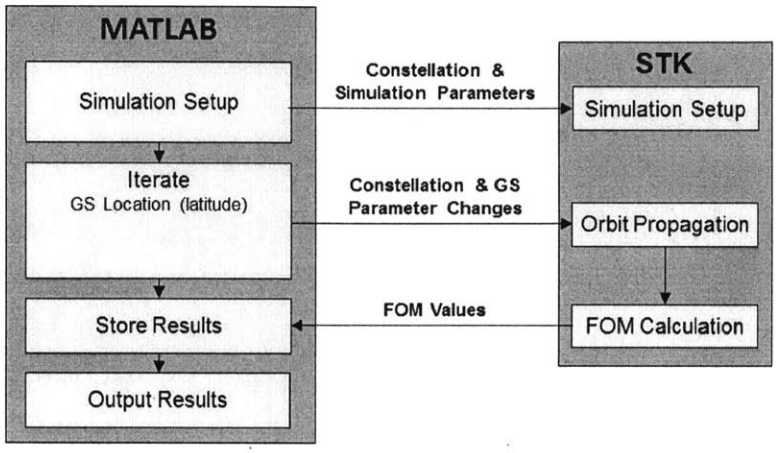

Figure 3-4: Astrodynamics Intra-Module Block Diagram.

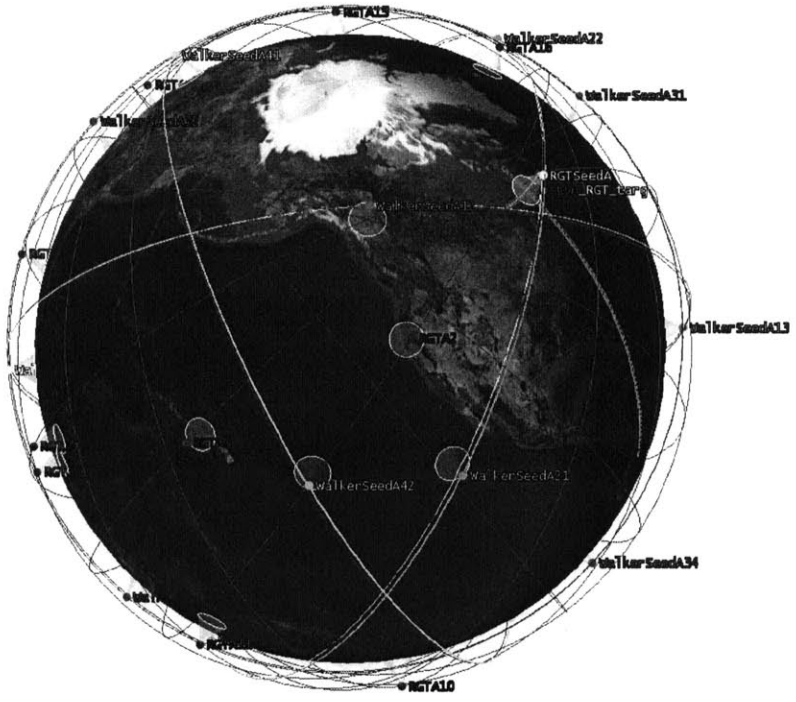

Figure 3-5: STK Constellations Setup [4]

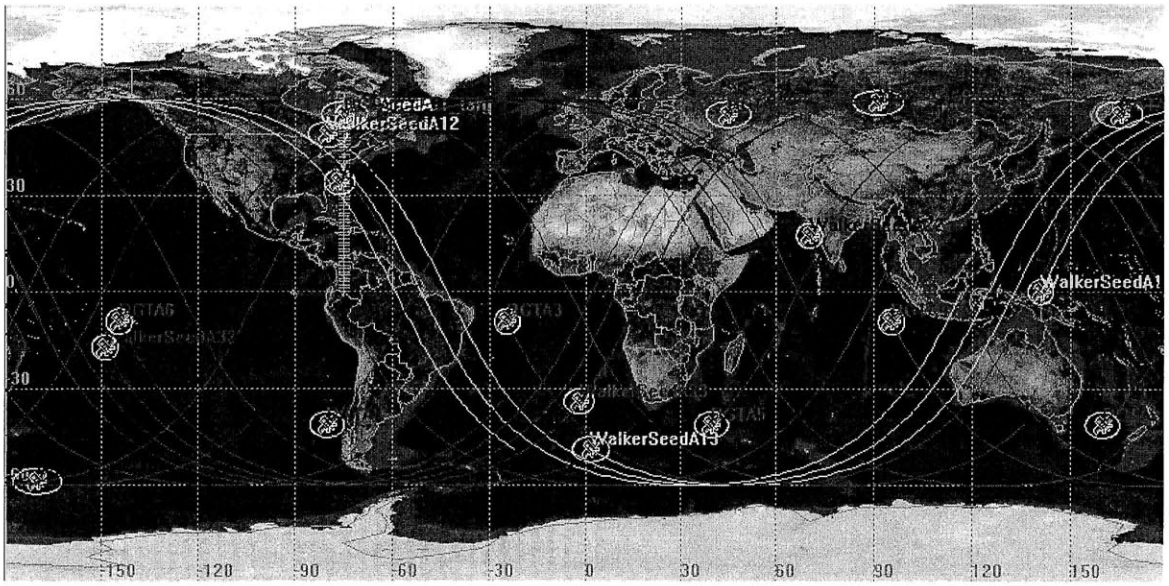

Figure 3-6: Ground Tracks of Constellations [4]

A three-dimensional Earth-centered view is shown in Figure 3-5. Both a ROM orbit and a GOM orbit have been set up and circles under satellites represent the field of view from on-board sensors. The RGT orbits considered here repeats after two days at most, so the STK simulations were run for two days in simulation time.

Figure 3-6 shows the corresponding ground tracks along with grid points on the ground for coverage calculations. Because there is no target of interest in GOM, the coverage statistics were gathered over the entire latitude band in the northern hemisphere which can be reached by the satellites, between the equator and 60°N, which is represented as light blue grids in the figure. In ROM, we have a target of interest whose latitude was assumed to be 55°N. These coverage figures of merit values are then output along with the altitude of the ROM constellation to other modules in the model.

3.3 Optics Module

The Optics module calculates the telescope aperture diameter (and its mass) required to achieve a particular ground sample distance (GSD) at a given altitude. In remote sensing, GSD, also referred to as ground-projected sample interval (GSI) or ground-projected instantaneous field of view (GIFOV) [57], is often defined as the distance between the centers of digital photo pixels projected on the ground. Figure 3-7 shows the optics module

highlighted in the DSM. The optics module accepts two altitude variables: the current RGT altitude calculated by the Astrodynamics module and the change in altitude provided by the design vector. The sum of these two values is the satellite altitude in GOM.

The optics module also accepts the field of regard (FoR) as an input from the design vector. The FoR value is used along with the higher altitude between GOM and ROM in order to determine the worst-case (maximum) slant range from the sensor to a target at the edge of the sensor view. This slant range is used for sizing the aperture diameter, as the payload must achieve the prescribed resolution at the edge of the FoR.

Once the slant range has been determined, the Optics module calculates the telescope aperture diameter. Another output is the telescope mass which can be estimated from a relationship obtained from an Earth-observation mission database. Although the Optics module does not produce objectives directly, it feeds the optics mass and the aperture size into the Constellation Properties module.

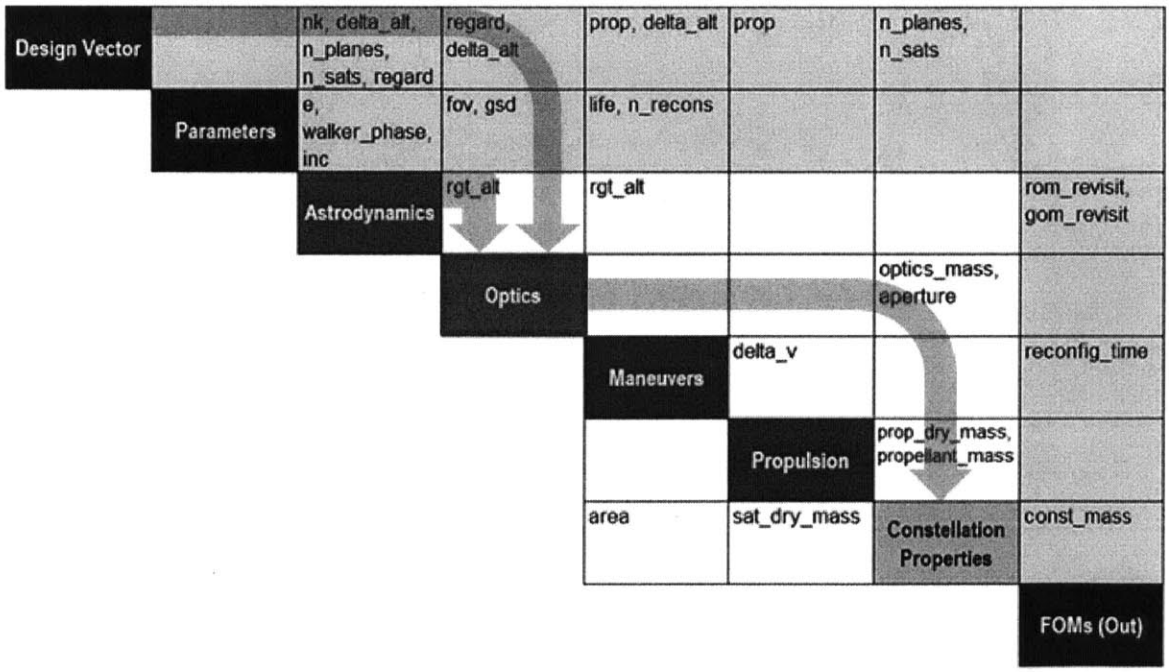

Figure 3-7: Optics Module in ReCon DSM

3.3.1 Telescope Aperture Diameter

As mentioned earlier, the GSD value is a parameter set prior to executing the simulation and corresponds to center-to-center distance of adjacent pixels (that is, the physical size of a

pixel, d, as shown in Figure 3-8(a)) projected onto the surface of the Earth. In the ReCon optimization problem, however, GSD instead is defined as the theoretical linear resolution limit which corresponds to the diameter of the ring, d', shown in Figure 3-8(b).

The standard Rayleigh diffraction criterion, as seen in Equation (3.1), calculates the distance from the center of the pattern to the first minimum of point spread function (the first radius of the first Airy ring) [58]. Figure 3-9 illustrates the definition of parameters, where θ is the angular resolution in radians, λ is the wavelength in meters, and D is the aperture diameter in meters.

$$\theta = 2.44\frac{\lambda}{D} \tag{3.1}$$

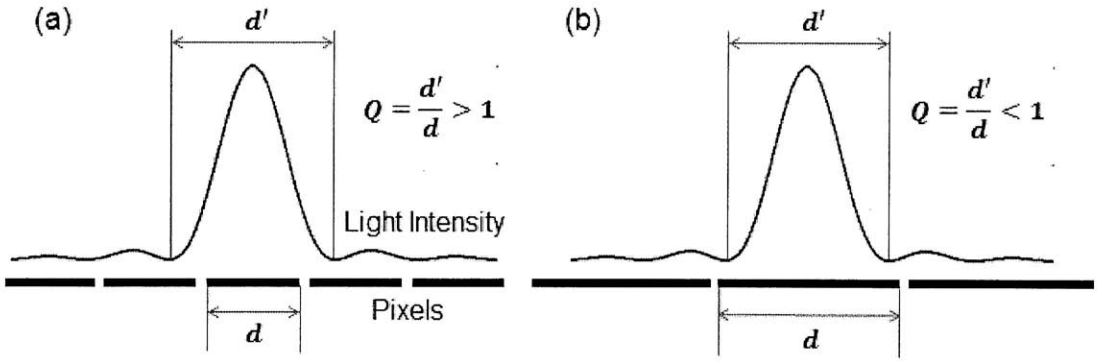

(a) Pixel-limited (b) Diffraction-limited

Figure 3-8: Relationship between Point Spread Function and Pixel Size according to Quality Factor [13]

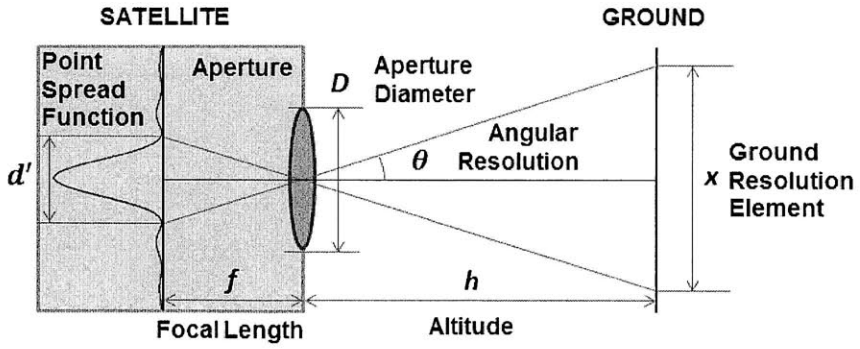

Figure 3-9: Optics Payload and Ground Resolution Element [13]

Figure 3-10 depicts the case when the satellite is no longer nadir-pointing, showing the aperture diameter (D), altitude (h), FoR (η), slant range (R_s), ground sample distance (GSD) and payload resolution element x. The angular resolution in Equation (3.1) is related to the linear resolution in Equation (3.2), from which the aperture needed for a given ground resolution x at nadir is calculated in Equation (3.3).

$$x = h\theta \tag{3.2}$$

$$D = 2.44\frac{\lambda h}{x} \tag{3.3}$$

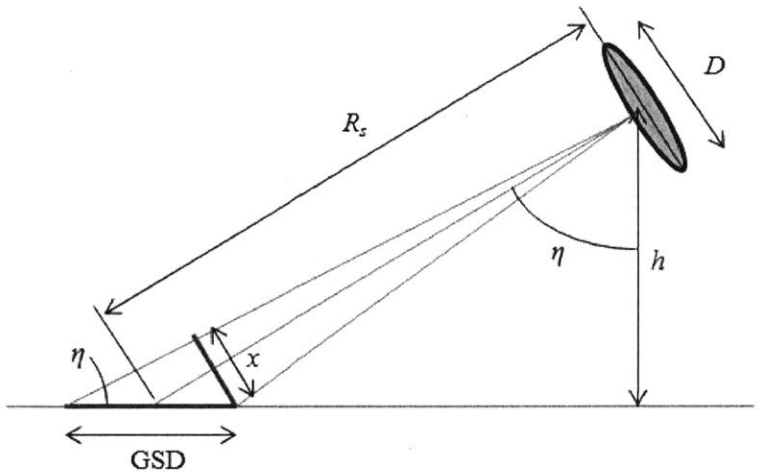

Figure 3-10: Imaging Geometry in the ReCon Optics Module

When the payload is oriented at the maximum FoR, the off-nadir angle is η and the slant range to the target is $R_s = h/\cos\eta$. The equation for aperture diameter therefore becomes:

$$D = 2.44\frac{\lambda R_s}{x} = 2.44\frac{\lambda h}{x\cos\eta} \tag{3.4}$$

The final part of the model is the relationship between the payload resolution element x and the projection of that element onto the ground (i.e. the GSD). At the edge of the FoR, a 1 m resolution element as viewed from the spacecraft will correspond to greater than 1 m on the ground when that resolution element is projected onto the Earth. Figure 3-10 illustrates this relationship that GSD is greater than x where x is the payload resolution element length

(normal to the optical axis of the payload). The relationship between payload resolution and GSD (i.e. ground projection) is therefore approximately

$$x = GSD\cos\eta \tag{3.5}$$

and the aperture diameter formula is given as Equation (3.6). The wavelength (λ) was assumed to be 500×10^{-9}m and GSD of 1m is assumed here.

$$D = 2.44\frac{\lambda h}{GSD\cos^2\eta} \tag{3.6}$$

3.3.2 Telescope Mass

The Optics module uses this aperture diameter to calculate the mass of the payload, including the primary mirror, optical telescope assembly (OTA), imagers, and supporting mechanical and electronic components. The mass calculation is done by considering an empirical relationship between the payload mass and the aperture size in Earth observation and astronomy missions. The database is provided in Table 3.3 [59] and the data points along with their fitting curve are plotted in Figure 3-11. From the data, the power law in Equation (3.7) could be obtained to approximate the payload (optics) mass from the given aperture size. The mass is in kilograms and the aperture diameter is in meters.

$$m_{optics} = 418.08 \cdot D^{1.37} \tag{3.7}$$

Table 3.3: Payload Aperture Size and Mass Data for Earth Observation Missions [59]

Spacecraft	Payload	Aperture [m]	Payload Mass [kg]
Quickbird	BHRC 60	0.6	380
WorldView-1	BHRC 60	0.6	380
Ikonos	OSA	0.7	171
GeoEye-1	GIS	1.1	452
OrbView-3	OHRIS	0.45	66
RapidEye	REIS	0.145	43
TopSat	RALCam 1	0.20	32

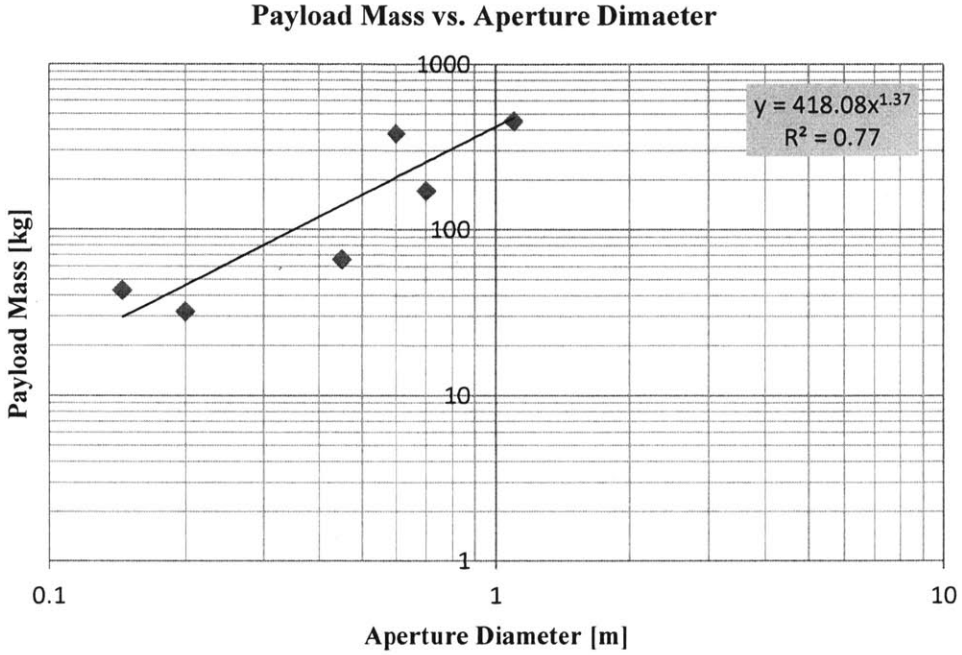

Figure 3-11: Correlation between Aperture Diameter and Payload Mass in Earth Observation Missions

3.4 Maneuvers Module

The Maneuvers module calculates the properties related to constellation reconfigurations in terms of time and fuel consumption. Figure 3-12 shows interaction of the maneuver module with other modules in the simulation. As inputs, the Maneuver module receives the propulsion type (`prop`) and altitude offset (`delta_alt`) from the design vector; design life (`life`) and number of reconfigurations (`n_recon`) from the parameter settings; and the RGT altitude from the Aerodynamics module (`rgt_alt`). As outputs, it generates the module delta-V (`delta-v`) and constellation reconfiguration time between GOM and ROM (`reconfig_time`).

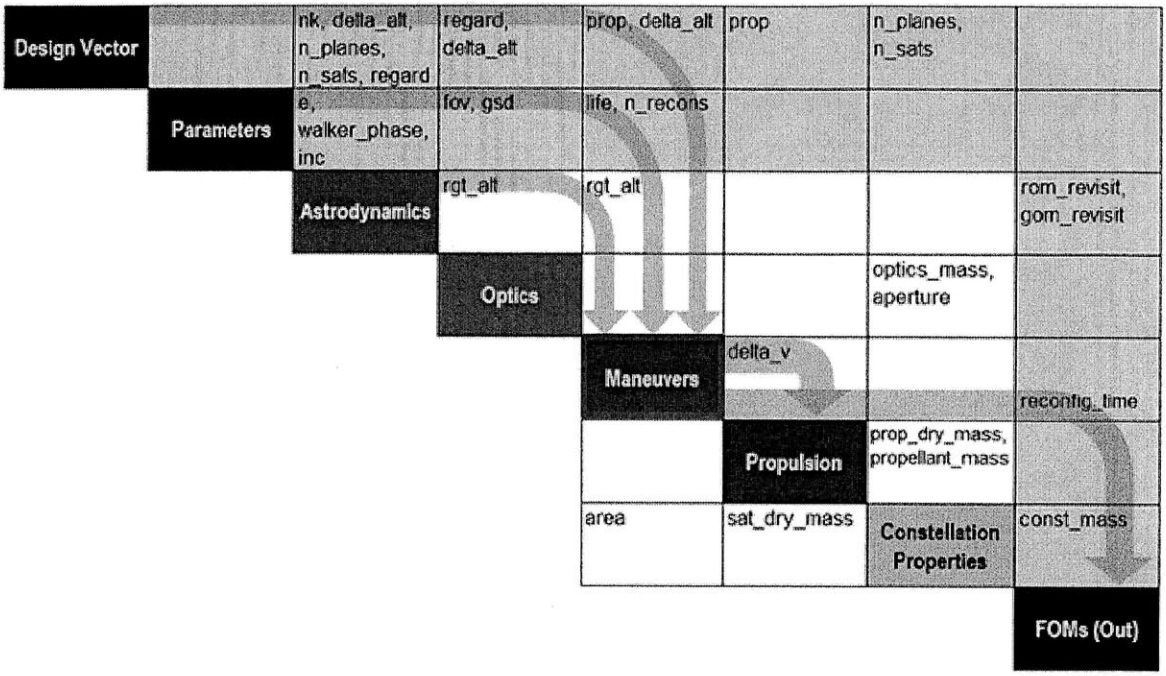

Figure 3-12: Maneuver Module in the ReCon DSM.

The following assumptions have been made regarding reconfiguration maneuvers in order to reduce the model complexity:

- The reconfiguration maneuver is a Hohmann transfer which uses two engine impulses.
- The reconfiguration maneuver occurs when the equator crossings of GOM and ROM ground tracks are aligned **exactly.** Under this assumption, the satellite path is slightly deviated from the desired RGT due to Earth's rotation during its Hohmann transfer. However, this drift during the orbit transfer can be ignored as long as the Hohmann transfer time (45~50 minutes) is significantly shorter than the GOM-ROM reconfiguration time (several days).

At the moment when a target of interest is identified, GOM and ROM ground tracks are usually not aligned for reconfiguration. This situation is illustrated as in Figure 3-13(a); red lines represent ROM ground tracks which pass through the target of interest; a yellow line represents the satellite's GOM ground track when the target is identified; and the two paths are separated by an angle of $\Delta\varphi$ at equator. If the GOM altitude is higher than the ROM altitude, the ground track of GOM drifts westward relative to that of ROM; if the GOM

altitude is lower than the ROM altitude, the GOM ground track drifts eastward. Therefore, the GOM ground track will overlap with the ROM ground track after several orbits, as shown in Figure 3-13(b), when the satellite can make an orbit transfer from GOM to ROM.

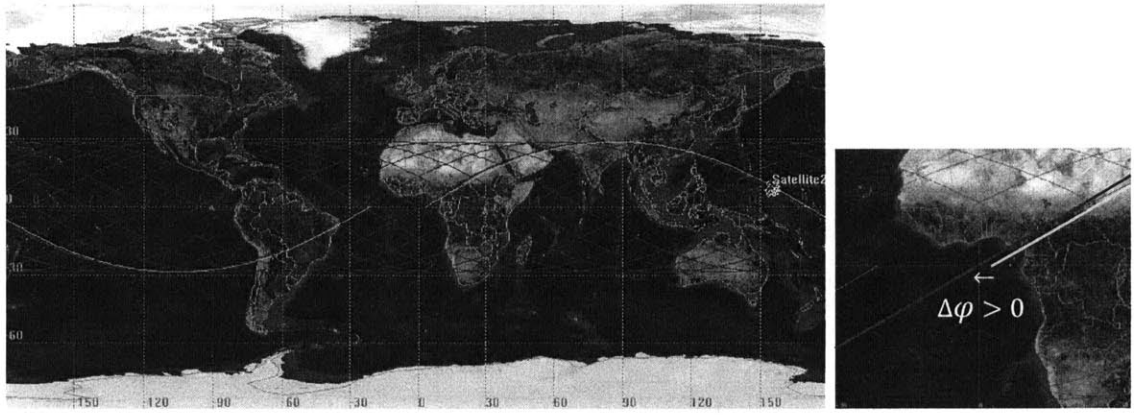

(a) Equator Crossings Misaligned

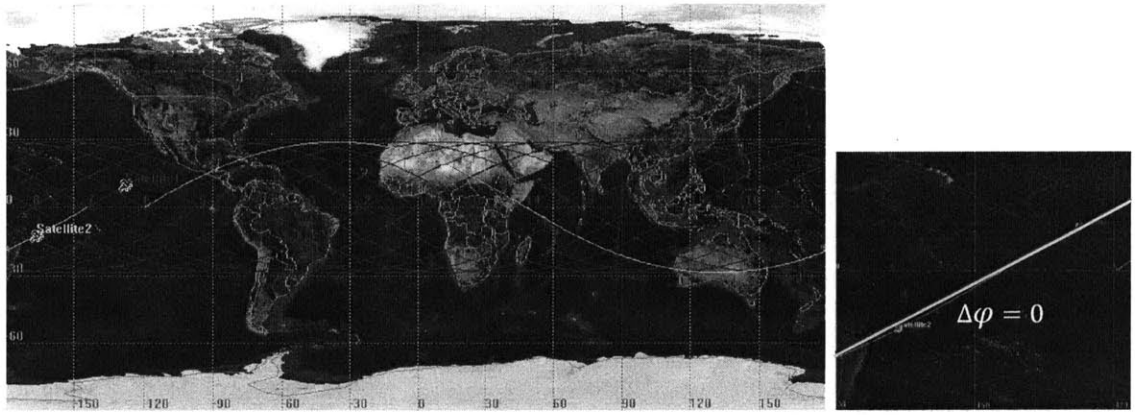

(b) Equator Crossings Aligned

Figure 3-13: Alignment of GOM and ROM Ground Tracks for Reconfiguration

3.4.1 Delta-V Budget

A satellite has to adjust its velocity, or produce delta-v (ΔV) throughout its life time. First, the satellite may have to propel itself in its commissioning phase if the designed orbit cannot be reached solely by the propulsion capabilities of the launch vehicle. While the satellite is operational, perturbing forces divert the satellite from its desirable path, which should be compensated for by changing its velocity. Also, a deorbiting burn might be required to decommission the satellite in a controlled way. In addition to these types of velocity changes performed by normal satellites, ReCon also requires frequent orbit reconfigurations which

should be included in the ΔV budget of its satellites. Table 3.3 displays the ΔV budget of a satellite in a ReCon.

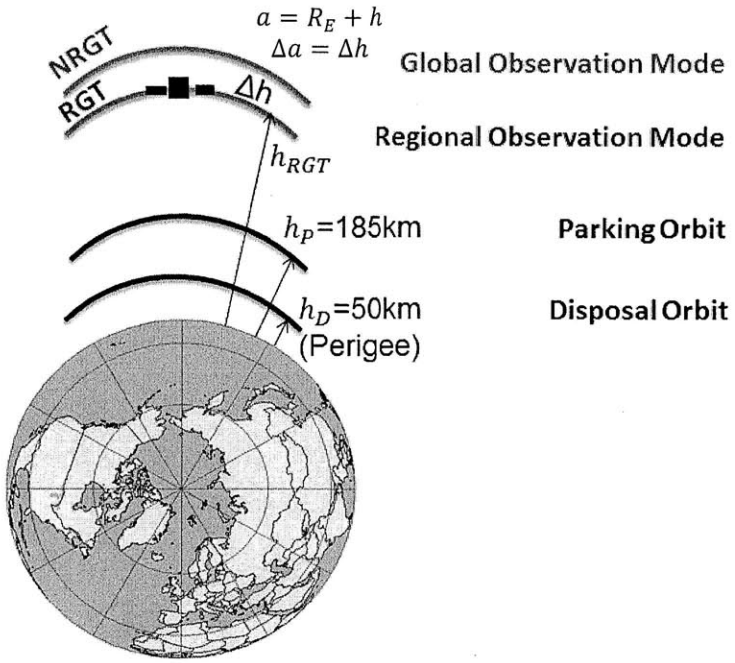

Figure 3-14: Orbit Definitions in ReCon

Table 3.4: ReCon Delta-V Budget

Delta-V	Definition	Number of Burns
Commissioning	From parking orbit to GOM orbit	1
Reconfiguration	From GOM(ROM) to ROM(GOM)	N = (Total number of reconfigurations during lifetime)
Station-keeping	Correct perturbations due to air drag and solar radiation	L = (Lifetime)*
Decommissioning	From GOM to disposal orbit	1

*Annual total counted as once per year

To be more specific, commissioning ΔV is the change in velocity required to raise the satellite from the parking orbit (h_P) to GOM orbit ($h_{RGT} + \Delta h$), as expressed in Equation (3.8). The parking orbit altitude is assumed to be h_P=185km (100 nautical miles), which can be reached by most launch vehicles [60, 61], to be conservative.

$$\Delta V_{commission} = \left|\sqrt{\frac{\mu_E}{R_E+h_{RGT}+\Delta h}} - \sqrt{\mu_E\left(\frac{2}{R_E+h_{RGT}+\Delta h} - \frac{1}{R_E+(h_{RGT}+\Delta h+h_P)/2}\right)}\right| + \left|\sqrt{\frac{\mu_E}{R_E+h_P}} - \sqrt{\mu_E\left(\frac{2}{R_E+h_P} - \frac{1}{R_E+(h_{RGT}+\Delta h+h_P)/2}\right)}\right| \quad (3.8)$$

Reconfiguration ΔV is the change in velocity required to transfer the satellite from GOM ($h_{\mathrm{RGT}} + \Delta h$) to ROM ($h_{\mathrm{RGT}}$) or vice versa and calculated from Equation (3.9).

$$\Delta V_{reconfig} = \left|\sqrt{\frac{\mu_E}{R_E+h_{RGT}+\Delta h}} - \sqrt{\mu_E\left(\frac{2}{R_E+h_{RGT}+\Delta h} - \frac{1}{R_E+h_{RGT}+\Delta h/2}\right)}\right| + \left|\sqrt{\frac{\mu_E}{R_E+h_{RGT}}} - \sqrt{\mu_E\left(\frac{2}{R_E+h_{RGT}} - \frac{1}{R_E+h_{RGT}+\Delta h/2}\right)}\right| \quad (3.9)$$

Equation (3.10) states that the station-keeping ΔV compensates for air-drag and solar radiation pressure (SRP). Velocity loss due to air drag, or ΔV required to compensate for it, is given in Equation (3.11); C_D is the drag coefficient of the satellite (typically 2.2); A is the cross-sectional area; ρ is the atmospheric density; m is the satellite mass; and V is its velocity. The quantity $m/C_D A$ is often defined as a ballistic coefficient, and an object with a higher ballistic coefficient can overcome air resistance better in flight [57]. The atmospheric density is an exponentially decaying function of altitude and the orbital velocity is proportional to the square root of the sum of Earth radius and altitude. Therefore, the altitude (h) which maximizes the multiplication of two, $\rho(h)\sqrt{R_E + h}$, is selected between h_{RGT} and $h_{RGT} + \Delta h$ for a conservative estimation. Delta-v for solar radiation pressure (SRP) is set to be 30m/s per year, which is the upper boundary in LEO suggested by literature [62]; because the SRP is independent of altitude, it is assumed to be constant.

$$\Delta V_{stationkeeping} = \Delta V_{airdrag} + \Delta V_{solar} \quad (3.10)$$

$$\Delta V_{airdrag} = \frac{\pi C_D A}{m}\rho a V = \frac{\pi C_D A}{m}\rho\sqrt{\mu_E(R_E + h)}$$

$$= \frac{\pi C_D A\sqrt{\mu_E}}{m} max\{\rho(h_{RGT})\sqrt{R_E + h_{RGT}}, \rho(h_{RGT} + \Delta h)\sqrt{R_E + h_{RGT} + \Delta h}\} \quad (3.11)$$

$$\Delta V_{solar} = 30\ m/s/yr \quad (3.12)$$

Decommissioning ΔV transfers the satellite in GOM to a decommissioning orbit which is an ellipse with the apogee altitude $R_E + h_{RGT}$ and the perigee altitude h_D. The perigee altitude, or disposal altitude, is set to be h_D=50km.

$$\Delta V_{decommission} = \left| \sqrt{\frac{\mu_E}{R_E+h_{RGT}+\Delta h}} - \sqrt{\mu_E \left(\frac{2}{R_E+h_{RGT}+\Delta h} - \frac{1}{R_E+(h_{RGT}+h_D)/2} \right)} \right| \quad (3.13)$$

Thus, total ΔV is the summation of all components multiplied by number of burns, given by Equation (3.14).

$$\Delta V_{total} = \Delta V_{commission} + \Delta V_{decommission} + L\Delta V_{stationkeeping} + N_{reconfig}\, \Delta V_{reconfig} \quad (3.14)$$

3.4.2 Reconfiguration Time

The reconfiguration time is defined as the period from the target identification to the alignment of round tracks in GOM and ROM. The duration of a Hohmann transfer was assumed to be negligible compared to the waiting time for alignment. If the NRGT altitude is $a + \Delta a$ and the RGT altitude is a, the difference of periods of the two orbits is given by:

$$\Delta T = 2\pi \left(\sqrt{\frac{(a+\Delta a)^3}{\mu_E}} - \sqrt{\frac{a^3}{\mu_E}} \right) \quad (3.15)$$

If $\Delta a > 0$, a satellite in the NRGT orbit will take a longer time to complete a revolution than a satellite in the RGT orbit. This lagging causes a westward drift of the NRGT orbit relative to the ground-fixed RGT. The distance by which the NRGT deviates from the RGT at equator after one orbit is:

$$\Delta d = (\omega_E - \dot{\Omega}) R_E \Delta T \quad (3.16)$$

For an orbit in which a satellite orbits around the Earth N_P times in N_D days ($\tau = N_P/N_D$), the deviating distance along the surface occurring in N_D days is:

$$N_P \Delta d = N_P(\omega_E - \dot{\Omega}) R_E \Delta T \tag{3.17}$$

Suppose that the NRGT orbit plane has to move by an angular distance (longitudinal difference) of $\Delta\varphi$ measured along the equator to align with its corresponding RGT orbit plane. Then, the required time for reconfiguration in days is given by

$$T_R = \frac{2\pi R_E \Delta\varphi}{N_P \Delta d} = \frac{2\pi R_E \Delta\varphi}{N_P(\omega_E - \dot{\Omega}) 2\pi R_E \left(\sqrt{\frac{(a+\Delta a)^3}{\mu_E}} - \sqrt{\frac{a^3}{\mu_E}} \right)} = \frac{\Delta\varphi}{N_P(\omega_E - \dot{\Omega}) \left(\sqrt{\frac{(a+\Delta a)^3}{\mu_E}} - \sqrt{\frac{a^3}{\mu_E}} \right)} \tag{3.18}$$

Figure 3-15 shows a sample constellation with six orbit planes near τ=1/15 RGT orbits. The orbit planes in GOM are 60°apart from each other as defined by Walker patterns. The ground track is assumed to pass through (0, 0) in the latitude-longitude plot. The other equator crossings are 24° (=360°/15) apart from one another. The figure describes a case where the satellites have just missed (0, 0), (60, 0), (120, 0), (180, 0), (240, 0), and (300, 0) which are possible transfer locations from GOM to ROM. The angular distance $\Delta\varphi$ differs amongst equator crossings, either 24° or 12°, meaning that some satellites are well-conditioned and others are ill-conditioned. The worst-case traverse angle was obtained by averaging $\Delta\varphi$ over all possible longitudes of target locations. In the case described here, the average $\Delta\varphi$ is approximately 18°.

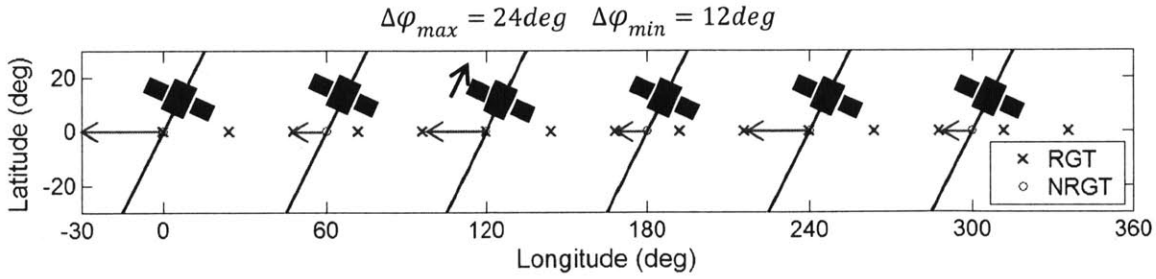

Figure 3-15: Traverse Angle from GOM to ROM

3.5 Propulsion Module

The Propulsion module is tasked with computing both the propellant mass (`propellant_mass`) and the dry mass of the propulsion subsystem (`prop_dry_mass`) from the propellant type (`prop`), delta-v (`delta_v`) and the satellite dry mass (`delta_v`). The `prop` variable in the design vector specifies the type of propulsion system, either cold gas or monopropellant. The Propulsion module is highlighted in the ReCon DSM in Figure 3-15.

Figure 3-16 defines the mass composition of a satellite. From the perspective of the Propulsion module, the total mass of a satellite consists of non-propulsion subsystem dry mass ($m_{dry,no\ prop}$), propulsion subsystem dry mass ($m_{dry,prop}$), and propellant mass (m_p). Non-propulsion subsystem dry mass is then subdivided into non-optics subsystem mass ($m_{dry,no\ optics}$) and optics subsystem mass (m_{optics}), which was calculated in the Optics module.

$$m_{sat} = m_{dry,no\ prop} + m_{dry,prop} + m_p = m_{dry,no\ optics} + m_{optics} + m_{dry,prop} + m_p \quad (3.19)$$

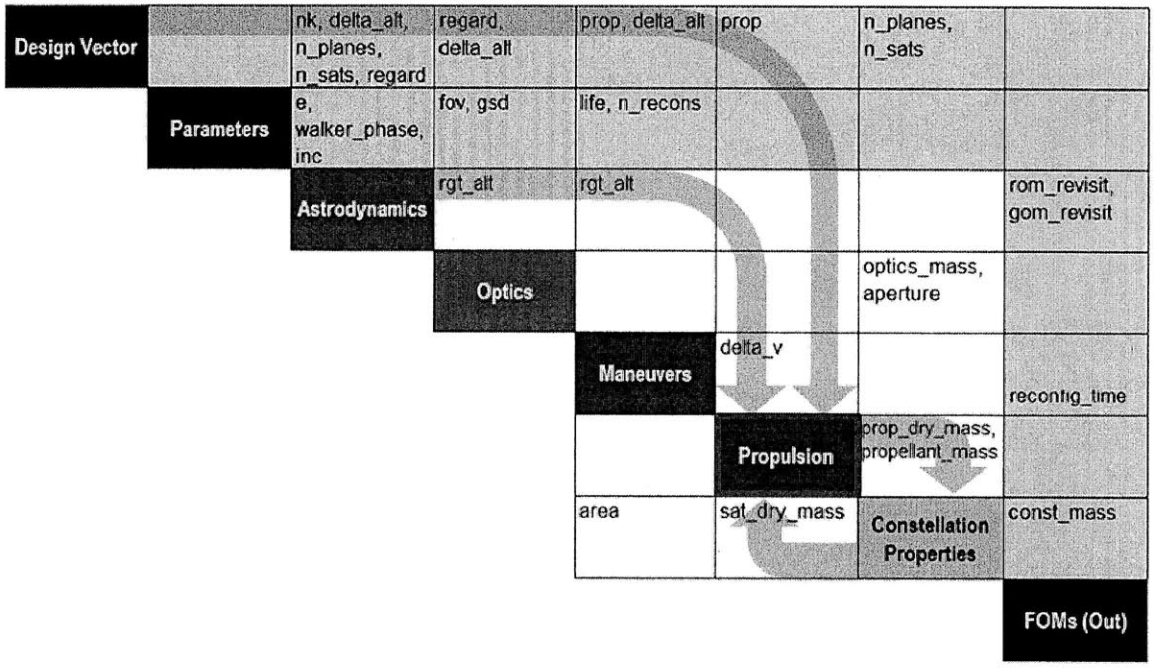

Figure 3-16: Propulsion Module in ReCon DSM

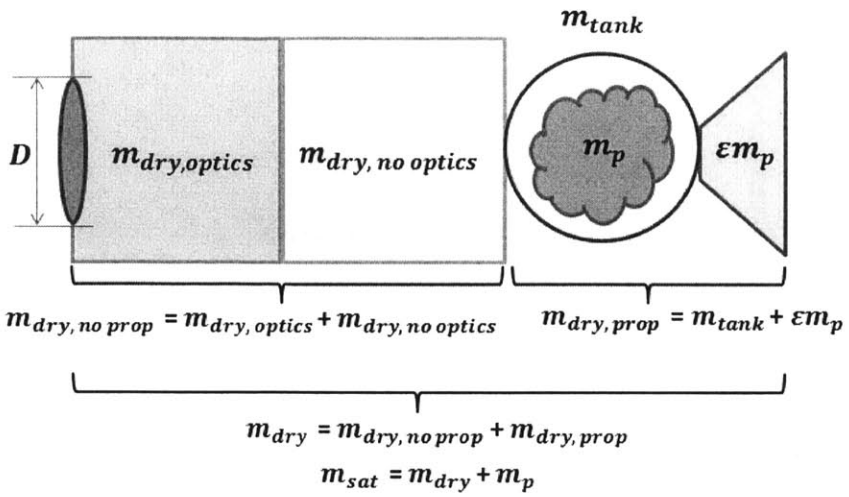

Figure 3-17: Satellite Mass Composition

The propulsion subsystem dry mass ($m_{dry,prop}$) is comprised of the tankage mass (m_{tank}) and some additional mass for propellant feed and thruster which is taken as a fixed percentage of the propellant mass as shown below:

$$m_{dry,prop} = m_{tank} + \varepsilon\, m_p \tag{3.20}$$

Where ε accounts for the additional hardware required for propellant feed control and the thrusters. An empirical fit is used to estimate the tank mass for high pressure cold gas systems and that for liquid monopropellant systems, which are plotted in Figure 3-17 and Figure 3-18, respectively [13, 58, 59, 60, 61]. The tank data comes from a variety of spacecraft propellant tank manufacturers and spans many orders of magnitude in terms of propellant capacity. The cold gas propellant tank data assumes a 4500 psi storage pressure and composite overwrapped pressure vessel (COPV) construction. Data is from ATK, Worthington Cylinders and HyperComp Engineering. For validation, an empirical relation is used from SMAD for 4500 psi composite pressure vessels which shows a fairly good fit for the higher volume tanks, but overpredicts mass for the smaller tanks. The liquid monopropellant tank data contains both tanks with propellant management devices (PMD) and internal diaphragms from ATK and EADS Astrium. Also included are two empirical fits from SMAD which fit the power law well over the range of propellant capacity in available database.

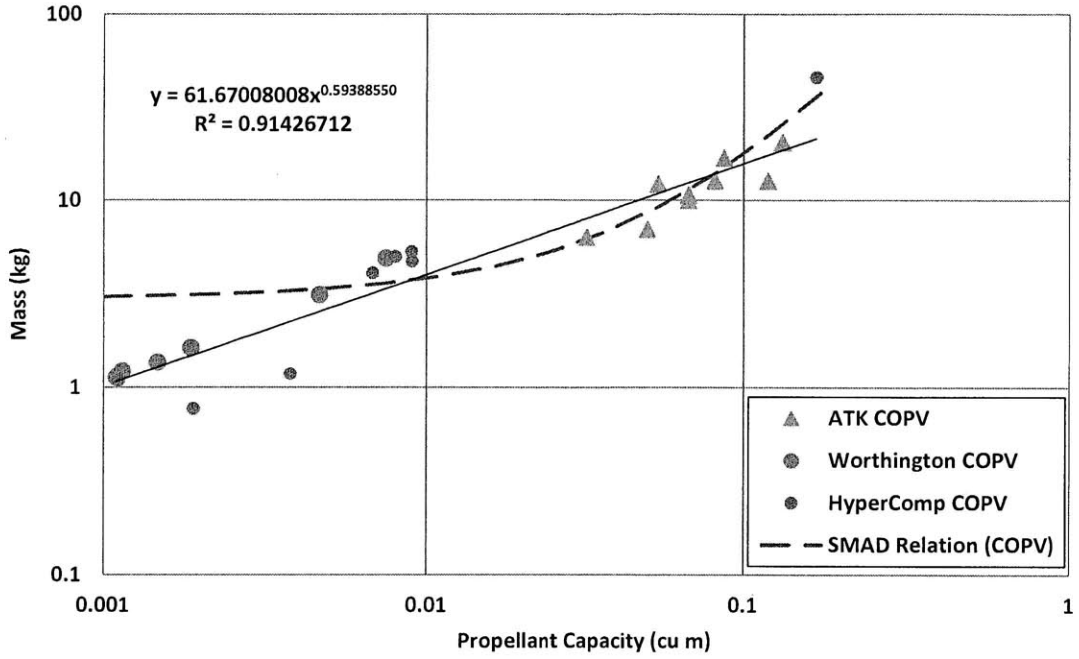

Figure 3-18: Cold Gas Propellant Tank Data and Curve Fit [13, 63, 64, 65]

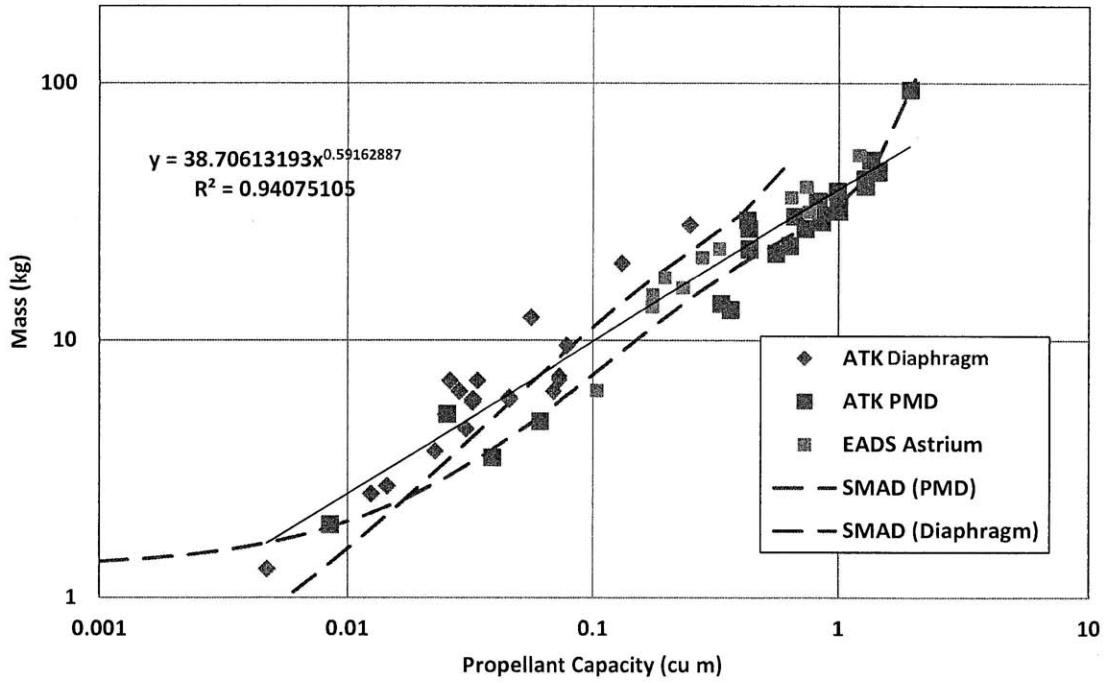

Figure 3-19: Liquid Monopropellant Tank Data and Curve Fit [13, 63, 66]

The empirical tank relationships are then:

$$\text{Cold Gas:} \quad m_{tank} = 61.67008008 \times (V_{tank})^{0.59388550} \tag{3.21}$$

$$\text{Liquid Monopropellant:} \quad m_{tank} = 38.70613193 \times (V_{tank})^{0.59162887} \tag{3.22}$$

The required tank propellant volume is also given by the mass of the propellant, m_p, divided by the propellant storage density, ρ_{prop}:

$$V_{tank} = \frac{m_p}{\rho_{prop}} \tag{3.23}$$

Next, the rocket equation is used to relate the initial mass to the final mass after all propellant is depleted as a function of the specific impulse of the propulsion system and the required mission delta-v:

$$m_0 = (m_0 - m_p)e^{\Delta V/g\, I_{SP}} \tag{3.24}$$

$$m_{dry} + m_{dry,prop} + m_p = (m_{dry} + m_{dry,prop})e^{\Delta V/g\, I_{SP}} \tag{3.25}$$

$$m_{dry} + m_{tank} + \varepsilon\, m_p + m_p = (m_{dry} + m_{tank} + \varepsilon\, m_p)e^{\Delta V/g\, I_{SP}} \tag{3.26}$$

The tank mass relations can then be added in for cold gas:

$$m_{dry} + 61.67008008 \times \left(\frac{m_p}{\rho_{prop}}\right)^{0.59388550} + \varepsilon\, m_p + m_p$$
$$= \left(m_{dry} + 61.67008008 \times \left(\frac{m_p}{\rho_{prop}}\right)^{0.59388550} + \varepsilon\, m_p\right) e^{\Delta V/g\, I_{SP}} \tag{3.27}$$

And for liquid monopropellant:

$$m_{dry} + 38.70613193 \times \left(\frac{m_p}{\rho_{prop}}\right)^{0.59162887} + \varepsilon\, m_p + m_p =$$
$$\left(m_{dry} + 38.70613193 \times \left(\frac{m_p}{\rho_{prop}}\right)^{0.59162887} + \varepsilon\, m_p\right) e^{\Delta V/g\, I_{SP}} \tag{3.28}$$

These relations are then solved to yield propellant mass (m_p) for a given non-propulsion bus dry mass (m_{dry}) using a Newton solver. Note that gaseous nitrogen was assumed for cold-gas implementation with a specific impulse of 65 seconds and a density of 302.18kg/m^3 at 4500 psi and 300K. For monopropellant, hydrazine was assumed with a specific impulse of 220 seconds and a density of 1021kg/m^3 at 400 psi and 300K.

3.6 Constellation Properties Module

The Constellation Properties module is tasked with computing the satellite dry mass (`sat_dry_mass`: m_{dry}), the total constellation mass (`const_mass`), and the estimated cross-sectional area of the satellites (`area`) from the number of planes, the number of satellites, optics mass, propulsion subsystem dry mass, and propellant mass.

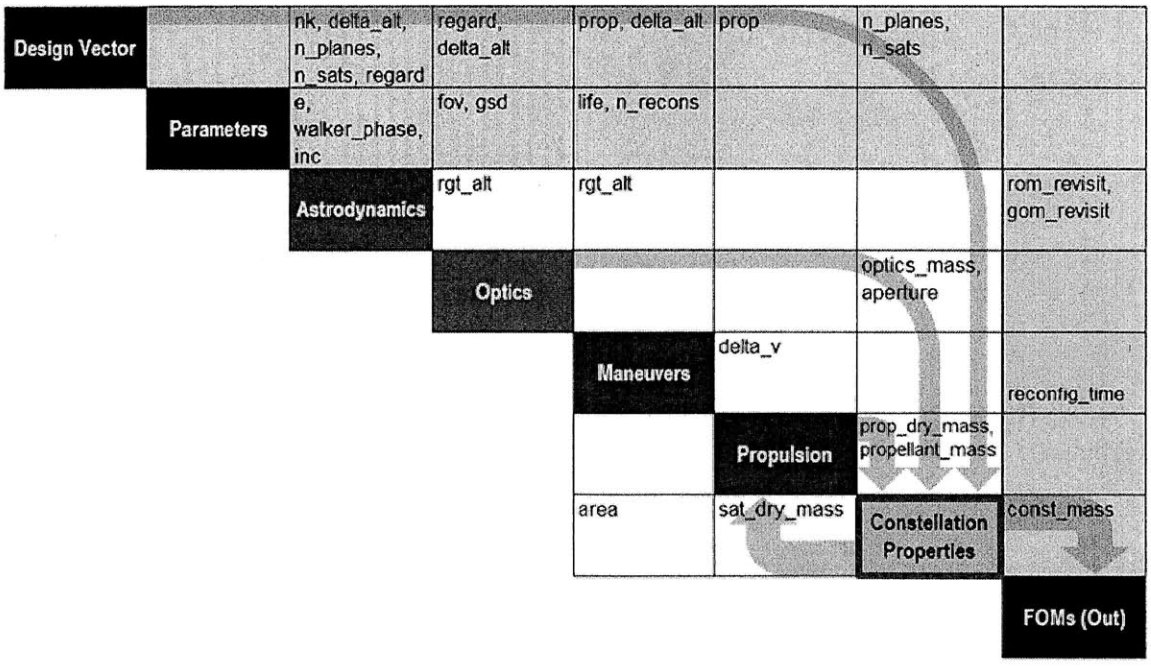

Figure 3-20: Constellation Module in ReCon DSM

The bus dry mass is computed using a curve fitted to the primary aperture diameter of historical observation satellite data as shown in Figure 3-21 [56].

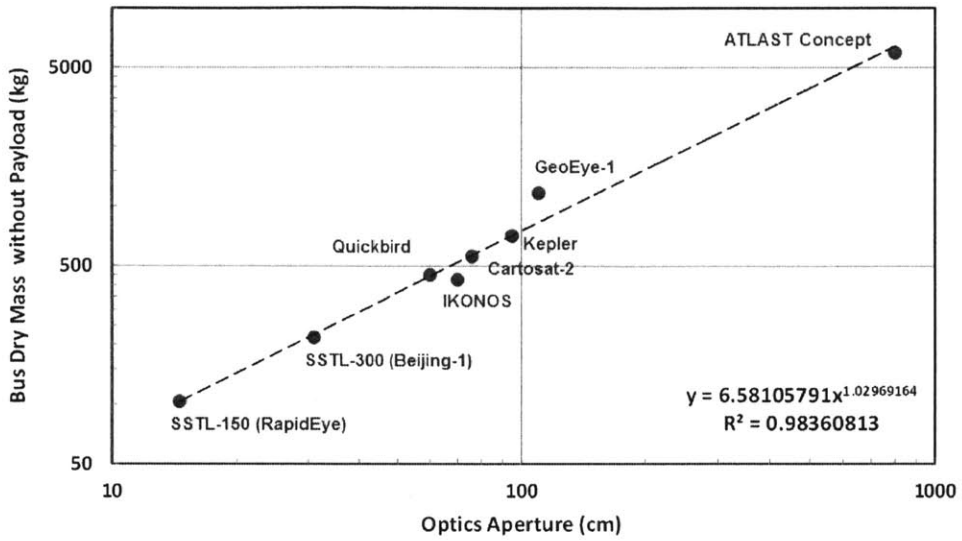

Figure 3-21: Bus Dry Mass without Payload vs. Optics Aperture Diameter for Historical Earth Observation Missions [56]

The power law curve fit shows good fit to the data and yields the following relation for the bus dry mass, not including the optical payload mass, as a function of the aperture diameter, D, in centimeters:

$$m_{dry,no\ optics} = 6.58105791D^{1.02969164} \tag{3.29}$$

The dry mass is then added to the optical payload, propellant subsystem dry mass, and propellant mass to yield the total mass of a single satellite:

$$m_{sat} = m_{dry,no\ optics} + m_{optics} + m_{dry,prop} + m_p \tag{3.30}$$

where m_{optics} is calculated by the optics module, and $m_{dry,prop}$ and m_p are calculated by the propulsion module. The total constellation mass is then computed as:

$$m_{const} = m_{sat} \times n_{planes} \times n_{sats} \tag{3.31}$$

where n_{planes} is the number of planes in the initial Walker constellation (P in the Walker notation) and n_{sats} is the number of satellites in each initial Walker plane.

The cross-sectional area of the satellite is then computed knowing the total satellite mass, assuming a spherical geometry and a satellite density parameter. The area will be used by the maneuvers module to predict atmospheric drag ΔV and is given by:

$$A = \pi \left(\frac{3\, m_{sat}}{4\pi\, \rho_{sat}} \right)^{\frac{2}{3}} \tag{3.32}$$

The density of the satellite, ρ_{sat}, is assumed to be 500kg/m^3 [67].

3.7 Single-Run Example

After integrating all modules, a one-time simulation was run as an example with a set of inputs summarized in Table 3.5.

Table 3.5: Example ReCon Design

	MATLAB Name	Value	Units
Design Variables	nk	15/1	-
	delta_alt	+40	km
	n_planes	3	-
	n_sats	3	-
	Regard	40	°
	Prop	2 (monopropellant)	-
Constraints	min_alt	350	km
	max_alt	1200	km
	max_regard	50	-
	max_aperture	1.8	m
	max_prop_frac	0.3	-
	Life	5	year
Parameters	E	0	-
	walker_phase	1	-
	Inc	60	°
	n_recons	10	-
	Gsd	1	m
	Fov	5	°
	rom_latitude	55	°
	global_lat_band	{0,60,1}	°
	solar_case	2	-

This constellation design corresponds to a design vector of:

$$\mathbf{x} = \begin{bmatrix} Satellite\ revolutions\ per\ day \\ Altitude\ difference\ (km) \\ Number\ of\ orbit\ planes \\ Number\ of\ satellites\ per\ plane \\ Field\ of\ regard\ (°) \\ Propellant\ type \end{bmatrix} = \begin{bmatrix} N_P/N_D \\ \Delta h \\ n_{planes} \\ n_{sats} \\ \eta \\ prop \end{bmatrix} = \begin{bmatrix} 15/1 \\ 40 \\ 3 \\ 3 \\ 40 \\ 2 \end{bmatrix} \tag{3.33}$$

Given these parameters, the resulting objectives vector and the constraints vector are then computed as:

$$J(\mathbf{x}) = \begin{bmatrix} GOM\ revisit\ time\ (s) \\ ROM\ revisit\ time\ (s) \\ Constellation\ mass\ (kg) \\ Reconfiguration\ time\ (day) \end{bmatrix} = \begin{bmatrix} 3048 \\ 19559 \\ 17422 \\ 3.95 \end{bmatrix} \tag{3.34}$$

$$g(\mathbf{x}) = \begin{bmatrix} Violation\ of\ minimum\ altitude\ constraint \\ Violation\ of\ maximum\ altitude\ constraint \\ Violation\ of\ maximum\ field\ of\ regard\ constraint \\ Violation\ of\ maximum\ \ aperture\ diameter\ constraint \\ Violation\ of\ maximum\ \ propellant\ mass\ ratio \end{bmatrix}$$

$$= \begin{bmatrix} h_{min} - min\{h_{RGT}, h_{RGT} + \Delta h\} \\ max\{h_{RGT}, h_{RGT} + \Delta h\} - h_{max} \\ \eta - \eta_{max} \\ D - D_{max} \\ \frac{m_p}{m_{dry}+m_p} - \zeta_{max} \end{bmatrix} = \begin{bmatrix} -116 \\ -654 \\ -27.9 \\ -0.665 \\ -0.028 \end{bmatrix} \tag{3.35}$$

The objectives vector, $J(\mathbf{x})$, means that the constellation has a regional coverage revisit time of 3048 seconds (0.847 hours), a global revisit time of 19559 seconds (5.433 hours), a total mass of 17,422kg and a reconfiguration time between GOM and ROM of 3.95 days. In this example, coverage duration for GOM and ROM were not included in the objectives vector, but the metrics can be included in or excluded from the objectives vector as necessary. The constraints vector, $g(\mathbf{x})$, has only negative entries, which show that all inequality constraints are satisfied.

3.8 Chapter Summary

In this chapter, a ReCon simulation model to predict the constellation mass and performance was described. In particular, this MATLAB model interacts with STK to compute the coverage performance, such as revisit time and observation duration, with high accuracy. The reconfiguration time and delta-v are calculated from the principles of astrodynamics. The database of previous Earth observation missions was used to estimate the mass of each subsystem from payload dimensions. Thus, these components constitute a "forward problem," whose boundary is represented by dashed lines in Figure 3-22, which is wrapped by an optimizer. The next chapter will discuss how a wide variety of optimization techniques are applied to this model to find optimal ReCon reconfigurations.

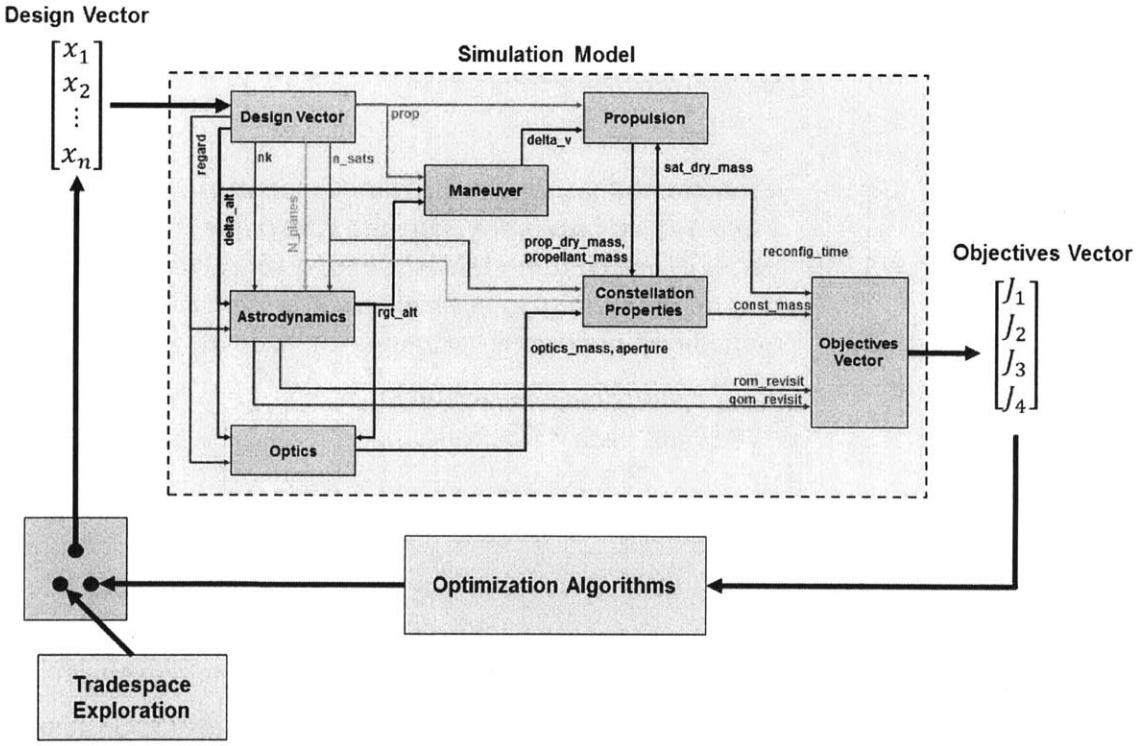

Figure 3-22: ReCon Optimization Framework

Chapter 4

ReCon Optmization

As the ReCon framework was refined, optimization of the ReCon design was performed concurrently for a single-layered ReCon. The term "single-layer" is defined as a constellation characteristic such that all satellites have orbits with an identical altitude, eccentricity, and inclination. If the orbits of satellites are grouped into multiple sets of these orbital elements, the constellation is considered to be "multi-layered," which can be further specified into double-layered, triple-layered, etc. For simplicity, the scope of this thesis is confined to the single-layered case.

A design of experiments (DOE) was first conducted to gain insights regarding the effects of ReCon design variables on the objectives. After that, heuristic optimization methods including the simulated annealing (SA) and the genetic algorithm (GA) were applied to find optimal designs for a single-objective case where all figures of merit are merged to single utility. The problem was then extended to a multi-objective problem to obtain a set of non-dominated designs along the Pareto front.

4.1 Design of Experiments

An initial exploration of the design space was carried out using Latin hypercube sampling (LHS). Amongst a variety of DOE techniques, LHS was chosen because it requires a lower number of computations compared to others. LHS divides the design space into l divisions (levels of value) for each of n factors (variables) and combines them in a random (non-reproducible) manner. A square grid containing samples is called a Latin square if and only if there is only one sample in each row and each column [68], as illustrated in Figure 4-1 where

the design space consists of two factors with four levels each. This can be extended to a multidimensional distribution, where there is only one sample in a hyperplane in each axis.

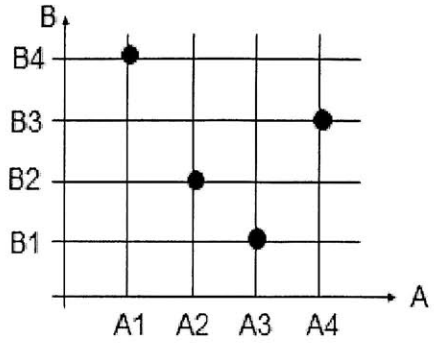

Figure 4-1: Latin Hypercube with Two Factors (A, B) and Four Levels (1, 2, 3, 4)

In a single-layered ReCon problem, five factors were used as established in the framework because the sixth variable (propellant) type had been frozen as monopropellant. Table 4.1 shows the factors and levels used for the experiment. Four levels were chosen for the n/k ratio, number of planes, and number of satellites per plane; eight levels for the Walker altitude difference and FoR to achieve a finer resolution; therefore, a total of 4096 combinations are possible. The selections were made to cover the range of likely design variable inputs for optimization. Due to the way LHS is implemented, the number of levels of a given factor must be an integer multiple of the number of levels of any other factor (hence the choice of 4 and 8 levels).

Table 4.1: Factors and Levels used in Latin Hypercube Sampling

Design Variable	Factor Symbol	MATLAB Name	Levels	Units
RGT ratio	N	`nk`	[31/2, 15/1, 29/2, 14/1]	-
Altitude difference between Walker and RGT	A	`delta_alt`	[-40, -30, -20, -10, 10, 20, 30, 40]	km
Number of planes	P	`n_planes`	[1, 2, 3, 4]	-
Number of satellites per plane	S	`n_sats`	[2, 3, 4, 5]	-
Field of regard	R	`Regard`	[5, 10, 15, 20, 25, 30, 35, 40]	°

A Latin hypercube sample of 100 design points was created using a MATLAB built-in function, `lhsdesign`. The combinations were saved to a spreadsheet that the ReCon model referenced when evaluating the design points. At each point, the model output the four

figures of merit of interest: ROM revisit time, GOM revisit time, constellation mass, and reconfiguration time. Table 4.2 shows the main effects of the levels of each factor, where blue boxes and red boxes indicate the level of a given factor that has the greatest effect in a positive direction and in a negative direction, respectively. Note that all metrics listed in Table 4.2 are better if their values are smaller. The same result is illustrated in Figure 4-2 for better understanding.

Table 4.2: Main Effects from Latin Hypercube Sampling with 100 Design Points

Factor / Level	Level Value	ROM Revisit [sec]	GOM Revisit [sec]	Constellation Mass [kg]	Reconfiguration Time [days]
N1	31/2	-667	-7800	-2444	-0.05
N2	15/1	-1658	-479	-246	-3.37
N3	29/2	2739	11797	1005	0.81
N4	14/1	317	-1969	2962	2.06
A1	-40km	-3522	-22931	6775	-6.7
A2	-30km	-3625	-25629	2482	-5.2
A3	-20km	-858	-332	-262	-0.4
A4	-10km	561	6831	-424	10.9
A5	10km	1021	5863	-1462	8.6
A6	20km	565	6457	-1953	-1.5
A7	30km	1080	8794	-3237	-5.5
A8	40km	8243	37467	-4216	-7.0
P1	1 planes	428	-5662	-912	-0.2
P2	2 planes	-489	-7380	479	-0.4
P3	3 planes	1098	7839	216	-1.4
P4	4 planes	-598	6207	162	1.4
S1	2 sats/plane	3956	19599	-4722	3.2
S2	3 sats/plane	-924	-3003	448	-2.7
S3	4 sats/plane	-1423	-6482	1052	-1.6
S4	5 sats/plane	-1584	-10062	2239	0.4
R1	5°	5076	44821	491	2.7
R2	10°	1798	7602	2281	6.2
R3	15°	-734	368	738	0.5
R4	20°	1205	9709	-2154	-2.4
R5	25°	-1122	-14134	1518	-4.0
R6	30°	-1971	-17839	-681	-2.3
R7	35°	-1648	-16690	-972	0.9
R8	40°	-2995	-20366	498	-1.1

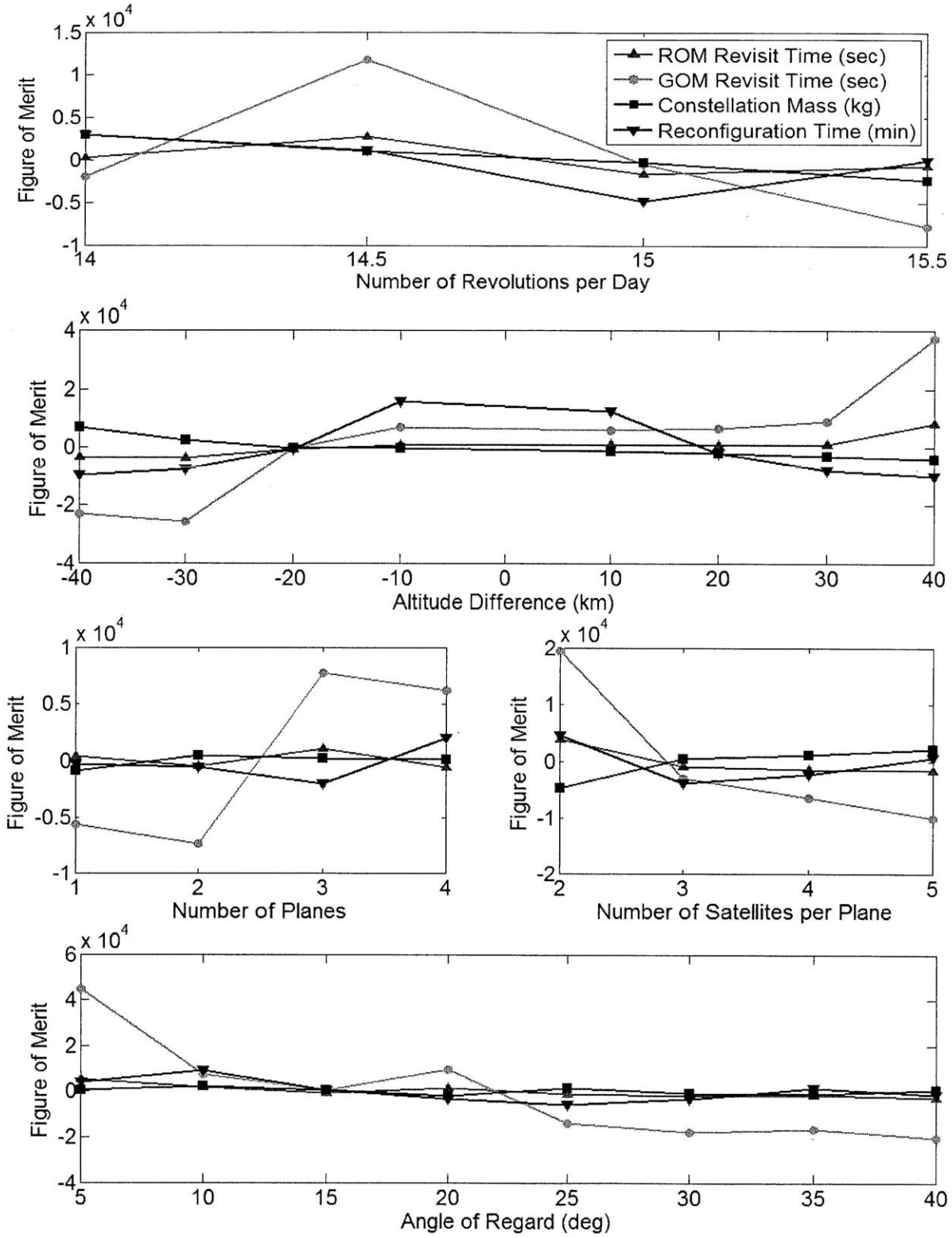

Figure 4-2: Results from Latin Hypercube Sampling

The following trends can be observed from the LHS results:

- As the RGT ratio (N_P/N_D, the number of satellite periods per day) decreases, the mass of the entire constellation increases because more propellant is required (i) to raise the altitude of satellites from the parking orbit to higher altitudes at the beginning of life and (ii) to lower the altitude to the disposal orbit. Reconfiguration time also increases as the RGT ratio increases because there are fewer locations where reconfiguration can occur. Similar increasing trends were observed in ROM revisit time and GOM revisit time, but the positive correlation was not strong.

- High altitude difference increases both ROM revisit time and GOM revisit time because a satellite has to orbit along a longer trajectory with a lower orbit velocity, which leads to a longer orbit period. The constellation mass decreases as altitude difference increases, mainly due to lower atmospheric drag and subsequent reduction in propellant mass. The reconfiguration time decreases as the absolute value of altitude difference increases because a greater deviation from the Walker altitude makes the orbit plane drift faster.

- Both ROM revisit time and GOM revisit time (to a lesser extent) decrease when the number of planes decreases and the number of satellites per plane increases.

- Increasing the FoR decreases the constellation mass.

From these trends, the following recommendations can be made regarding a starting point for optimization algorithms:

- The number of revolutions per day should be large.
- The altitude difference from the Walker constellation should be large.
- The satellites should be distributed in a small number of orbit planes.
- The FoR should be large.

By satisfying these initial conditions, the starting point could be located as close to optima as possible to save computation time and improve the quality of solutions.

4.2 Single-Objective Optimization

The result from the DOE was used as a starting point for the optimization algorithms. Gradient-based methods were deemed inappropriate for the ReCon design optimization problem due to its large design space, nonlinearity, non-convexity (local minima), and combinatorial (discrete) variables. Therefore, heuristics (or metaheuristics) were considered, which refer to a computational method as a rule of thumb that will improve a design vector over the design space to achieve a desired quality [70]. Amongst a wide variety of heuristics depicted in Figure 4-3, simulated annealing (SA) and genetic algorithm (GA) were implemented for the single-objective optimization of a ReCon design. Both SA and GA are nature-inspired algorithms but have distinctive characteristics, as explained in Table 4.3. SA perturbs a design vector according to an explicit cooling schedule whereas GA has a schedule implicit in genome reproduction [71]. Also, SA tends to require relatively less iteration while GA produces a better-optimized solution, which will be discussed in more detail in the following sections.

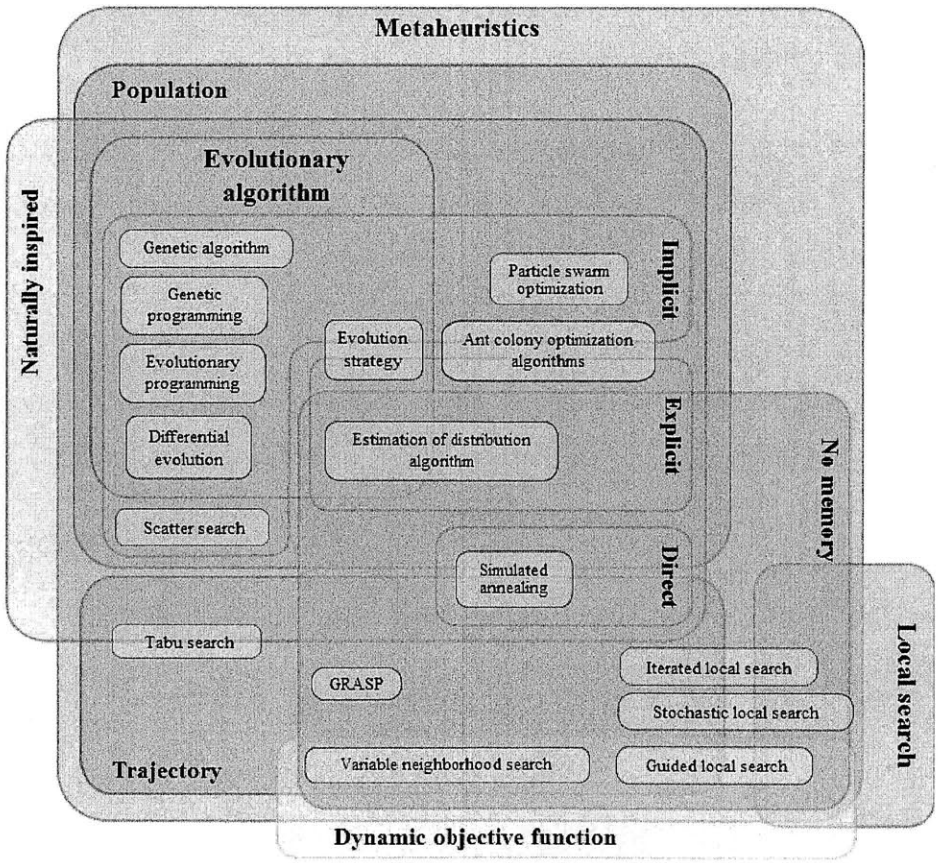

Figure 4-3: Heuristic Methods [70]

Table 4.3: Comparison of Simulated Annealing and Genetic Algorithm

	Simulated Annealing (SA)	Genetic Algorithm (GA)
Entity	Individual design	Population of designs
Memory	No	Yes
Type	Direct	Implicit

4.2.1 Simulated Annealing

Simulated Annealing (SA) is a heuristic [72] named and inspired by annealing in metallurgy, which is a cooling technique to increase the crystal sizes and reduce their defects by letting atoms settle down to a minimum energy state. SA attempts to computationally mimic this physical phenomenon through perturbing the initial (or previous) configuration and accepting the new configuration with a probability dependent upon both energy difference and the system temperature. It is the Metropolis-Hastings algorithm that determines whether or not to accept a new configuration. A lower-energy configuration will always be accepted; on the other hand, a higher-energy configuration will be accepted only if the acceptance probability in Equation (4.1) is greater than a random number between 0 and 1, as illustrated in Figure 4-4 [64].

$$P(j) = \exp(-\Delta E_j / T_j) \tag{4.1}$$

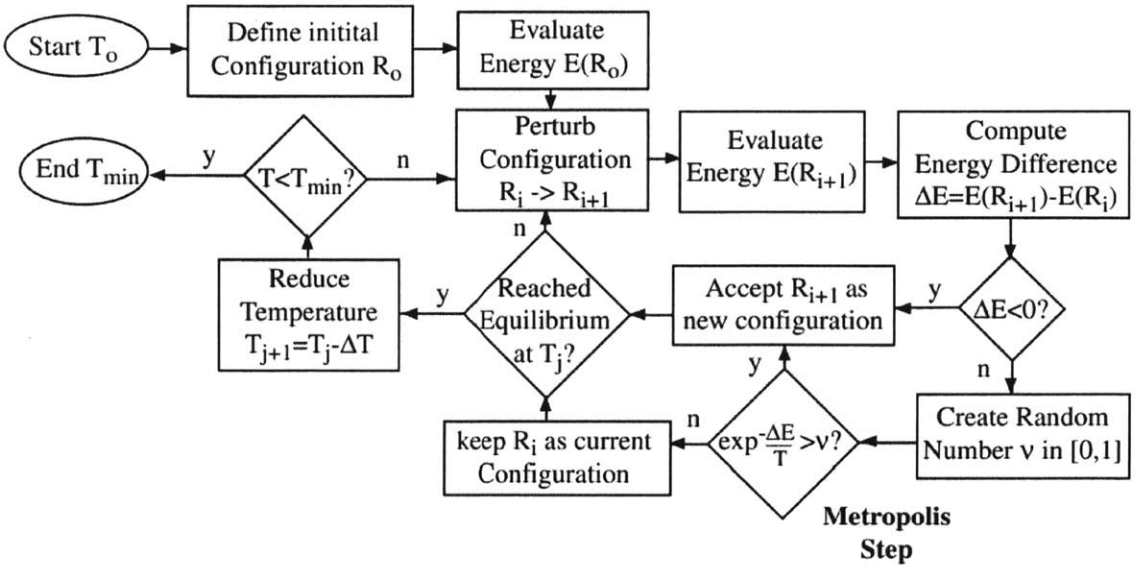

Figure 4-4: Simulated Annealing Flow Diagram [73]

In the equation above, even if the new configuration has higher energy, i.e., positive energy difference ($\Delta E_j > 0$), it is likely to be accepted in earlier stages because the high system temperature (T_j) makes the acceptance probability high. As a cooling schedule decreases the system temperature in a controlled way, however, the acceptance probability also decreases, making the acceptance harder. In a nutshell, SA initially searches a wide design space by allowing configurations that appear inferior at first glance, but it behaves like a steepest-gradient method in the end to narrow down to a local minimum.

The SA optimizer was implemented by modifying the SA codes provided on the MIT Stellar course website, as seen in Figure 4-5 [67, 68]. The evaluation function is the ReCon simulation model discussed in Chapter 3. The perturbation function perturbs all or part of the elements in a design vector: RGT ratio, altitude difference, number of orbit planes, number of satellites per plane, FoR, and propellant type. The propellant type is fixed as monopropellant, so up to five design variables can be perturbed at once. In this implementation, two variables were perturbed at once because experimentation showed that it was optimal.

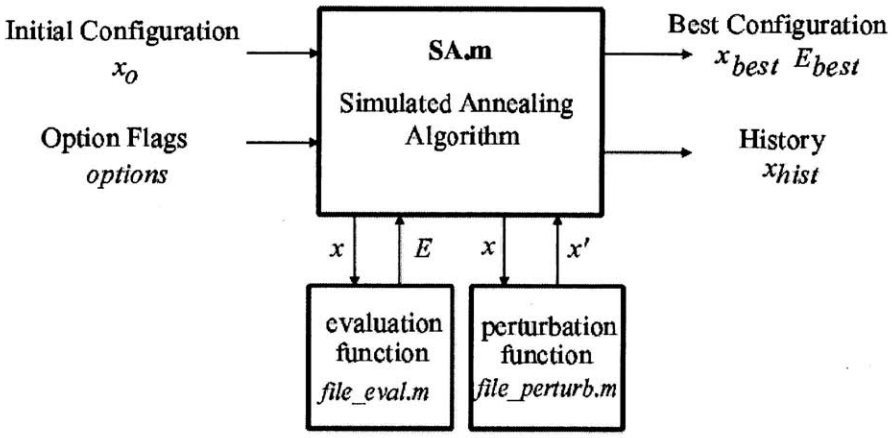

Figure 4-5: Simulated Annealing MATLAB Function Block Diagram [67]

The allowable range of each variable and its initial value are listed in Table 4.4. The initial values were chosen according to recommendations from DOE: the minimum height, the lowest altitude difference, smallest number of planes and satellites, and the greatest FoR. The SA tuning parameters are summarized in Table 4.5 along with their rationales. The cooling schedule is such that the temperature decreases by a factor of ten at each step to expedite the system convergence.

Table 4.4: Design Variable Range and Initial Values in SA

Design Variable (MATLAB Name)	Range	Type	Initial Value
RGT Ratio `nk`	31/2 to 13/1 (Low to high altitude)	Discrete (decrement of 0.5)	31/2
Altitude Difference `delta_alt`	-200km to 200km	Continuous	-200km
Number of Planes `n_planes`	2 to 9	Integer	2
Number of Satellites per Plane, `n_sats`	1 to 5	Integer	1
Field of Regard `Regard`	5° to 50°	Continuous	50°
Propellant Type `prop`	2 (monopropellant)	Integer	2

Table 4.5: SA Tuning Parameters

SA Parameters	Values	Rationale
T_0 - initial system temperature	See Table 4.8	Guarantees a good initial sampling of the design space by satisfying $\exp(-E(x_0)/ T_0) > 0.99$
Cooling Schedule	Exponential	Proven to be effective in terms of the optimality of the final result and computation time
dT -Temperature Cooling Rate	$dT = T_{k+1} / T_k$ =0.1	This value was shown to be effective in terms of the optimality of the final result and computation time
Equilibrium Condition	20 evaluations	Ensures that enough configurations are evaluated before moving to the next temperature state
Freezing Condition	3 evaluations	Ensures that freezing occurs near the optimal solution

The single-objective fitness function was defined as a weighted sum of individual figures of merit and penalty terms of constraint violation:

$$F(\mathbf{x}) = \sum_{i=1}^{4} w_i s_i J_i(\mathbf{x}) + g \sum_{j=1}^{5} c_j h_j(\mathbf{x}) \tag{4.2}$$

where $\mathbf{x}$ is the design vector; J_i's are figures of merit; and h's are constraint violations, which are zero if there is no violation and positive if there is any violation. The figures of merit and the constraints are summarized in Table 4.6. Note that J_1 is defined as the negative of GOM coverage because we seek to maximize coverage and minimize the other FOMs. Also, GOM coverage is used instead of GOM revisit time analyzed in DOEs in order to Both the FOMs and constraint violations are weighted and scaled to transform different physical values into a

single objective. In the first term in Equation (4.2), each FOM is multiplied by the corresponding scaling factor (s_i) and weight (w_i), as shown in Table 4.7. Scaling factors are used to prevent domination of one FOM over others by converting them to approximately the same order of magnitude. Weights balance the relative importance of the four FOMs. To reiterate, we want to minimize the objective (fitness) here.

Table 4.6: Single-objective Fitness Function

FOM	Definition	Constraint	Weighting
J_1	(-1) × GOM coverage (%)	h_1	Minimum altitude
J_2	ROM revisit time (s)	h_2	Maximum altitude
J_3	System mass (kg)	h_4	Maximum aperture
J_4	Reconfiguration time (day)	h_5	Maximum propellant mass fraction

Table 4.7: Fitness Function Objectives

FOM	Typical Value	Scaling Factor (s_i)	Weighting (w_i)
J_1	-5	0.5	0.25
J_2	1000	0.001	0.25
J_3	10000	0.0001	0.3
J_4	2	1	0.2

Table 4.8: Fitness Function Constraints

Constraint	Value	Scaling Factor (c_j)	Gain (g)
Minimum altitude	350km	0.01	Values from 0.001 to 1000 experimented
Maximum altitude	120km	0.001	
Maximum aperture	1.8m	1	
Maximum propellant mass fraction	0.3	100	

The second term in Equation (4.2) is a penalty term imposed on constraint violations. When the amount of violations increases, the penalty also increases. This penalty term is necessary because (1) design solutions with large constraint violations are less favorable or (2) the uncertainty increases outside the range where our assumptions of governing equations are valid. The amount by which each constraint is violated, h_j, is multiplied by a relative scale factor c_j and a global gain g, as summarized in Table 4.8. Because we want to minimize the overall fitness, large constraint violation will result in a higher overall objective (fitness)

which is undesirable, even if the objective part itself might be small. The relative scale factors force the constraints to be of approximately the same order of magnitude. The gain g can be tuned to adjust the optimizer's navigation behavior in the design space, which will be discussed in more depth later.

A sample SA run is illustrated in Figure 4-6 with these simulation settings: on the left side is the convergence history where the optimizer navigates through a large design space in the beginning, and converges to an optimum in the end; on the right side is the plot of SA convergence parameters. At each temperature step, temperature decreases exponentially. The specific heat hints at the nature of the solution, whose peak suggests a change in the nature of the solution configuration, namely a "phase change."

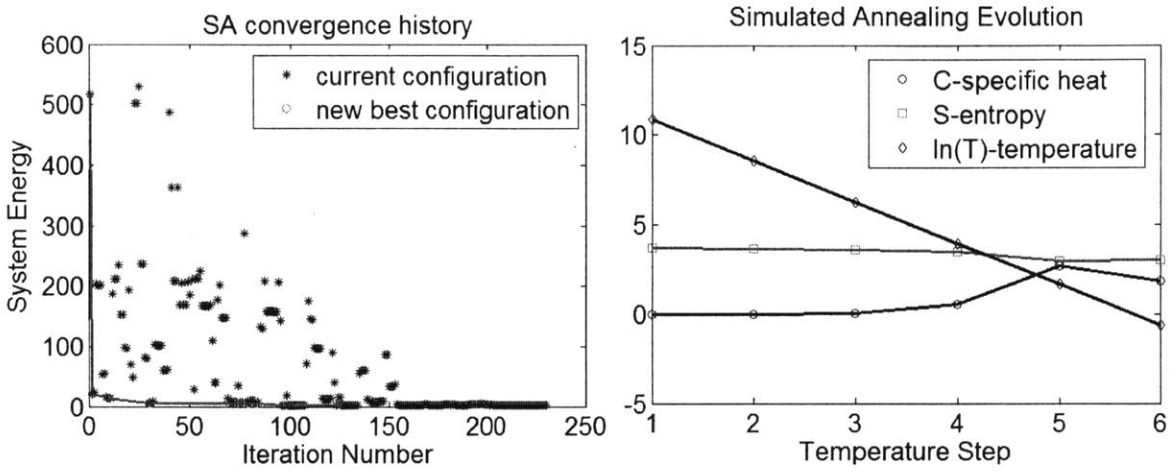

(a) SA Fitness (Energy) Convergence (b) SA Convergence Parameters

Figure 4-6: Simulated Annealing Simulation History (Gain = 10)

More simulations were performed as the global gain g for constraint violations was varied from 0.001 to 1000, as summarized in Table 4.9. When the gain is small, from 0.001 to 0.1, the optimized solution violates constraints because the penalty is discounted; however, when the gain is larger, the optimizer tries to avoid violating the constraints because the incurred penalty will be significantly amplified. It has been found that a high value of gain improves not only the optimality of a solution, as seen by a low normalized fitness in Table 4.9, but also improves the convergence speed, as illustrated in Figure 4-7.

Table 4.9: Tuning of Constraint Gain in Simulated Annealing

Gain	Fitness*	∑ FOM	Gain ×∑ Penalty	∑ Penalty	Normalized Fitness**
0.001	1.24	1.22	0.02	21.33	22.56
0.01	1.59	1.47	0.12	12.42	13.89
0.1	1.53	1.50	0.03	0.36	1.85
1	2.27	2.27	0	0	2.27
10	1.71	1.71	0	0	1.71
100	1.75	1.75	0	0	1.75
1000	1.46	1.46	0	0	1.46

* Fitness or objective = ∑FOM + Gain × ∑ Penalty

** Normalized Fitness = ∑ FOM+ ∑Penalty

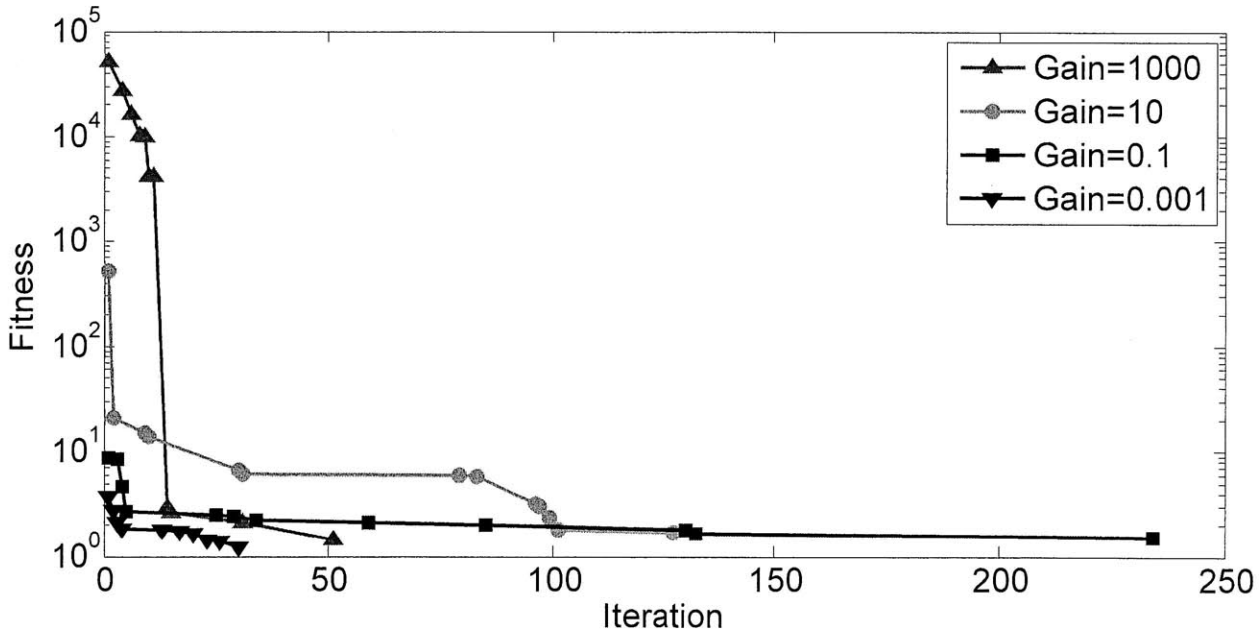

Figure 4-7: Simulated Annealing Fitness History

The table above also shows that the case with the greatest gain (1000) has the most optimal solution with a normalized fitness of 1.46. The ReCon configuration with this fitness value has a 15/1-RGT orbit, an altitude difference of 49.6km, 5 orbit planes, 2 satellites per plane, and a field of regard of 46.8°. All boundary constraints seem to be inactive, but the range of variables will be readjusted in the next chapter to confirm this. The figures of merit are provided in Table 4.6.

Table 4.10: Optimal ReCon Design from SA

Design Variable	Value	Boundary	FOM	Value
RGT Ratio `nk`	2	Inactive	GOM area coverage	2.89%
Altitude Difference `delta_alt`	49.6km	Inactive	ROM revisit time	1609s
Number of Planes `n_planes`	5	Inactive	Constellation mass	26276kg
Number of Satellites per Plane, `n_sats`	2	Inactive	Reconfiguration time	3.17 days
Field of Regard `regard`	46.8°	Inactive		

4.2.2 Genetic Algorithm

In addition to SA, a genetic algorithm (GA) was implemented by modifying the GA code provided on the Stellar course website [74]. GAs mimic the process of natural selection, where individuals are fighting for survival in the population. Only the "fittest" can survive and reproduce, improving the entire population over generations. The optimization routine terminates when the maximum number of generations GAs differ from other traditional optimization methods in that: they search a population of design points, not a single design; and they operate on an encoding of design variables (genotype) instead of variables themselves (phenotype). Figure 4-8 illustrates the GA flow diagram [75] and the state of design variables in each step.

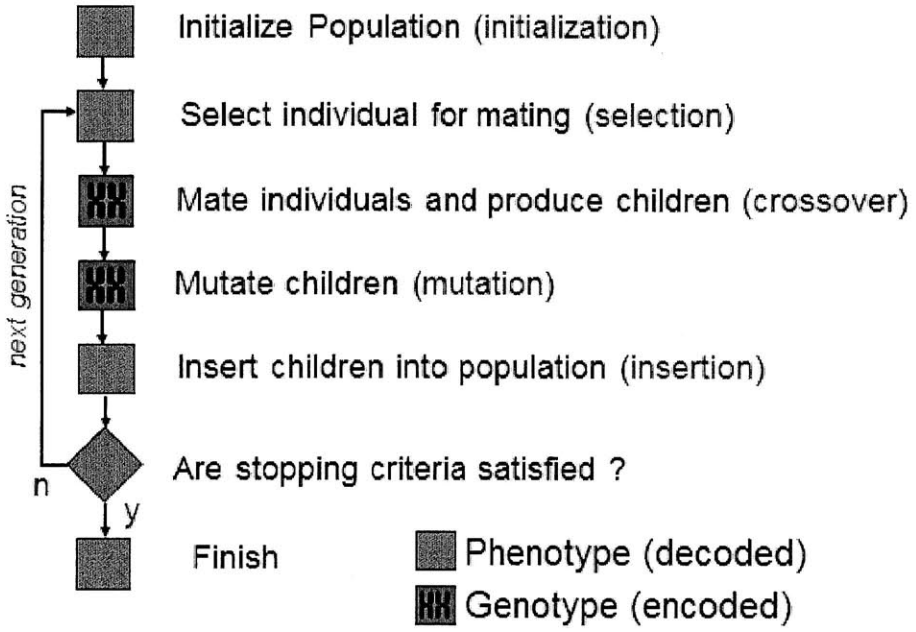

Figure 4-8: Genetic Algorithm Flow Diagram [75]

In this GA implementation, the chromosomes are encoded into binary schemas using two bases of 0 and 1. The design variables are given a varying number of bits corresponding to the range of permissible values as well as whether or not the variables are continuous or discrete, as summarized in Table 4.11. The number of bits chosen for the integer variables ensures that there is no error when encoding and decoding; while this could have potentially been accomplished with fewer bits, 4 bits are chosen so that there would be enough length to effectively accomplish crossover and mutations. Two continuous variables use 12 bits each so that the encoding and decoding error is small. Note that the entire range of variables was adjusted from that used in SA. This is to ensure that GA can quickly find local minima unaffected by active constraints.

The selection process uses a roulette wheel selection scheme. A crossover rate of 0.95 and a mutation rate of 0.001 were used along with a population of 50. Experimentation has shown that higher mutation rates often lead to poor convergence because new, mutated species are continually injected into the population; lower mutation rates with a small population also provide sub-optimal solutions because the population converges homogeneously to a sub-optimal solution too quickly.

Table 4.11: Design Variable Chromosome Parameters

Design Variable	Range	Type	Bits	Max Encode / Decode Error (Absolute)
RGT Ratio `nk`	31/2 to 14/1	Integer	4	N/A
Altitude Difference `delta_alt`	-100 to 100	Continuous	12	0.097
Number of Planes `n_planes`	2 to 7	Integer	4	N/A
Number of Satellites per Plane, `n_sats`	1 to 7	Integer	4	N/A
Field of Regard `Regard`	5 to 60	Continuous	12	0.011
Propellant Type `prop`	2	Integer	4	N/A

Figure 4-9 shows the convergence history of the population mean fitness, and Figure 4-10 illustrates the fitness of the best individual, whose values are summarized in Table 4.12. If the constraint gain is too small (0.001), the constraint violation is discounted and the resultant solution is sub-optimal. If the gain is too high, the solution is also sub-optimal, so the most optimal solution was found when the gain is 0.1. It is also noteworthy that the convergence of the population mean fitness and the best individual was both obtained earlier when the constraint gain was lower.

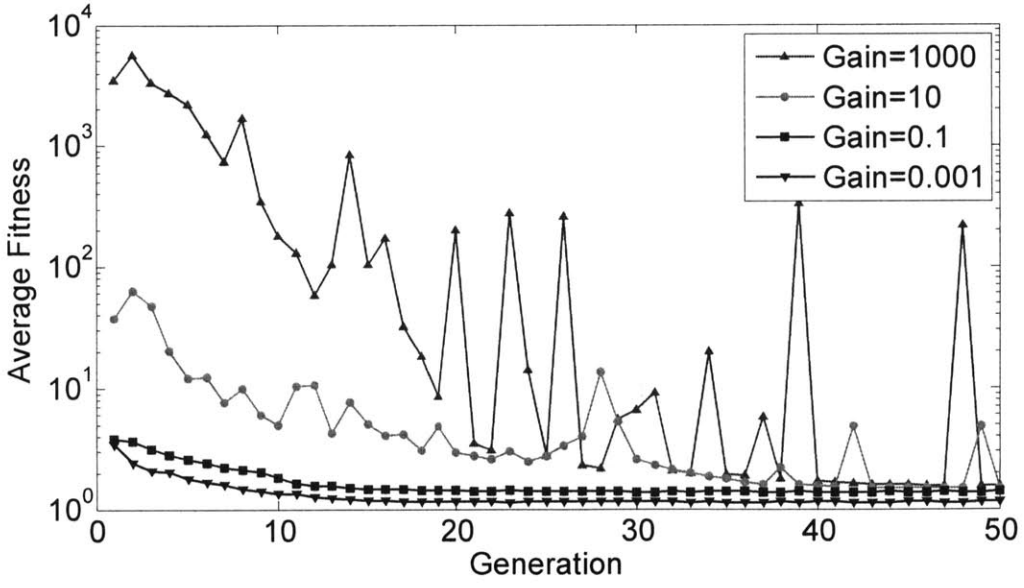

Figure 4-9: Genetic Algorithm Mean Fitness History

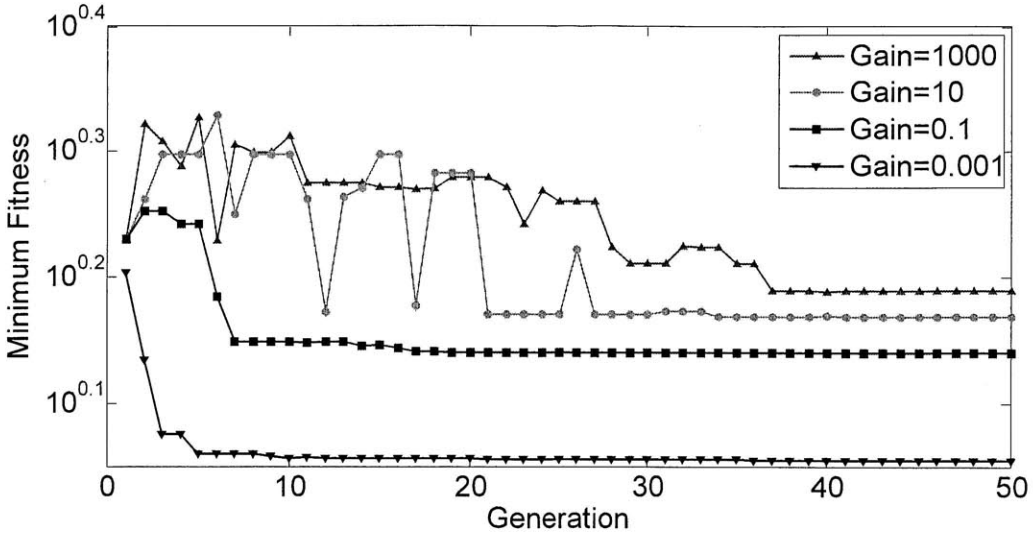

Figure 4-10: Genetic Algorithm Minimum Fitness History

Table 4.12: Tuning of Constraint Gain in Genetic Algorithm

Gain	Fitness*	∑ FOM	Gain ×∑ Penalty	∑ Penalty	Normalized Fitness**
0.001	1.135	1.117	0.018	18.14	19.25
0.1	1.382	1.382	0	0	1.382
10	1.473	1.473	0	0	1.473
1000	1.543	1.543	0	0	1.543

* Fitness or objective = ∑FOM + Gain × ∑ Penalty
** Normalized Fitness = ∑ FOM+ ∑Penalty

Table 4.13 summarizes the optimal ReCon design obtained when the constraint gain was 0.1. This configuration is very similar to the optimal ReCon design obtained from SA, except the sign of altitude difference. GA produced a solution with negative altitude difference, which compromised the GOM coverage performance but also reduced the constellation mass. The ROM revisit time and reconfiguration time remained nearly the same.

Table 4.13: Optimal ReCon Design from GA

Design Variable	Range	Boundary	FOM	Value
RGT Ratio	2	Inactive	GOM area coverage	1.95%
Altitude Difference	-54.7km	Inactive	ROM revisit time	1602s
Number of Planes	5	Inactive	Constellation mass	21318kg
Number of Satellites	2	Inactive	Reconfiguration time	2.93 days
Field of Regard	47.1°	Inactive		

4.2.3 Comparison of SA and GA

Both SA and GA produce very similar ReCon configurations with 5 orbit planes, 2 satellites per plane, and a field of regard of 47°. Only the altitude difference differs in sign, but the magnitudes are very close to each other. The solution from GA is more optimal (less fitness value) than that from SA, but requires significantly more computation time. For a desktop with Intel® Core™ i7-2600 CPU (3.40GHz) and 16.0 GB RAM, it takes around 6 hours to perform one run of GA optimization and 1 hour for SA. GA performs optimization over a population of designs and SA optimizes a single design point, so the former requires more iterations.

4.2.4 Sensitivity Analysis

A sensitivity analysis is conducted at the optimal design1415, $\mathbf{x}^*$ = (15/1, -54.7, 5, 2, 47.1), by approximating the local gradient to the first order and normalizing it:

$$\nabla\bar{F} = \frac{\mathbf{x}^*}{F(\mathbf{x}^*)} \circ \nabla F = \frac{1}{F(\mathbf{x}^*)} \begin{bmatrix} N \\ A \\ P \\ S \\ R \end{bmatrix}^* \circ \begin{bmatrix} \partial F/\partial N \\ \partial F/\partial A \\ \partial F/\partial P \\ \partial F/\partial S \\ \partial F/\partial R \end{bmatrix}^* = \frac{1}{F(\mathbf{x}^*)} \begin{bmatrix} N\partial F/\partial N \\ A\partial F/\partial A \\ P\partial F/\partial P \\ S\partial F/\partial S \\ R\partial F/\partial R \end{bmatrix}^*$$

$$\text{where} \begin{bmatrix} \partial F/\partial N \\ \partial F/\partial A \\ \partial F/\partial P \\ \partial F/\partial S \\ \partial F/\partial R \end{bmatrix}^* \cong \begin{bmatrix} (F(N^* + \Delta N, A^*, P, S^*, R^*) - F(N^*, A^*, P^*, S^*, R^*))/\Delta N \\ (F(N^*, A^* + \Delta A, P^*, S^*, R^*) - F(N^*, A^*, P^*, S^*, R^*))/\Delta A \\ (F(N^*, A^*, P + \Delta P, S^*, R^*) - F(N^*, A^*, P^*, S^*, R^*))/\Delta P \\ (F(N^*, A^*, P^*, S^* + \Delta S, R^*) - F(N^*, A^*, P^*, S^*, R^*))/\Delta S \\ (F(N^*, A^*, P, S^*, R^* + \Delta R) - F(N^*, A^*, P^*, S^*, R^*))/\Delta R \end{bmatrix} \quad (4.3)$$

In the equation above, $\circ$ is the entrywise product, also called the Hadamard product or the Schur product [68]. Table 4.14 summarizes the sensitivity analysis results. It can be found that the RGT ratio has the largest impact (highest sensitivity) while the number of planes shows the second highest sensitivity. Because both variables have positive sensitivity values, increasing these variables will reduce the optimality of a ReCon (remember that high fitness is defined to be undesirable). The RGT ratio determines the RGT altitude, which plays a significant role in sizing both the payload and the propulsion subsystem, driving overall system mass. It makes intuitive sense that the number of satellites in the constellation would

drive the objective function. The sensitivity of the altitude difference was negative at this design point, which means that increasing this variable will improve the optimality.

Table 4.14: Sensitivity Calculation at the Optimal Solution from SOO

Design Variable	Step (Δ)	Optimal Solution ($F(\mathbf{x}^*)$)	Perturbed Solution ($F(\mathbf{x}^* + \Delta)$)	Sensitivity (∇F)	Normalized Sensitivity ($\nabla \bar{F}$)
RGT Ratio (N)	0.5	1.382	2.343	1.922	20.87
Altitude Difference (A)	10km	1.382	1.498	0.012	-0.458
Number of Planes (P)	1	1.382	1.681	0.299	1.083
Number of Satellites (S)	1	1.382	1.428	0.046	0.067
Field of Regard (R)	5°	1.382	1.423	0.008	0.284

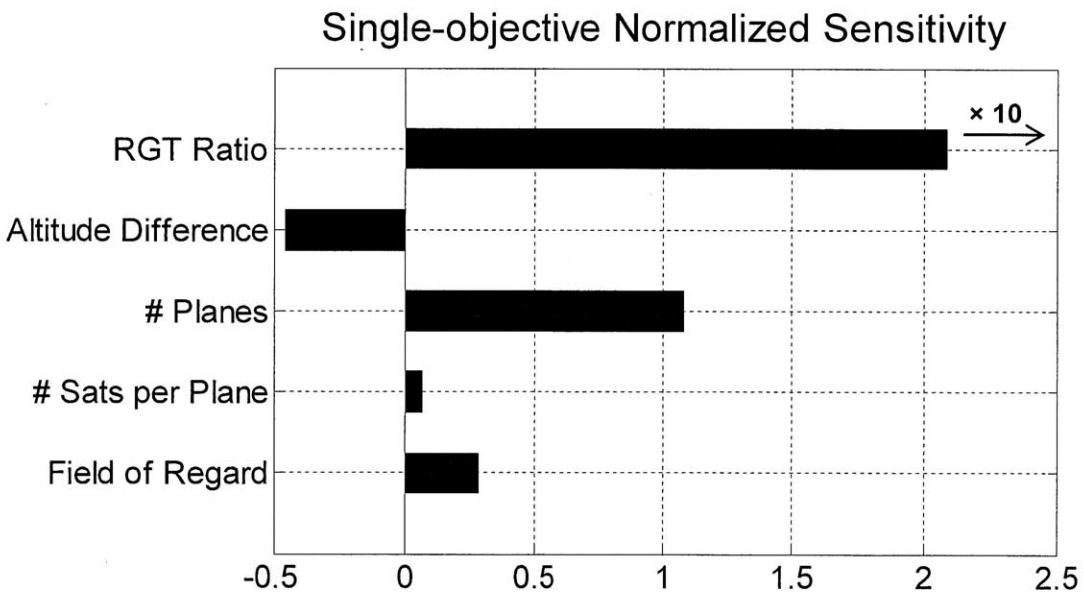

Figure 4-11: Normalized Sensitivity at the Optimal Solution from SOO

4.3 Multi-Objective Optimization

In the previous sections, SA and GA were performed as single-objective optimization (SOO) approaches in order to find a single-point optimal design. The obtained ReCon design was optimal in that it maximizes its performance (or minimizes the fitness function). However, SOO fails to clearly demonstrate the trade-offs, or tensions, amongst figures of merit because all metrics are wrapped into a single value. Therefore, multi-objective optimization (MOO) is required, where the objective is no longer a scalar, but a vector of objectives. The elements of the objective vector are conflicting, but can easily be inspected and balanced on the objective space.

The feasible designs from a domain in design space are correlated to a range in objective space. Although all objective vectors are from feasible designs, of special interest for designers are non-dominated solutions. In a non-dominated solution, one objective cannot be improved unless at least one or more objectives are sacrificed. In Figure 4-12, the goal is to maximize the first objective (F_1) and minimize the second objective (F_2), so the non-dominated solutions are those that do not have any neighbors to their bottom and right (towards the "utopia"). When the adjacent non-dominated points are connected each other, the resulting boundary approximates the true Pareto front. As can be seen in the figure, all Pareto-optimal points are non-dominated, but vice versa is not necessarily true, because of the coarseness of design space.

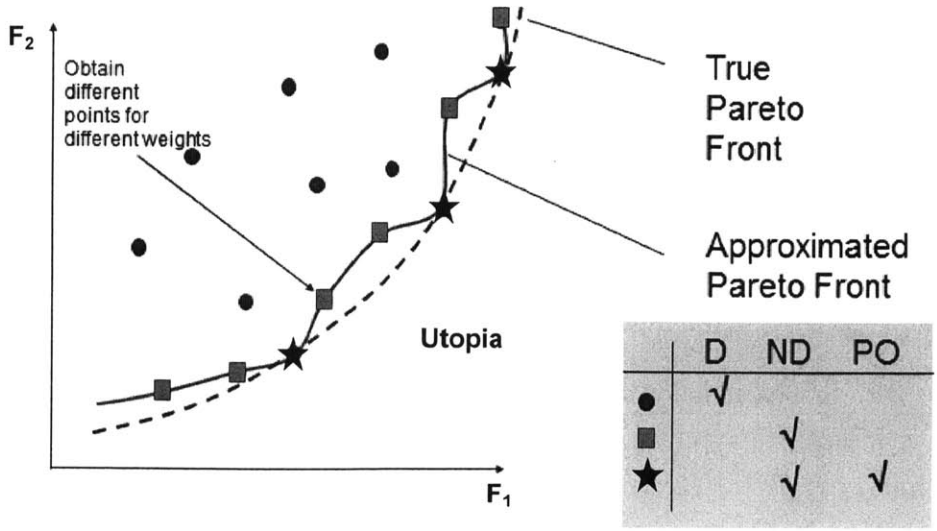

Figure 4-12: Non-dominated (ND) Points and Pareto-Optimal (PO) Points [69]

To sum up, the goal of MOO is to find the Pareto front, whereas SOO tries to find a single optimal solution. Other differences are also summarized in Table 4.15. This section discusses three MOO methods that were implemented: Adaptive Weighted Sum (AWS), Multi-objective Genetic Algorithm (MOGA), and Non-dominated Sorting Genetic Algorithm-II (NSGA-II).

Table 4.15: Comparison of SOO and MOO

	Single Objective Optimization	Multi-Objective Optimization
Objective	Scalar	Vector
Approach	Scalarization	Pareto Front
Designer Preferences	Included a priori in form of weightings	Included a posteriori when investigating a family of solutions in Pareto-optimal set

4.3.1 Multi-objective Definition

In order to turn the SOO problem into the MOO problem, some changes had to be made in defining the objectives. Amongst the four FOMs (GOM coverage, ROM revisit time, reconfiguration time, and constellation mass), reconfiguration time was redefined as a constraint, whose allowable maximum was set to be 4 days. This value was set from experimentation in order to allow a design space that is large enough. GOM coverage and ROM revisit time were scaled and summed up as one objective (F_1), whereas the mass of the entire constellation mass (proxy of cost) was set as another objective (F_2), resulting in a bi-objective problem. The FOMs and constraints are explained in Table 4.16, and the two objectives are defined in Equation (4.4).

Table 4.16: Multi-objective Fitness Function

FOM	Explanation	Constraint	Weighting
J_1	(-1) × (GOM coverage)	h_1	Minimum altitude
J_2	ROM revisit time	h_2	Maximum altitude
J_3	Constellation mass	h_3	Maximum aperture
		h_4	Maximum propellant mass fraction
		h_5	Maximum reconfiguration time

$$F_1(\mathbf{x}) = w_1 s_1 J_1(\mathbf{x}) + w_2 s_2 J_2(\mathbf{x}) + g \sum_{j=1}^{5} c_j h_j(\mathbf{x})$$
$$F_2(\mathbf{x}) = w_3 s_3 J_3(\mathbf{x}) + g \sum_{j=1}^{5} c_j h_j(\mathbf{x}) \quad (4.4)$$

In calculating the values of two fitness functions, FOMs are penalized by the amount of constraint violations as in Equation (4.4). The corresponding scaling factors and weights are summarized in Table 4.17.

Table 4.17: Scaling and Weighting of FOMs

FOM	Typical Value	Scaling Factor (s_i)	Weighting (w_i)
GOM area coverage (%)	5	0.5	0.5
ROM revisit time (s)	1000	0.001	0.5
Constellation mass (kg)	10000	0.0001	1

4.3.2 Adaptive Weighted Sum

Adaptive weighted sum (AWS) is a variation of a weighted sum approach. The weighted sum turns the objective vector into a scalar by multiplying weights whose sum is unity with each element of the vector. By varying the weights and optimizing with these weights, solutions on the Pareto front can be obtained. However, this approach has two major drawbacks:

- Evenly spaced weights among the objectives do not necessarily result in evenly distributed solutions on the Pareto front. That is, solutions can be heavily concentrated in some parts of the Pareto front while leaving gaps in other parts.

- The non-dominated solutions located on the non-convex parts of the Pareto front cannot be located, because the weighted sum is often implemented as a convex combination of objectives. Here, a convex combination refers to a linear combination of points or vectors where all coefficients are non-negative and add up to 1, which is often the case in real applications [76].

$$F_1(\mathbf{x}) = w_1 s_1 J_1(\mathbf{x}) + w_2 s_2 J_2(\mathbf{x}) + g \sum_{j=1}^{5} c_j h_j(\mathbf{x})$$
$$F_2(\mathbf{x}) = w_3 s_3 J_3(\mathbf{x}) + g \sum_{j=1}^{5} c_j h_j(\mathbf{x}) \quad (4.4)$$

In calculating the values of two fitness functions, FOMs are penalized by the amount of constraint violations as in Equation (4.4). The corresponding scaling factors and weights are summarized in Table 4.17.

Table 4.17: Scaling and Weighting of FOMs

FOM	Typical Value	Scaling Factor (s_i)	Weighting (w_i)
GOM area coverage (%)	5	0.5	0.5
ROM revisit time (s)	1000	0.001	0.5
Constellation mass (kg)	10000	0.0001	1

4.3.2 Adaptive Weighted Sum

Adaptive weighted sum (AWS) is a variation of a weighted sum approach. The weighted sum turns the objective vector into a scalar by multiplying weights whose sum is unity with each element of the vector. By varying the weights and optimizing with these weights, solutions on the Pareto front can be obtained. However, this approach has two major drawbacks:

- Evenly spaced weights among the objectives do not necessarily result in evenly distributed solutions on the Pareto front. That is, solutions can be heavily concentrated in some parts of the Pareto front while leaving gaps in other parts.

- The non-dominated solutions located on the non-convex parts of the Pareto front cannot be located, because the weighted sum is often implemented as a convex combination of objectives. Here, a convex combination refers to a linear combination of points or vectors where all coefficients are non-negative and add up to 1, which is often the case in real applications [76].

Therefore, AWS is used to further refine the Pareto front obtained from the weighted sum. The procedures for performing AWS when the goal is to minimize two objectives, F_1 and F_2, simultaneously, are provided below.

- Step 1: Normalize the objective functions in the objective space.

$$\bar{F}_i = \frac{F_i - F_i^U}{F_i^N - F_i^U}$$

where $\mathbf{x}^{1*}, \mathbf{x}^{2*}$ are optimal solution vectors from single-objective optimization

$$F^U = [F_1^U, F_2^U]\text{: Utopian point, } F_i^U = \min\{F_i(\mathbf{x}^{1*}), F_i(\mathbf{x}^{2*})\}$$
$$F^N = [F_1^N, F_2^N]\text{: Non-utopian point, } F_i^N = \max\{F_i(\mathbf{x}^{1*}), F_i(\mathbf{x}^{2*})\} \quad (4.5)$$

- Step 2: Perform MOO using the usual weighted sum approach. The uniform step size can be obtained by dividing unity by the number of desired steps, $n_{initial}$. The recommended value is between 3 and 10, so 5 is used here.

$$\min \alpha_i \bar{F}_1(\mathbf{x}) + (1 - \alpha_i)\bar{F}_2(\mathbf{x})$$
$$\alpha_i \in [0, 1], \Delta\alpha = 1/n_{initial} \quad (4.6)$$

- Step 3: Delete adjacent solutions that almost overlap each other on the Pareto front.

- Step 4: Determine the number of refinements in each of the regions. More refinements are required for the segment whose length is relatively long compared to the average length of overall segments. In Equation (4.7), the range of C is [1, 2], in which a large value of C is used if a small $n_{initial}$, was used, to limit premature convergence.

-

$$n_i = Round(C\frac{l_i}{l_{avg}}) \quad (4.7)$$

- Step 5: If $n_i \leq 1$, no further refinement is needed in that segment. If $n_i > 1$, determine the offset distances from the two end points of each segment.

❖ Step 5-1: Find the slope angle of the piecewise linearized secant line connecting the two end points.

$$\theta = \tan^{-1}\left(-\frac{P_1^2 - P_1^2}{P_1^1 - P_1^1}\right) \tag{4.8}$$

❖ Step 5-2: Select a distance along the secant line, δ_J, and perform a sub-optimization internally with the weighted sum method in each of the feasible regions. The range of δ_J is [0.05, 0.2] in the normalized objective space, and α_i is the relative weighting between objectives (δ_J =0.1 and $\alpha_1 = 0.67$ used here).

$$\begin{aligned} &\min \alpha_i \bar{F}_1(\mathbf{x}) + (1-\alpha_i)\bar{F}_2(\mathbf{x}) \\ &\text{s.t. } \bar{F}_1(\mathbf{x}) \le P_1^x - \delta_1 = P_1^x - \delta_J cos\theta \\ &\bar{F}_2(\mathbf{x}) \le P_1^y - \delta_2 = P_2^y - \delta_J sin\theta \\ &h(\mathbf{x}) = 0 \\ &g(\mathbf{x}) \le 0 \\ &\alpha_i \in [0,1], \Delta\alpha_i = 1/n_i \end{aligned} \tag{4.9}$$

- Step 6: Compute the length of all segments between adjacent solutions. If all the lengths are less than the tolerance, terminate the routine; otherwise, go to Step 4.

Figure 4-13 gives a pictorial summary of the aforementioned steps. The true Pareto front is approximated by a piecewise linear segment, and the feasible region is defined by setting constraints (blue lines) after advancing by δ_J along the segment from the two ends. Under these constraints, new solutions can be found.

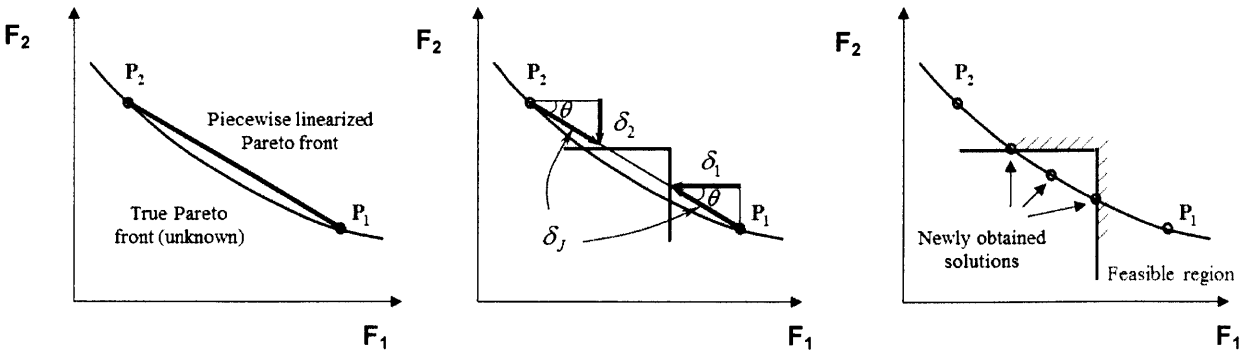

Figure 4-13: Adaptive Weighted Sum (AWS) Approach

To locate the Pareto front, "internal" optimization should be executed once for each point. As the optimization method, GA was used because it has been shown to generate more optimal solutions than SA. The GA routine used a population size of 50 and a mutation rate of 0.0001, which are identical to the values used in SOO.

Because of high computation time, this AWS method could not be automated entirely. The computation time ranged from 3 hours to more than a day, depending upon the constellation size which tends to grow from the bottom and right to top and left. The interface between MATLAB and STK often lost connections when the simulation lasted more than a day. Therefore, the procedures were done in hands. For the same reasons, Step 3 and Step 4 were skipped in this "manual" version. The number of generations was adjusted from 15 to 60. A higher number of generations was used in the lower mass region to place the solution as close to the true Pareto front as possible, and a lower number was used in the higher mass region to reduce computation time. The Pareto front obtained from AWS is plotted in Figure 4-14, where the black dots and the red dots are from the weighted sum and the adaptive weighted sum, respectively. To reiterate, F_1 and F_2 are the constellation performance and the constellation mass, respectively, and both should be minimized here by definition.

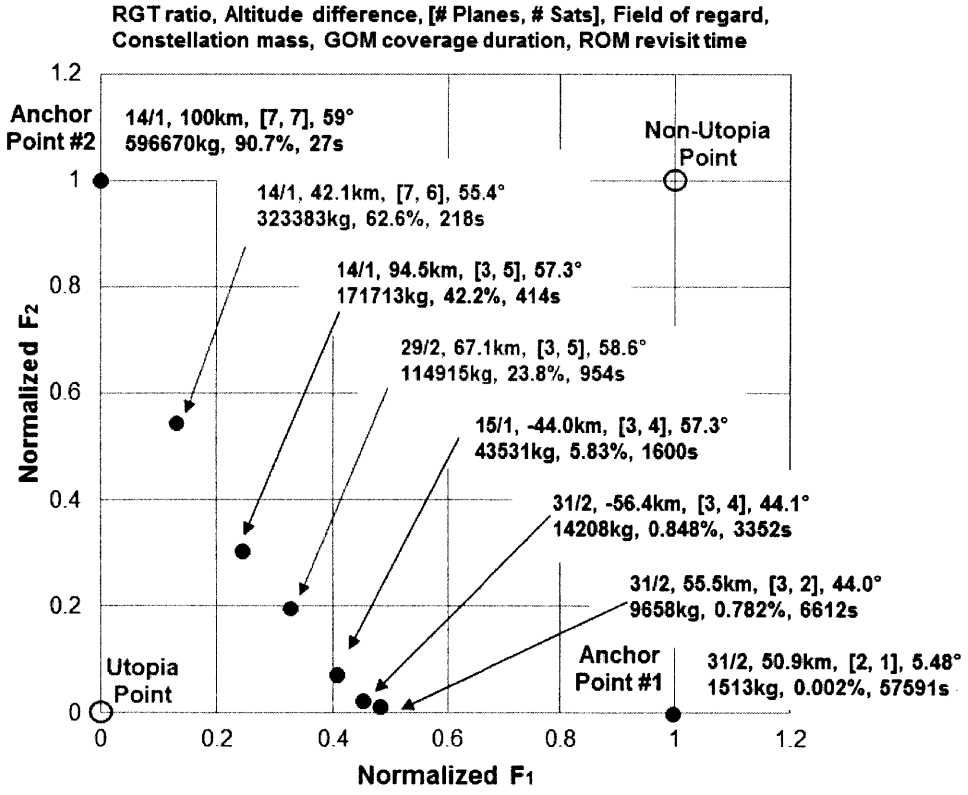

Figure 4-14: Adaptive Weighted Sum (AWS) Results

4.3.3 Multi-objective Genetic Algorithm

To double-check the AWS results and investigate the effect of tuning the constraint gain, g, we also implemented a multi-objective genetic algorithm (MOGA). Compared to the single-objective GA, MOGA uses a Pareto ranking scheme in order to assign the ordinal rankings of a population when multiple objectives must be considered. If an individual x_i in generation t is dominated by $p_t^{(i)}$ individuals, the individual's rank is given by [77]:

$$rank(x_i, t) = 1 + p_t^{(i)} \tag{4.10}$$

In Figure 4-15, for example, the goal is to minimize both f_1 and f_2, so $p_t^{(i)}$ equals the number of individuals which is in the bottom-left quadrant centered at x_i. Non-dominated individuals have a rank of 1.

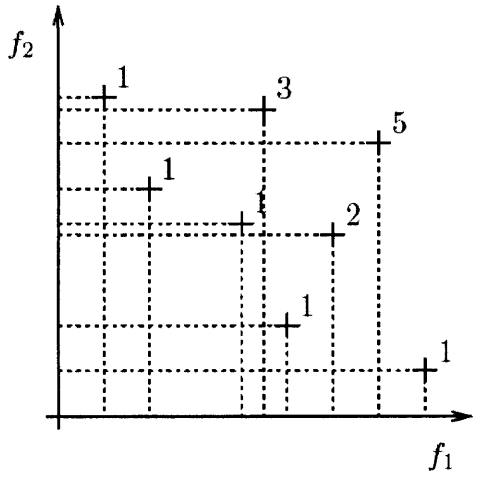

Figure 4-15: Multi-objective Ranking [77]

The individuals are grouped into fronts according to their ranks, and low-ranked fronts have priority in being preserved by elitism. The elitism is an additional selection/filtering step whereby only the top portion (5% used here) of "best-fit" designs are preserved without being affected by crossovers or mutations. By updating this elite group in every generation, the overall population gradually converges to the Pareto front, which is by definition the "most fit" set.

The chosen implementation of MOGA does not include "diversity preserving" schemes, so the population tends to converge or "cluster" around a certain region of the Pareto front due to the convergence of genomes as the GA iterates. To counteract this trend, we increased the population size to 100 (50 in SOO), increased the mutation rate to 0.1 (0.001 in SOO), and decreased the number of generations to 10 (50 in SOO). By increasing the "randomness" via high population size and high mutation rate and terminating the optimization prematurely, the diversity could be maintained.

Figure 4-16 shows the Pareto fronts obtained by varying the constraint gain. When the gain increases, the solutions get better-fitted as they head toward the bottom left direction, but the diversity also decreases due to clustering effects. Another drawback of MOGA is that it can miss portions of the Pareto front even with a well-distributed initial population. In the three cases plotted above, on average only 23 out of 100 individuals were located on the Pareto front, making the front look quite sparse.

W

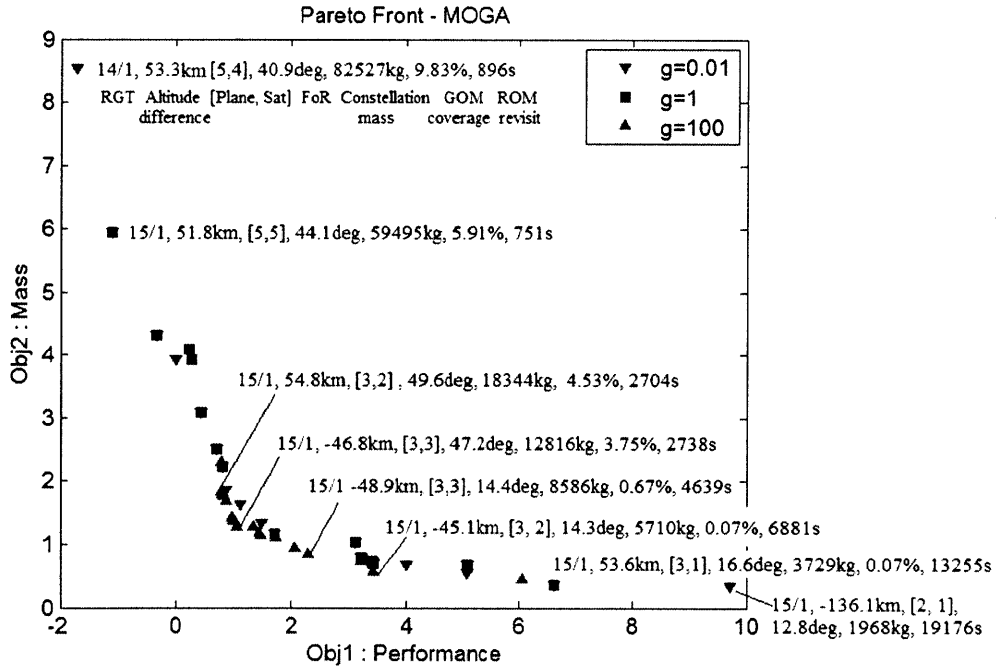

Figure 4-16: Pareto Fronts Obtained via MOGA
with Constraint Violation Gains Ranging from 0.01 to 100.

4.3.4 Non-dominated Sorting Genetic Algorithm-II

The Non-dominated Sorting Genetic Algorithm-II (NSGA-II) is a non-domination-based multi-objective genetic algorithm which improves on its predecessor (NGSA) by removing a priori knowledge requirements and incorporating elitism [78]. The rank of each individual is calculated as in MOGA, but a new parameter called *crowding distance* is also calculated in addition to fitness value for each individual. The crowding distance measures how close an individual is to its closest neighbor. This selection process filters the population based on the rank and the crowding distance; an individual is selected when its rank is lower than others or its crowding distance is greater than others if the ranks are the same. A high crowding distance is preferred in order to spread out solutions along the Pareto front, thus preserving diversity. A brief description of NSGA-II is given below:

- Step 1: Initialize the GA population of size N.

- Step 2: Sort the initialized population based on the non-domination of objectives and assign a crowding distance to each individual of the entire population.

- Step 3: Carry out a binary tournament selection with a crowded-comparison-operator to select better-fitted individuals to have their children. As mentioned earlier, two individuals' ranks are compared first, and when the ranks are the same, their crowding distances are compared.

- Step 4: Perform genetic operations including Simulated Binary Crossover (SBX) and polynomial mutation, which mimic genetic crossovers and mutations in nature (discrete) by generating random numbers (continuous) with appropriate distributions. After the genetic operations, the offspring population of size N is created. More specific details regarding SBX and polynomial mutation are provided in Appendix C.

- Step 5: The offspring (children) population is combined with the current population (parents), making the population size twice the original or $2N$. This mixed population of parents and children is sorted into fronts with differing ranks.

- Step 6: Low-ranked fronts are assigned to the new parent generation. If all the individuals of the last non-dominated front cannot be included without exceeding the population size, N, then the most-widely spread solutions are included.

- Step 7: Repeat from Step 2 to Step 6 until the Pareto front converges.

Figure 4-17 shows the Pareto front obtained from NSGA-II along with the design points obtained from the adaptive weighted sum (AWS) and single-objective optimization (SOO). The designs at anchor points are summarized in Table 4.18. NSGA-II exhibits a clustering phenomenon when the constraint gain is relatedly high (g=1 or g=100 compared to g=0.01), but the solutions at higher gains were not necessarily more optimal on the entire Pareto front.

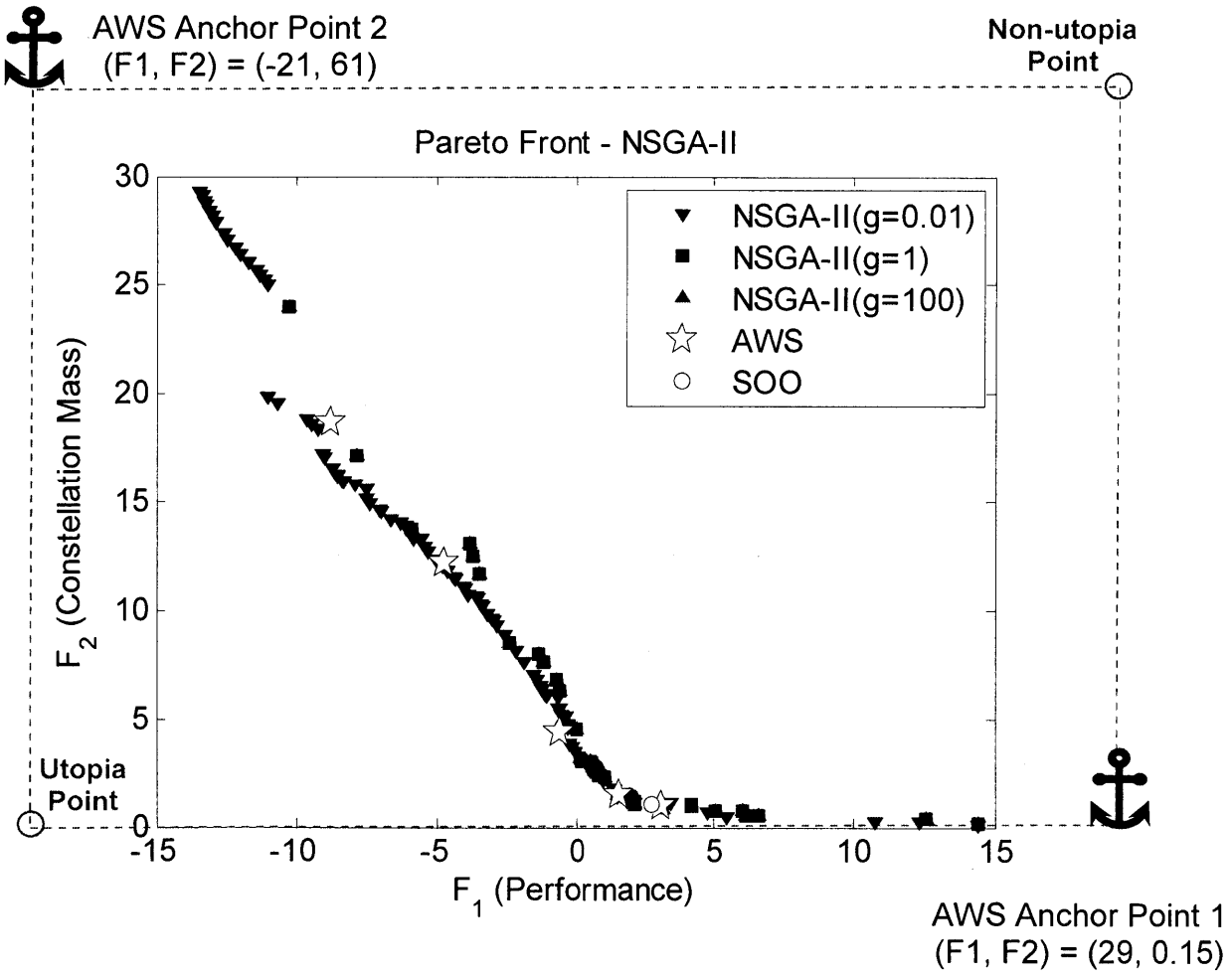

Figure 4-17: Pareto Fronts Obtained via NSGA-II
with Constraint Violation Gains Ranging from 0.01 to 100.

Table 4.18: ReCon Configuration at Anchor Points

Anchor point	#1	#2
RGT ratio	31/2 (↑*)	14/1 (↓**)
Altitude difference	50km	200km (↑)
Number of orbit planes	2 (↓)	7 (↑)
Number of sats per plane	1 (↓)	7 (↑)
Field of regard (°)	5.3	59 (↑)
Fitness 1	28.80	-21.05
Fitness 2	0.1513	61.28

*Upper boundary reached
**Lower boundary reached

It is noteworthy that the solutions obtained via NSGA-II are nearly as optimal as those from the AWS method. AWS generates solutions that are more optimal than those from NSGA-II only when the number of generations is large, which requires a great deal of computation time. Nonetheless, adaptability of AWS to adjust the point locations at a designer's will is still a strong advantage compared to multi-objective heuristics.

Figure 4-18 compares the Pareto fronts obtained by MOGA and NSGA-II. The biggest difference between the two methods is diversity of the solutions. NSGA-II usually places the entire population along the Pareto front, so it produces a Pareto front that is more dense and continuous than that obtained by MOGA.

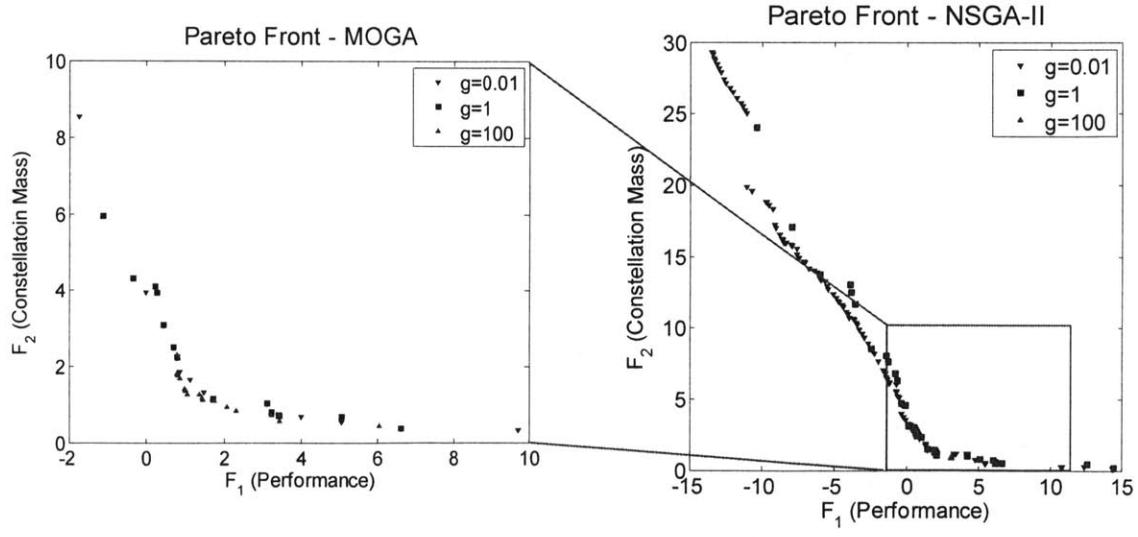

(a) Multi-objective genetic algorithm (b) Non-dominated sorting genetic algorithm-II

Figure 4-18: Pareto Front Calculated via Multi-objective Heuristics

4.4 Sensitivity Analysis

A sensitivity analysis for MOO can be conducted similarly to that for SOO except that the objective gradient is now replaced by the Jacobian matrix, as given in Equation (4.11). The optimal design corresponding to a point on the Pareto front from AWS (α=0.4) was chosen because it was a "knee" point where the cost per marginal performance starts to increase.

$$\nabla\bar{F} = \frac{[\mathbf{x}^* \; \mathbf{x}^*]}{F(\mathbf{x}^*)} \circ \nabla F = \frac{1}{F(\mathbf{x}^*)} \begin{bmatrix} N & N \\ A & A \\ P & P \\ S & S \\ R & R \end{bmatrix}^* \circ \begin{bmatrix} \partial F_1/\partial N & \partial F_2/\partial N \\ \partial F_1/\partial A & \partial F_2/\partial A \\ \partial F_1/\partial P & \partial F_2/\partial P \\ \partial F_1/\partial S & \partial F_2/\partial S \\ \partial F_1/\partial R & \partial F_2/\partial R \end{bmatrix}^* = \frac{1}{F(\mathbf{x}^*)} \begin{bmatrix} N\partial F_1/\partial N & N\partial F_2/\partial N \\ A\partial F_1/\partial A & A\partial F_2/\partial A \\ P\partial F_1/\partial P & P\partial F_2/\partial P \\ S\partial F_1/\partial S & S\partial F_2/\partial S \\ R\partial F_1/\partial R & R\partial F_2/\partial R \end{bmatrix}^* \tag{4.11}$$

As can be seen in the results in Table 4.19 and Figure 4-19, the RGT ratio has the greatest effect on both the performance and mass of a ReCon. However, as for the secondary factors, the constellation mass depends on the number of planes and the number of satellites per plane (the product of the two is the total number of satellites), whereas the performance was affected more by the altitude difference.

Table 4.19: Sensitivity Calculation at the Optimal Solution from MOO

Design Variable	**Step (Δ)**	**Optimal Solution ($F_1(\mathbf{x}^*)$)**	**Perturbed Solution ($F_1(\mathbf{x}^* + \Delta)$)**	**Sensitivity (∇F_1)**	**Normalized Sensitivity ($\nabla \bar{F}_1$)**
RGT Ratio (N)	0.5	1.382	0.393	1.979	22.19
Altitude Difference (A)	10km	1.382	0.339	-0.104	-1.170
Number of Planes (P)	1	1.382	0.979	-0.403	-4.522
Number of Satellites (S)	1	1.382	2.062	0.680	7.630
Field of Regard (R)	5°	1.382	1.023	-0.072	-0.806
Design Variable	**Step (Δ)**	**Optimal Solution ($F_2(\mathbf{x}^*)$)**	**Perturbed Solution ($F_2(\mathbf{x}^* + \Delta)$)**	**Sensitivity (∇F_2)**	**Normalized Sensitivity ($\nabla \bar{F}_2$)**
RGT Ratio (N)	0.5	1.382	2.296	-1.526	-15.43
Altitude Difference (A)	10km	1.382	2.258	-1.450	-14.66
Number of Planes (P)	1	1.382	2.131	-1.196	-12.10
Number of Satellites (S)	1	1.382	1.888	-0.710	-7.184
Field of Regard (R)	5°	1.382	1.829	-0.592	-5.986

3 have similar aperture diameters, so identical payloads can be used in both configurations. Likewise, any staging path can be found based on the commonalities of the satellite designs while keeping the path itself as close to the Pareto front as possible.

Table 4.20: Selected ReCon Configurations along the Pareto Front

Configuration #	**1**	**2**	**3**	**4**	**5**
RGT ratio (altitude)	31/2 (353km)	31/2 (353km)	31/2 (353km)	15/1 (505km)	29/2 (667km)
Altitude difference	+50.9km	+55.5km	-56.4km	-44km	+67.1km
# Orbit planes	2	3	3	3	3
# Sats per plane	1	2	4	4	5
Field of regard	5.48°	44.0°	44.1°	57.3°	58.6°
GOM coverage	0.002%	0.782%	0.848%	5.83%	23.8%
ROM revisit time	57591s	6612s	3352s	1600s	954s
Constellation mass	1513kg	9658kg	14208kg	43531kg	114915kg
Walker altitude	404km	409km	297km	461km	734km
Aperture diameter	0.686m	0.964m	0.703m	3.85m	3.30m
Satellite mass	757kg	1610kg	1184kg	3268kg	7661kg

Chapter 5

ReCon Case Studies

In this chapter, three ReCon applications are studied based on the modeling framework and optimization techniques discussed in the previous chapters.

First, one of the optimal ReCon designs obtained earlier is revisited - one whose orbit planes are rearranged differently from the normal Walker pattern in order to shorten the reconfiguration time. The trade-off is analyzed to see whether this plane rearrangement compromises other performances such as coverage duration and revisit time.

In the following section, Sun-synchronous orbits are considered, which entirely alter the ReCon design space. This is a more realistic scenario because all Earth observation constellations deployed so far have Sun-synchronous orbits to provide consistent illumination conditions.

Finally, this chapter concludes with a small satellite implementation that can be launched as secondary payloads to reduce manufacturing and launch costs.

Although the scope of these applications is restricted to single-objective optimization, this analysis can be easily extended to multi-objective optimization.

5.1 Tailoring Reconfiguration Time

A normal Walker pattern distributes its orbit planes over a longitude range of 360°, with an angular distance between neighboring planes (node interval, $\Delta RAAN$) equal to 360° divided by the number of planes. The normal Walker pattern provides an even global coverage for static constellations, but it may not provide the maximal responsiveness for ReCons because the arrangement of orbit planes does not always minimize the reconfiguration time.

Therefore, this section attempts to tailor the reconfiguration time of a ReCon by changing the normal Walker pattern.

Let us consider a sample ReCon design whose ROM has an RGT orbit such that satellites orbit the Earth 15 times a day (RGT ratio of 15/1). The equator crossings of RGT are 24° (=360°÷15) apart from each other, as represented by red axes in Figure 5-1. Suppose that this ReCon has 6 orbit planes, and a normal Walker pattern will distribute them along the longitude range of 360°with a node interval ($\Delta RAAN$) of 60° (=360°÷6). The orbit planes and equator crossings are represented with blue lines and blue circles, respectively, in Figure 5-1. Initially, satellites are in GOM and their orbit planes (blue lines) are drifting to the direction dependent on the sign of altitude difference; if the altitude difference is greater than zero, the GOM ground tracks will drift westward. The satellites can reconfigure to ROM when the equator crossings of GOM orbits (non-repeating ground track) and ROM orbits (repeating ground track) are coincident, which happens at longitudes of 0°, 120°, and 240°.

As a worst case, suppose that the satellites have just flown over the reconfiguration points so that they have to wait for the next alignment of GOM and ROM equator crossings. When $\Delta RAAN$ is 60°, the minimum traverse angle is 12° in Figure 5-1(a). If the plane interval changes to 68°, however, the minimum traverse angle ($\Delta\varphi_{min}$) will be reduced to 4°. Therefore, the best-positioned satellite ($\Delta\varphi_{min}$=4°) in the modified Walker pattern can access the target faster than one ($\Delta\varphi_{min}$=12°) in the normal Walker pattern.

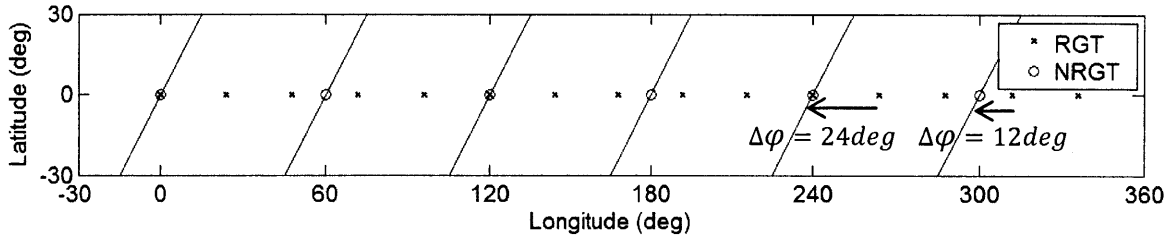

(a) $\Delta RAAN$=60° (Normal Walker)

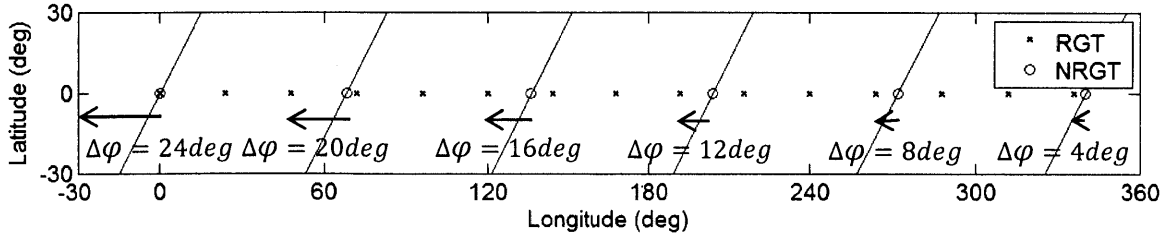

(b) $\Delta RAAN$=68° (Modified Walker)

Figure 5-1: Alignment of GOM and ROM Ground Tracks for Reconfiguration.

Of course, there comes a price to pay. Even though this is not the case here, the worst-conditioned satellite in a modified normal Walker pattern may access the target later than its counterpart in the normal Walker pattern for other combinations of the RGT ratio and the number of planes. Also, the distribution of orbit planes is skewed in the modified pattern, which could impact the GOM coverage for some regions.

Figure 5-2 illustrates the relationship between $\Delta RAAN$ and the geo-spatially averaged traverse angle of a ReCon with 6 orbit planes and an RGT ratio of 15/1. It can be observed that the traverse angle of the best-positioned satellite is minimized when $\Delta RAAN$=68°. On the other hand, the traverse angle of the worst-positioned satellite has a local minimum at $\Delta RAAN$=60°, which is identical to the normal Walker pattern. It is clear in the plot that the traverse angles of the best-conditioned satellite and the worst-conditioned satellite behave oppositely.

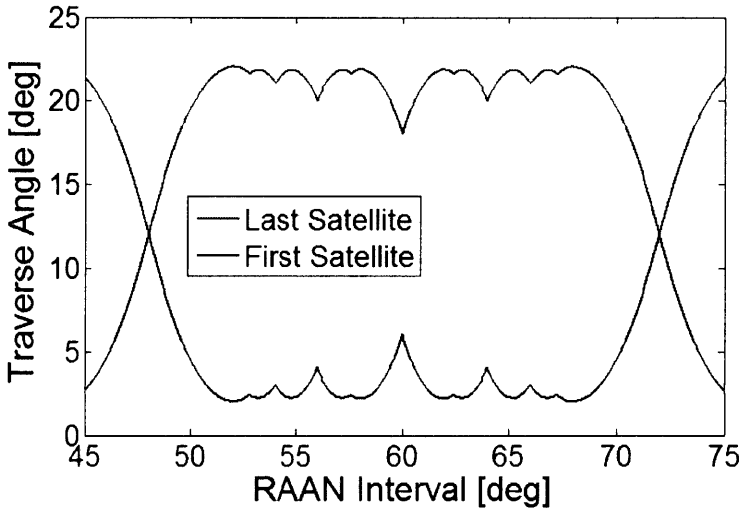

Figure 5-2: Geo-spatially Averaged Traverse Angle according to RAAN Interval between Orbit Planes (τ=15/1, 6 orbit planes)

The ReCon configuration in Table 5.1 was used to compare the performance of the normal Walker pattern and modified Walker patterns. This configuration is one of the design points on the Pareto front obtained by the adaptive weighted sum (AWS) method. There can be at large two approaches in modifying the normal Walker pattern: one for minimizing the reconfiguration time of the best-conditioned satellite (individual-oriented) and the other for minimizing the reconfiguration time of the worst-conditioned satellite (constellation-oriented). As can be seen in Table 5.2, modifying a normal Walker pattern by changing

$\Delta RAAN$ does not affect the GOM coverage and the ROM revisit time in this case. Although this is promising in reducing reconfiguration time, more investigation is required to verify whether this can be generalized for other ReCon configurations and target locations.

Table 5.1: Sample ReCon Configuration (from AWS)

Design Variable	Value
RGT ratio (altitude)	31/2 (450km)
Altitude difference	55.48km
Number of orbit planes	3
Number of sats per plane	2
Field of regard	44.00°

Table 5.2: Modified Walker Pattern Results

	Normal Walker	Worst-positioned Minimized	Best-positioned Minimized
$\Delta RAAN$	120.0°	116.1°	123.8°
Traverse angle of the worst-positioned satellite	17.44°	11.49°	19.34°
Traverse angle of the best-positioned satellite	5.69°	11.37°	3.85°
Reconfiguration time of the worst-positioned satellite	3.98 days	2.62 days	4.44 days
Reconfiguration time of the best-positioned satellite	1.30 days	2.59 days	0.88 days
GOM coverage	0.7822%	0.7822%	0.7822%
ROM revisit time	5513s	5513s	5511s

5.2 Sun-synchronous Orbit

The ReCon considered so far had an orbit that is not Sun-synchronous. The characteristics of a Sun-synchronous orbit were discussed in Chapter 2, and are summarized below in relation to the mission requirements.

- A Sun-synchronous orbit (SSO) provides uniform data of a specific location under consistent lighting conditions. However, it restricts the time of data collection, as can be seen in the "noon/midnight" orbit or the "dawn/twilight" orbit. If a phenomenon of interest occurs in the early morning and late in the afternoon

(patterns in coastal fog banks), it will be difficult to obtain enough data from Sun-synchronous satellites only. Many traditional Earth-observation platforms utilize this type of orbit.

- A non-Sun-synchronous orbit is used when a variety of illumination conditions are required for the purpose of Earth observation missions. The International Space Station (ISS) is in an orbit that is not Sun-synchronous, whose onboard observation equipment includes: window observational research facility, ISS agricultural camera, hyper-spectral imager for coastal oceans, and SERVIR environmental research and visualization system [79].

Sun-synchronous orbits have been popular in remote sensing satellites equipped with passive sensors that rely on illumination of the Sun. In fact, the orbits of some Earth-observation satellites combine the Sun-synchronous orbit and the repeating ground track orbit to generate a Sun-synchronous repeating ground track (SSRGT).

- A Sun-synchronous orbit crosses the equator (or any specific latitude) at the same local "solar" mean time.

- A repeating ground track orbit passes a certain location (or any combination of longitude and latitude) on the Earth at the same "nodal" time.

Therefore, an SSRGT is an orbit such that its node migrates at the same angular rate as the Earth's spin rate around the Sun (ω_{ES}). The derivation of SSRGT orbital elements is provided in Appendix D. A sample of possible circular SSRGT designs is plotted in Figure 5-3, where the altitude (radius minus the Earth radius) is a function of the ratio of the repeat cycle to the number of satellite periods (RGT ratio); Figure 5-4 is the 3-D plot with the inclination also included. In Figure 5-4, the points that correspond to circular SSRGTs form a subset of a curved surface, which represents the whole design space of general sun-synchronous orbits with the altitude now equal to the semi-major axis minus Earth radius.

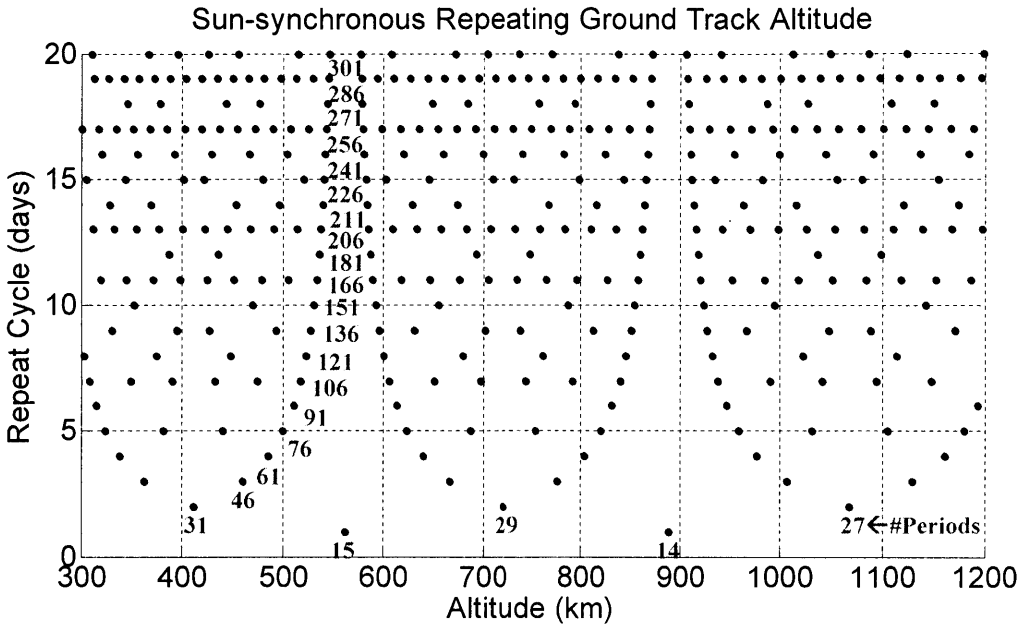

Figure 5-3: Sun-synchronous Repeating Ground Track Altitudes [74]

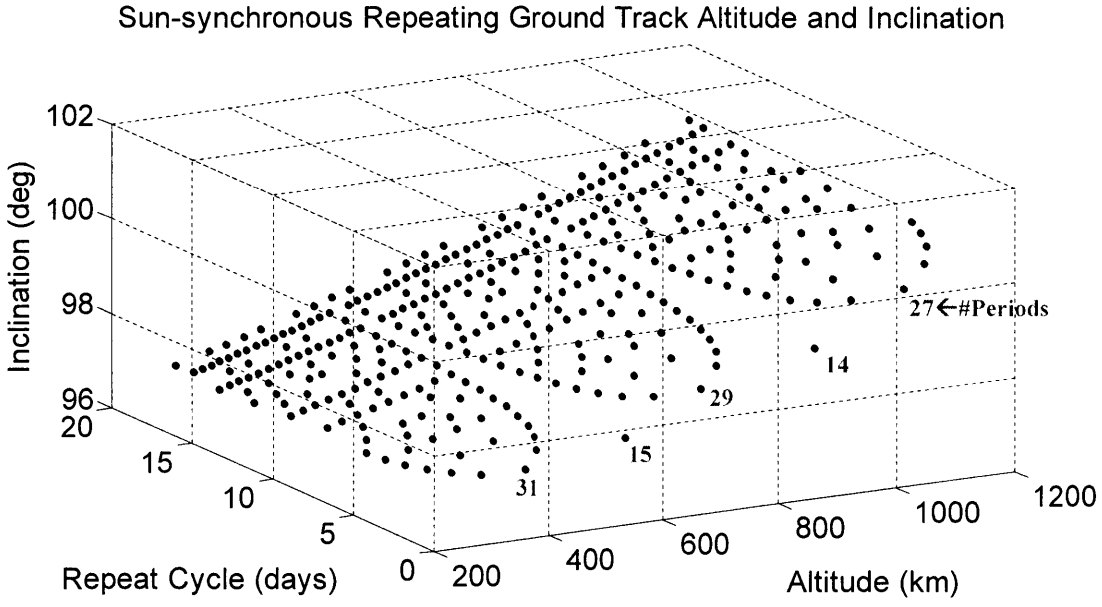

Figure 5-4: Sun-synchronous Repeating Ground Track Inclinations

Let us revisit Equation (2.18) for a general SSO to obtain insights about Sun-synchronous ReCon.

$$\dot{\Omega} = -\frac{3R_E^2 J_2 \sqrt{\mu_E}}{2a^{\frac{7}{2}}(1-e^2)^2}\cos(i) = \omega_{ES} \tag{5.1}$$

From the equation above, the following observations can be made:

O-1. ω_{ES} is a positive value, so inclination (i) must be greater than 90° to make its cosine negative and neutralize the minus sign on the left-hand side.

O-2. For a circular orbit (e=0), the semi-major axis (or radius) of an SSO is a single-variable function of inclination.

O-3. For an elliptical orbit (e≠0), the semi-major axis of an SSO is a function of inclination, and eccentricity. Compared to its circular counterpart in the same inclination the semi-major axis of an elliptical SSO always has a greater semi-major axis because $1 - e^2 < 0$.

Consider a Sun-synchronous ReCon whose ROM has a circular SSO, that is, a circular SSRGT orbit. The elliptical SSRGT for ROM is beyond the scope of this thesis because its altitude becomes well above LEO if we want to prevent the perigee drift by setting the orbit inclination to a critical angle of 116.6°. From the observations earlier, there are three possible choices for GOM when ROM has a circular SSRGT orbit:

C-1. Circular, non-Sun-synchronous orbit.
C-2. Circular, Sun-synchronous orbit with different inclination.
C-3. Non-circular (elliptical), Sun-synchronous orbit.

From O-2, there can be only a single value of altitude for a circular SSO. Therefore, if ROM already occupies that altitude, GOM cannot be both circular and sun-synchronous at the same time. This means that GOM has to give up either its Sun-synchronous characteristic (C-1) or its circular shape (C-3); when the GOM orbit is elliptical (C-3), its semi-major axis

must be greater than the GOM orbit radius due to O-3. Alternatively, the inclination can be changed (C-2), but this option is fuel-expensive. To recapitulate, a satellite in a circular SSRGT orbit in ROM cannot transfer to another circular Sun-synchronous orbit in GOM within the same orbit inclination.

In this case study, the first option is considered because the astrodynamics module cannot set up elliptical orbits using the Walker pattern generator in STK. The ROM orbit is assumed to be an SSRGT orbit with an RGT ratio of 29/2 and an inclination of 98.27°, which is the similar inclination value with those of the Earth observation constellations in Table 2.5. Using the simulated annealing (SA) method for single-objective optimization (SOO) with the fitness function in Equation (4.2), the following configuration and performance were obtained.

Table 5.3: Sun-synchronous ReCon Summary

Design Variables		**Parameters & Intermediate variables**		**Figures of Merit**	
RGT ratio	29/2	Inclination (Altitude)	98.27° (720km)	GOM Coverage	4.71%
Altitude Difference	-19.9km	Lifetime	5 years	ROM Revisit Time	1173s
# Orbit Planes	5	# Reconfigurations	10	Reconfiguration Time	13.6 days
# Satellites Per Plane	3	Ground Sample Distance	1m	Constellation Mass	41796kg
Field of Regard	41.4°	Aperture Diameter	1.52m	Satellite Mass	2786kg

This configuration has a total of 15 satellites, 3 satellites each in 5 orbit planes. The satellites are located at the RGT altitude of 720km in ROM and at the Walker altitude of 740km in GOM and (=720-(-20)) in GOM. To provide a 1m GSD with a FOV of 41.4°, the aperture diameter should be x m, resulting in a single satellite mass of 2786kg. The GOM coverage is 4.7% of the GOM period, the ROM revisit time is about 20 minutes, and the reconfiguration time is slightly less than two weeks. This reconfiguration time does not provide high responsiveness, but the design parameters can be tuned to improve the responsiveness. Also, the reconfiguration time of two weeks is still reasonable for observing natural phenomena (e.g. hurricanes in different parts of the world) that happen on a seasonal basis.

5.3 Small Satellite Implementations

"Small satellites," or "miniaturized satellites," refer to artificial satellites with small dimensions and low weights, usually fewer than 500 kilograms (1100 pounds) [80]. Small satellites can be categorized into minisatellites, microsatellites, nanosatellites, picosatellites, femtosatellites, and molecularsatellites, as illustrated in Figure 5-5 [80, 81, 82, 83, 84, 85, 86]. Small satellites have been a very active area of research – in particular, the CubeSat standard (1~4 kilograms) developed by California Polytechnic State University and Stanford University is widely used as a test bed as well as for educational purposes [87].

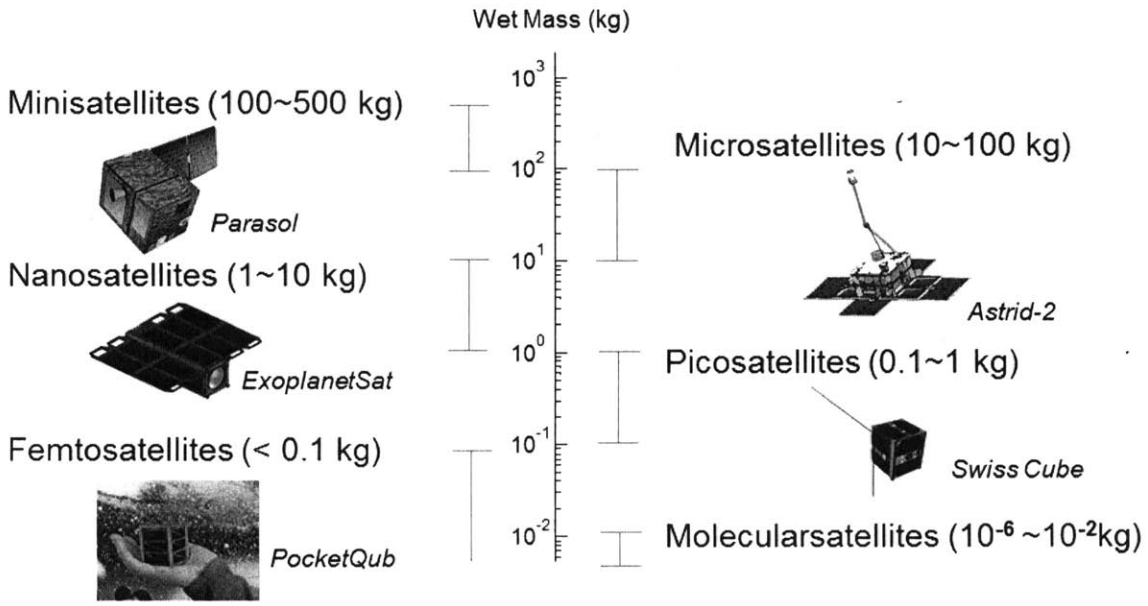

Figure 5-5: Classification of Small Satellites [80, 81, 82, 83, 84, 85, 86]

Small satellites can reduce the developing cost and manufacturing cost by utilizing commercial-off-the-shelf (COTS) components instead of space-rated components. Furthermore, launch cost can also be reduced if they are launched as secondary payloads. In this ReCon study, we want to minimize mass but also retain the propulsion capability at the same time, so our target is the lower region of minisatellites, whose maximum weight is approximately 182 kilograms (400 pounds), which is compatible with the EELV secondary payload adapter (ESPA) ring [88].

To minimize the satellite (constellation) mass, the adaptive weighted sum (AWS) method was used. In the fitness functions, the weightings for the performance and the system mass

were set to be zero and unity, respectively, to obtain an anchor point that minimizes the constellation mass. The ground sample distance (GSD) was also increased to 3m, which is still an acceptable resolution for commercial Earth observation satellites [89]. The genetic algorithm was used to generate a ReCon design with the lowest mass, which was then tuned to improve the performance. The optimization results of a ReCon with small satellites are provided below.

Table 5.4: Small Satellite ReCon Summary

Design Variables		**Parameters & Intermediate variables**		**Figures of Merit**	
RGT ratio	31/2	Inclination (Altitude)	60° (350km)	GOM Coverage	0.0057%
Altitude Difference	-30.0km	Lifetime	5 years	ROM Revisit Time	34548s
# Orbit Planes	2	# Reconfigurations	10	Reconfiguration Time	6.78 days
# Satellites Per Plane	1	Ground Sample Distance	3m	Constellation Mass	357kg
Field of Regard	10.0°	Aperture Diameter	0.136m	Satellite Mass	178kg

This configuration has two satellites, which is the lower boundary in design space. The RGT altitude in ROM also hits the lower boundary of 353km, and the Walker altitude in GOM is 383km (=353-(-30)). To provide a 3m GSD with a FOV of 10°, the aperture diameter and the single satellite mass should be 0.136m and 178kg, respectively, which are compatible with the dimensions and mass standards of the ESPA ring. The GOM coverage is 0.006% of the GOM period, the ROM revisit time is less than 10 hours. The reconfiguration is about a week.

5.4 Chapter Summary

This chapter explored the ReCon applications that meet specific mission requirements for Earth observations. First, one of the non-dominated ReCon designs obtained in multi-objective optimization was post-processed to further reduce the reconfiguration time by modifying the normal Walker pattern. Other two cases applied additional constraints, Sun-

synchronous orbits and the mass budget of small satellites, respectively. All these cases turned out to be feasible within the new ReCon framework, but further experimentation is needed to further validate and fine-tune the design solutions.

Chapter 6

Conclusions

This thesis has described the three-staged development cycle of a ReCon design framework: modeling, optimization, and applications. Through this effort, characteristics of optimal ReCon configurations could be identified. Feasibility of the ReCon under distinct mission scenarios has also demonstrated the flexibility and scalability of the ReCon framework. Each step of the ReCon framework development is revisited in this chapter to present the summary of findings made throughout this thesis and recommendations for future work.

6.1 Summary of Findings

This section summarizes the findings contributed by this thesis with respect to each stage of the ReCon development cycle.

6.1.1 Findings from ReCon Modeling

F-1 **RGT Altitude** - the repeating ground track (RGT) ratio and orbit inclination determine the RGT altitude; for a given RGT ratio, the RGT altitude increases as the orbit inclination increases under J_2 perturbations.

F-2 **Satellite Subsystem Mass vs. Optics Dimensions** - the optical payload mass has a slightly super-linear (exponent between 1.3 and 1.4) correlation with the optical aperture diameter. The non-payload bus mass has a nearly linear (exponent close to 1) correlation with the optical aperture diameter.

F-3 **Reconfiguration Time** - Reconfiguration time from GOM to ROM depends on the altitude of a baseline Walker constellation, the altitude difference, and the number of orbit planes.

6.1.2 Findings from ReCon Optimization

F-4 **Optimization Technique Performance** - gradient-based optimization techniques work poorly for the ReCon problem due to discrete variables, nonlinearity, and non-convexity. Heuristics are better suited for the ReCon problem in both single-objective optimization (SOO) and multi-objective optimization (MOO). In particular, a genetic algorithm produces a highly-optimal solution for the ReCon problem, but requires considerable amount of computation time. Simulated annealing produces a slightly less optimal solution, but requires much less computation time. Most of the computation time is spent in calculating the coverage and revisit time in Satellite Tool Kit (STK).

F-5 **Tuning Penalties for Constraint Violations** - in simulated annealing, using greater penalties (higher gains) on constraint violations helps to reach a more optimal solution faster. This tendency is not true for a genetic algorithm, however, where the optimality of solution is decreased when the penalty gain was either too high or too low.

F-6 **Optimal ReCon Configuration in SOO** - the optimal ReCon configuration obtained from SOO has a 450km Walker altitude in GOM and a 505km RGT altitude in ROM (RGT ratio of 15/1 with an altitude difference of -55km) given an inclination of 60°. A total of 10 satellites are distributed in 5 orbit planes, 2 satellites per each plane, and the field of regard (FoR) is 40°.

F-7 **Optimal ReCon Configuration in MOO** - along the Pareto front, the RGT altitude is 353km in the low-performance region (RGT ratio of 31/2) and gradually increases to 838km (RGT ratio 14/1) in the high-performance region. The number of satellites also rapidly increases, but the optimal configuration near the "knee" point has 3 satellites in 4 orbit planes, which has about the same number of satellites as in SOO. The RGT ratio has the greatest effects on both the constellation mass and the performance.

6.1.3 Findings from ReCon Case Studies

F-8 **Modified Walker Pattern** - redistributing the nodes of orbit planes over the range other than 360° can significantly reduce the reconfiguration time without significantly compromising the GOM coverage duration and ROM revisit time in some cases.

F-9 **Sun-synchronous RGT** - when the ROM orbit has a Sun-synchronous repeating ground track (SSRGT), additional constraints are imposed on the GOM.

- A satellite in a circular SSRGT orbit cannot transfer to another circular Sun-synchronous orbit in GOM within the same orbit inclination. There are three choices for the GOM configuration:
  (1) Circular, non-Sun-synchronous orbit
  (2) Circular, Sun-synchronous orbit with different inclination
  (3) Non-circular (elliptical), Sun-synchronous orbit
- If the GOM orbit is elliptical and Sun-synchronous, the altitude difference can only be positive due to physical constraints.

F-10 **Small Satellite Implementations** - It is feasible to implement a ReCon with small satellites. In particular, the satellite mass can be decreased as low as 180kg, compatible with ESPA rings, when the ground resolution requirement is relaxed to 3m.

6.2 Recommendations for Future Work

In this section, recommendations are made with respect to each stage of the ReCon development cycle based on the findings obtained earlier.

6.2.1 Recommendations for ReCon Modeling

R-1 **Multi-fidelity Model Integration** ***(From F-4)*** - Develop a medium-fidelity reduced model to replace STK in calculating the constellation performance for multi-fidelity optimization, where the medium-fidelity is continuously run in

MATLAB and the high-fidelity model is run in STK periodically to reduce computation time.

R-2 **Expansion of Deign Space** ***(From F-1, F-2, and F-3)*** - Expand the capabilities of the current ReCon framework to explore:

- A wider range of RGT ratios covering more repeat cycles
- More orbit options including elliptical orbits or high altitudes (MEO or beyond)
- Multi-layered constellations with differing satellite designs in each layer
- High-impulse propellants such as bipropellant or electric propulsion
- More maneuvering options such as a direct transfer or bi-elliptic transfer
- Other types of sensors such as microwave radiometer or synthetic aperture radar (SAR)

In particular, the Flower Constellations notation could be promising to formulate generalized constellations with elliptic orbits or/and non-uniform phases.

6.2.2 Recommendations for ReCon Optimization

R-3 **Fitness Function** ***(From F-6)*** - consult experts in the field regarding which figures of merit shall be included and what should be the scaling factors and weighting factors for each.

R-4 **Stated Deployment Strategy** ***(From F-7)*** - devise a method to locate optimal staged deployment paths in objective space.

6.2.3 Recommendations for ReCon Case Studies

R-5 **Modified Walker Pattern** ***(From F-8)*** - explore more in depth the possible impacts of the skewed node arrangement on the coverage duration and revisit time, while expanding the design space to heterogeneous node intervals.

R-6 **Sun-synchronous Constellation** ***(From F-9)*** – consider reconfiguration to a circular Sun-synchronous orbit in different inclinations or an elliptical Sun-synchronous orbits in the same inclination.

R-7 **Further Applications** – explore more case studies which include:

- Co-optimization of space-based assets (satellites) and air-based assets (UAVs)
- Placement of on-orbit fuel depots
- Space debris mitigation
- Planetary observation missions or interplanetary communication relays

Appendix A

Project Team Members

This project initiated as a non-funded research in November 2010 and was further developed during the Multidisciplinary System Optimization class (16.888/ESD77) at MIT in 2012 spring. The team members and the mentor are listed below.

Team Member	Role	Position	Institute
de Weck, Olivier L.	Mentor	Associate Professor	MIT
Legge, Robert S.	Team Member	Research Assistant	MIT
Paek, Sung Wook	Team Member	Research Assistant	MIT
Smith, Matthew W.	Team Member	Research Assistant	MIT

Appendix B

Reconfiguration Time Calculation Source Code

```
clc, clear, close all
numPlanes = 6; % the number of orbit planes
j=0;k=0;

t=(360/numPlanes-40):.1:(360/numPlanes+40);
% RAAN spacing [deg] between adjacent orbit planes
% Consider only the vicinity of 360/numPlanes + or - alpha
% to prevent the constellation from being skewed too much

ev = 0:.1:359; % the longitude of the target of interest [deg]

tau = 15.5; % RGT ratio
for event=ev % Loop1 : For every possible target location
  k = k+1;
  j = 0;
  for dist = t % Loop2: For every possible RAAN interval
    j=j+1;
    total = 0;
    max = 0;
    min = 360/tau;
    for i=0:(numPlanes-1) % Loop3: For each orbit plane

      traverse = mod(event-dist*i,360/tau);
      % Calculate traverse angle (lambda) from GOM to ROM

      if traverse==0
        traverse = 360/tau-traverse;
      end
      % If traverse angle is zero, we assume the worst case.
      % (the satellite in that plane have just missed the
      % reconfiguration opportunity, so it must wait for
      % the next alignment.
```

```
      total = total + traverse;

      if traverse>max
        max = traverse
      end

      if traverse<min && traverse>0
        min = traverse;
      end
      % Update total, maximum, and minimum traverse angles

    End % Loop3


  outtotal(j,k)=total;
  outmax(j,k)=max;
  outmin(j,k)=min;
  % Store in numPlane / targetLocation matrix

  End % Loop2
End % Loop1

for i=1:length(t)
    out1(i)=mean(outmin(i,:));
    out2(i)=mean(outmax(i,:));
end
%  Average over target longitudes
```

Appendix C

Non-dominated Sorting Genetic Algorithm-II Formulas

Crowding Distance Assignment

The crowding distance is assigned to each individual after the non-dominated sort is complete. The crowding distance is only meaningful when compared amongst individuals in the same front (rank), so this process is conducted front-wise.

- Step 1: Initialize the crowding distance of all individuals (d_j) in each front (F_i), to be zero.

$$F_i(d_j) = 0 \tag{C.1}$$

- Step 2: Sort the individuals in front F_i for each objective function f_m to obtain a sorted set I.

$$I = \text{sort}(F_i, f_m) \tag{C.2}$$

- Step 3: Assign an infinite distance to boundary values for each individual in the front F_i.

$$I(d_j) = \infty \tag{C.3}$$

- Step 4: Update the distance for $j = 2$ to n-1, where n is the number of individuals in the front F_i. In the equation below, $I(j).m$ is the value of the m^{th} objective function of the j^{th} individual in I.

$$I(d_j) = I(d_j) + \frac{I(j+1).m - I(j-1).m}{f_m^{max} - f_m^{min}} \tag{C.4}$$

Simulated Binary Crossover (SBX)

SBX simulates the binary crossover in nature with continuous variables. Two selected parents, p_1 and p_2, produce two children, c_1 and c_2, whose k-th variables are related by:

$$c_{1,k} = \frac{1}{2}[(1 - \beta_k)p_{1,k} + (1 + \beta_k)p_{2,k}]$$
$$c_{2,k} = \frac{1}{2}[(1 + \beta_k)p_{1,k} + (1 - \beta_k)p_{2,k}] \tag{C.5}$$

where β is obtained from a uniformly sampled random number, u, between 0 and 1, and the crossover distribution index, η_c.

$$\beta(u) = (2u)^{\frac{1}{\eta_c+1}}, \text{ if } u < 0.5$$
$$\beta(u) = \frac{1}{[2(1-u)]^{\frac{1}{\eta_c+1}}}, \text{ if } u \geq 0.5 \tag{C.6}$$

Polynomial Mutation

The polynomial mutation is governed by the following equation:

$$c_k = p_k + (p_k^u - p_k^l)\delta_k \tag{C.7}$$

where c_k is the child, p_k is the parent with an upper bound p_k^u and a lower bound p_k^l, and δ_k is a small variation calculated as follows from a uniformly sampled random number, r_k, between 0 and 1, and the mutation distribution index, η_m.

$$\delta_k = (2r_k)^{\frac{1}{\eta_m+1}} - 1, \text{ if } r_k < 0.5$$
$$\delta_k = 1 - [2(1 - r_k)]^{\frac{1}{\eta_m+1}}, \text{ if } r_k \geq 0.5 \tag{C.8}$$

Appendix D

Derivation of Sun-synchronous Repeating Ground Track Orbits

Letting the nodal precession rate from Equation (2.18) equal to the Earth's rotation rate around the Sun, or ω_{ES}=360° ÷ 365.2422day = 0.9856°/day,

$$\dot{\Omega} = -\frac{3R_E^2 J_2\sqrt{\mu_E}}{2a^{\frac{7}{2}}(1-e^2)^2}\cos(i) = \omega_{ES} \tag{D.1}$$

which can be expressed with respect to the cosine term as:

$$\cos(i) = -\frac{2\omega_{ES}a^{\frac{7}{2}}(1-e^2)^2}{3R_E^2 J_2\sqrt{\mu_E}\omega_{ES}} \tag{D.2}$$

After substituting Equation (D.2) into each variable in Equation (2.13) and substituting the variables again into Equation (2.14),

$$f(a) = \sqrt{\frac{\mu_E}{a^3}} + \frac{3}{4}\frac{J_2R_E^2\sqrt{\mu_E}}{2a^{\frac{7}{2}}}\left(\frac{4}{3}\frac{a^7\omega_{ES}^2}{J_2^2R_E^4\mu_E} - 1\right) + \frac{3}{4}\frac{J_2R_E^2\sqrt{\mu_E}}{2a^{7/2}}\left(\frac{20}{9}\frac{a^7\omega_{ES}^2}{J_2^2R_E^4\mu_E} - 1\right) - \omega_E\tau + \omega_{ES}\tau \tag{D.3}$$

if a circular orbit is assumed ($e = 0$). Differentiating the equation above,

$$f'(a) = \frac{-18J_2R_E^2\mu_E a^2 + 112a^7\omega_{ES}^2 + 63J_2^2R_E^4\mu_E}{12J_2R_E^2\sqrt{\mu_E a^9}} \tag{D.4}$$

Thus, the semi-major axis of a circular SSRGT (a) can be calculated via the Newton-Raphson method once the RGT ratio (τ) is given, from which the orbit inclination can be also calculated. For a more general case when the orbit is no longer circular (non-zero eccentricity), the function and its derivative are given in Equations (D.5) and (D.6).

$$f(a) = \sqrt{\frac{\mu_E}{a^3}} + \frac{3}{4}\frac{J_2 R_E^2 \sqrt{\mu_E}}{a^{\frac{7}{2}}(1-e^2)^{\frac{3}{2}}}\left(\frac{4}{3}\frac{a^7 \omega_{ES}^2 (1-e^2)^4}{J_2^2 R_E^4 \mu_E} - 1\right) + \frac{3}{4}\frac{J_2 R_E^2 \sqrt{\mu_E}}{2a^{\frac{7}{2}}(1-e^2)^2}\left(\frac{20}{9}\frac{a^7 \omega_{ES}^2 (1-e^2)^4}{J_2^2 R_E^4 \mu_E} - 1\right) \quad \text{(D.5)}$$

$$f'(a) = -\frac{3}{2}\sqrt{\frac{\mu_E}{a^5}} - \frac{21}{8}\frac{J_2 R_E^2 \sqrt{\mu_E}}{a^{\frac{9}{2}}(1-e^2)^{\frac{3}{2}}}\left(\frac{4}{3}\frac{a^7 \omega_{ES}^2 (1-e^2)^4}{J_2^2 R_E^4 \mu_E} - 1\right) - \frac{21}{8}\frac{J_2 R_E^2 \sqrt{\mu_E}}{a^{\frac{9}{2}}(1-e^2)^{\frac{3}{2}}}\left(\frac{20}{9}\frac{a^7 \omega_{ES}^2 (1-e^2)^4}{J_2^2 R_E^4 \mu_E} - 1\right)$$
$$+ \frac{7(1-e^2)^{\frac{5}{2}}\omega_{ES}^2}{J_2 R_E^2 \mu_E}\sqrt{\frac{a^5}{\mu_E}} + \frac{35(1-e^2)^2 \omega_{ES}^2}{3J_2 R_E^2 \mu_E}\sqrt{\frac{a^5}{\mu_E}} \quad \text{(D.6)}$$

References

[1] Aggarwal, S., 2004, Principles of Remote Sensing. In. Sivakumar, M.V.K., Roy, P.S., Harsen, K., and Saha, S.K. (eds.), "Satellite Remote Sensing and GIS Applications in Agricultural Meteorology," World Meteorological Organization, Geneva., pp. 23-38.

[2] Wikipedia, 2012, "Remote sensing," Wikimedia Foundation, Inc., [Online], URL: http://en.wikipedia.org/wiki/Remote_sensing [Cited: February 14th, 2012].

[3] Bogosian, R., 2008, "Image Collection Optimization in the Design and Operation of Lightweight, Low Areal-Density Space Telescopes," Massachusetts Institute of Technology, Dept. of Aeronautics and Astronautics.

[4] Satellite Tool Kit 9.2.3, 2010, Analytical Graphics Inc.

[5] NASA, 2012, "The Afternoon Constellation," [Online], URL: http://atrain.nasa.gov/images.php [Cited: May 16th, 2012].

[6] MATLAB 2010a, 2010, The MathWorks, Inc.

[7] Wikipedia, 2012, "Kepler Orbit," Wikimedia Foundation, Inc., [Online], URL: http://en.wikipedia.org/wiki/Kepler_orbit [Cited: April 21st, 2012].

[8] Wertz, J. R, 2001, "Mission Geometry: Orbit and Constellation Design and Management," El Segundo, CA: Microcosm Press, 2001.

[9] The Encyclopedia of Earth, "Northern Hemisphere," [Online], URL: http://www.eoearth.org/article/Northern_Hemisphere [Cited: April 21st, 2012].

[10] Do, S., 2007, "Relative Orbital Positioning and Maintenance for a Minimal Delay Line Multiple Spacecraft Interferometer," Undergraduate Thesis, University of Sydney.

[11] Muller, M., 1995, "Equation of Time – Problem in Astronomy," Acta Phys. Pol. A 88 Supplement, S-49.

[12] Feinstein, S. A., and McLaughlin, C. A., 2006, "Dynamic discretization method for solving Kepler's equation," Celest. Mech. Dyn. Astron. 96, pp. 49–62.

[13] Wertz, J. R., Everett, D. F., and Puschell, "Space Mission Engineering: The New SMAD," El Segundo, CA: Microcosm Press, 2010.

[14] Wikipedia, 2012, "Keplerian Elements," Wikimedia Foundation, Inc., [Online], URL: http://ja.wikipedia.org/wiki/人工衛星の軌道要素 [Cited: April 21st, 2012].

[15] Wikipedia, 2012, "Ground Track," Wikimedia Foundation, Inc., [Online], URL: http://en.wikipedia.org/wiki/Ground_track [Cited: April 21st, 2012].

[16] Wilkins, M., Bruccoleri, C., and Mortari, D., 2003, "The Flower Constellations," Paper AAS 03-274 of the John L. Junkins Astrodynamics Symposium, Texas A&M University, College Station, TX.

[17] Boain, R. J., 2005, "A-B-Cs of Sun-synchronous orbit mission design (AAS 04-108)," in Spaceflight Mechanics 2004—Part I., edited by S. L. Coffey et al., pp. 85–104, Univelt, Inc., San Diego, Calif.

[18] POSITIM, 2012, "Global Navigation Satelite Systems," [Online], URL: http://www.positim.com/navsys_overview.html [Cited: April 21st, 2012].

[19] Vallado, D. A., 2007, "Fundamentals of Astrodynamics and Applications," 3rd ed., Space Technology Library, ed. J.R. Wertz., NY: Microcosm Press.

[20] Wagner, C., 1991, "A Prograde Geosat Exact Repeat Mission?" J Astronaut. Sci, **39**(3): pp. 316–326.

[21] Wikipedia, 2012, "Sun-synchronous Orbit," Wikimedia Foundation, Inc., [Online], URL: http://en.wikipedia.org/wiki/Sun_synchronous [Cited: April 21st, 2012].

[22] NASA, 2012, "Seasonal Illumination Variations, " [Online], URL: http://landsat.gsfc.nasa.gov/images/seasons.html [Cited: March 20th, 2012].

[23] eoPortal, 2012, "SNOE (Student Nitric Oxide Explorer)," [Online], URL: http://www.eoportal.org/directory/pres_SNOEStudentNitricOxideExplorer.html [Cited: May 20th, 2012].

[24] Wikipedia, 2012, "Satellite Constellations," [Online], URL: http://en.wikipedia.org/wiki/Satellite_constellation. [Cited: March 3rd, 2012].

[25] Hu, Y. F., Maral, G. and Ferro, E., 2002, "Service Efficient Network Interconnection Via Satellite," John Wiley & Sons.

[26] Wikipedia, 2012, "InmarSat," Wikimedia Foundation, Inc., [Online], URL: http://en.wikipedia.org/wiki/Inmarsat [Cited: April 21st, 2012].

[27] Inmarsat plc., 2012, "Maritime Fleet 77 55 33 Services," [Online], URL: http://www.inmarsat.com/Support/Coverage/Fleet_77_55_33.aspx?language=EN&textonly=False [Cited: April 21st, 2012].

[28] Nguyen, H. N., 2002, "Routing and Quality-of-Service in Broadband LEO Satellite Networks," Springer; 1st edition.

[29] World Map, 2012, "Map Pictures," World Map, [Online], URL: http://www.wpmap.org/category/world-maps [Cited: April 21st, 2012].

[30] Adams, W. S., and Lang, T. J., 1998, "Mission Design and Implementation of Satellite Constellations," International Astronautical Federation, pp. 51–62 (Chapter 1.4).

[31] Turner, A. E., 2002, "Constellation Design Using Walker Patterns," AIAA 2002-4904, Space Systems/Loral.

[32] Lang, T. J., 1993, "Optimal Low Earth Orbit Constellations for Continuous Global Coverage," AAS 93-597.

[33] Wikipedia, 2012, "Molniya Orbit," Wikimedia Foundation, Inc., [Online], URL: http://en.wikipedia.org/wiki/Molniya_orbit [Cited: April 21st, 2012].

[34] Wikipedia, 2012, "QZSS," Wikimedia Foundation, Inc., [Online], URL: http://en.wikipedia.org/wiki/File:Qzss-45-0.09.jpg [Cited: April 21st, 2012].

[35] Draim, J. E., and Castiel, D., 1997, "Optimization of the Borealistm™ and Concordiatm™ Sub-constellations of the Ellipso Personal Communications System," Acta Astronautica, **40**(2-8) pp. 183-193.

[36] Draim, J. E., Cefola, P. J., and Ernandes, K. J., 2007, "Seamless Handovers in Cobra Teardrop Satellite," Acta Astronautica, **61**(1-6) pp. 139-150.

[37] Wertz, J. R., 2005, "Coverage, Responsiveness, and Accessibility for Various Responsive Orbits," RS3-2005-2002, 3rd Responsive Space Conference, Los Angeles, CA.

[38] Ruggieri, M. et al., 2008, "The Flower Constellation Set and its Possible Applications," ESA Advanced Concept Team Final Report.

[39] Avendaño, M. E., Davis, J. J., and Mortari, D., 2010, "The Lattice Theory of Flower Constellations," AAS 10-172, 20th AAS/AIAA Space Flight Mechanics Meeting, San Diego, CA.

[40] Globalcom Satellite Communications, 2012, "LEO vs. GEO Satellites when used with Mobile Satellite Services," [Online], URL: http://www.globalcomsatphone.com/leo_geo.html [Cited: May 16th, 2012].

[41] Gunter, 2012, "Orbcomm (2nd gen.)," Gunter's Space Page, [Online], http://space.skyrocket.de/doc_sdat/orbcomm-2.htm [Cited: May 16th, 2012].

[42] Wikipedia, 2012, "Iridium Satellite Constellation," Wikimedia Foundation, Inc., [Online], URL: http://en.wikipedia.org/wiki/Iridium_satellite_constellation [Cited: April 22nd, 2012].

[43] Globalcom Satellite Communications, 2012, "How the Iridium Phone Works," [Online], URL: http://www.globalcomsatphone.com/iridium/info.html [Cited: May 16th, 2012].

[44] NASA, 2008, "TDRSS System Description," [Online], https://www.spacecomm.nasa.gov/spacecomm/programs/tdrss/system_description.cfm [Cited: May 22nd, 2012].

[45] Wikipedia, 2012, "Satellite Navigation," Wikimedia Foundation, Inc., [Online], URL: http://en.wikipedia.org/wiki/Satellite_navigation [Cited: April 22nd, 2012].

[46] Encyclopedia Astronautica, 2012, "GPS Block 2R," [Online], URL: http://www.astronautix.com/craft/gpsock2r.htm [Cited: May 16th, 2012].

[47] Sistemilaser, 2012, "GLONASS System," [Online], URL: http://www.glonass.it/eng glonass-story.aspx [Cited: May 16th, 2012].

[48] Wikipedia, 2012, "Beidou Navigation System," Wikimedia Foundation, Inc., [Online], URL: http://en.wikipedia.org/wiki/Beidou_navigation_system [Cited: April 21st, 2012].

[49] ESA Navigation, 2012, "Galileo System," European Space Agency, [Online], URL: http://www.esa.int/esaNA/SEM5K8W797E_galileo_2.html [Cited: May 19th, 2012].

[50] Wikipedia, 2012, "A-train (satellite constellation)," Wikimedia Foundation, Inc., [Online], URL: http://en.wikipedia.org/wiki/A-train_(satellite_constellation) [Cited: May19th, 2012].

[51] Imre, E., Kormos, T., and Palmer, P., 2004, "Orbit Acquisition of the Disaster Monitoring Constellation – Preliminary Results," IFAC *Automatic Control in Aerospace*, pp. 215-221.

[52] Wikipedia, 2012, "RapidEye," Wikimedia Foundation, Inc., [Online], URL: http://en.wikipedia.org/wiki/RapidEye [Cited: May 17th, 2012].

[53] Wikipedia, 2012, "KH-11 Kennan," Wikimedia Foundation, Inc., [Online], URL: http://en.wikipedia.org/wiki/KH-11_Kennan [Cited: May 17th, 2012].

[54] de Weck, O. L., Scialom, U., and Siddiqi, A., 2008, "Optimal Reconfiguration of Satellite Constellations with the Auction Algorithm," *Acta Astronautica*, **62**(2–3) pp. 112–130.

[55] de Weck, O. L., de Neufville, R., and Chaize, M., 2004, "Staged deployment of communications satellite constellations in low Earth orbit," J Aerospace Cmput Inform Commun, **1**(4) pp. 119–136.

[56] Veterans Today, 2012, [Online], URL: http://www.veteranstoday.com/2012/01/19 [Cited: May 20th, 2012].

[57] Wikipedia, 2012, "Ground sample distance," Wikimedia Foundation, Inc., [Online], URL: http://en.wikipedia.org/wiki/Ground_sample_distance [Cited: April 28th, 2012].

[58] Wikipedia, 2012, "Airy Disk," Wikimedia Foundation, Inc., [Online], URL: http://en.wikipedia.org/wiki/Airy_disk [Cited: April 28th, 2012].

[59] eoPortal, 2012, "eoPortal: sharing earth observation resources," [Online], URL: http://www.eoportal.org/ [Cited: May 20th, 2012].

[60] Phillips, L., 2002, "Micro Arcsecond Xray Imaging Mission: Pathfinder (MAXIM-PF) – Launch Vehicle Information," NASA Goddard Space Flight Center, Internal Slides Package.

[61] SpaceX, 2008, "Falcon 1 Launch Vehicle Payload User's Guide Rev7," Space Exploration Technologies Corporation.

[62] Thomas, S. J., Mueller, J. B., Paluszek, M., 2004, "Formations for Close-Orbiting Escort Vehicles," AIAA 2004-6289, AIAA 1st Intelligent Systems Technical Conference, Chicago, IL..

[63] Alliance Space Systems, Inc. – Commerce, 2012, "Tank Data Sheets," Alliant Techsystems Inc., [Online], URL: http://www.psi-pci.com/Data_Sheets1_main.htm [Cited: May 17th, 2012].

[64] Worthington Cylinders, 2012, "SCI Standard Cylinders," [Online], URL: http://www.worthingtoncylinders.com/Products/composite-cylinders/SCI-Standard.aspx [Cited: May 17th, 2012].

[65] HyPerComp Engineering Inc., 2012, "Product Examples," HyPerComp Engineering Inc. [Online], URL: http ://www .hypercompeng.com/products.html [Cited: May 17th, 2012].

[66] Astrium, 2012, "EADS Astrium GmbH - Space Propulsion Product Brochures," EADS, [Online], URL: http://cs.astrium.eads.net/sp/brochures/index.html [Cited: May 17th, 2012].

[67] Curiel, A. S., 2003, "Small Satellites in Constellation - Constraints," Surrey Satellite Technology Ltd., Internal Slides Package.

[68] Wikipedia, 2012, "Matrix multiplication," Wikimedia Foundation, Inc., [Online], URL: http://en.wikipedia.org/wiki/Matrix_multiplication [Cited: May 22nd, 2012].

[69] Wikipedia, 2012, "Latin hypercube sampling," Wikimedia Foundation, Inc., [Online], URL: http://en.wikipedia.org/wiki/Latin_hypercube_sampling [Cited: May 13th, 2012].

[70] Wikipedia, 2012, "Metaheuristic," Wikimedia Foundation, Inc., [Online], URL: http://en.wikipedia.org/wiki/Metaheuristic [Cited: April 21st, 2012].

[71] Fang, H.-L., Ross, P., and Come, D., 1993, "A promising Genetic Algorithm approach to job-shop scheduling, rescheduling, and open-shop scheduling problems," in Proceedings of the Fifth International Conference on Genetic Algorithms, ed., S. Forrest, pp. 375-382, San Mateo: Morgan Kaufmann.

[72] Wikipedia, 2012, "Simulated annealing," Wikimedia Foundation, Inc., [Online], URL: http://en.wikipedia.org/wiki/Simulated_annealing [Cited: May 13th, 2012].

[73] Cohanim, B. E., Hewitt, J. N., and de Weck, O. L., 2004, "The Design of Radio Telescope Array Configurations using Multiobjective Optimization: Imaging Performance versus Cable Length," The Astrophysical Journal, Supplement Series, Vol. 154: pp. 705-719.

[74] MIT, "16.888/ESD.77 Multidisciplinary System Design Optimization," [Online], URL: http://stellar.mit.edu/S/course/16/sp12/16.888/ [Cited: May 19th, 2012].

[75] Goldberg, D. E., 1989, "Genetic Algorithms in Search, Optimization & Machine Learning. Reading", MA: Addison-Wesley.

[76] Wikipedia, 2012, "Convex combination," Wikimedia Foundation, Inc., [Online], URL: http://en.wikipedia.org/wiki/Convex_combination [Cited: May 13th, 2012].

[77] Fonseca, K. C. M. and Fleming, P. J., 1993, "Genetic algorithms for multiobjective optimiza-tion: Formulation, discussion and generalization," in Proceedings of the Fifth International Conference on Genetic Algorithms, S. Forrest, Ed. San Mateo, CA: Morgan Kauffman, pp. 416–423.

[78] Deb, K., Agrawal, S., Pratab, A., and Meyarivan. T., 2002, "A fast elitist nondominated sorting genetic algorithm for multi-objective optimization: NSGA-II," in Proc. Parallel Problem Solving From Nature VI Conf., pp. 849–858.

[79] NASA, 2012, "Earth Remote Sensing From the Space Station - It's Not Just Handheld Cameras Anymore," [Online], URL: http://www.nasa.gov/mission_pages/station/research/benefits/remote_sensing.html [Cited: May 13th, 2012].

[80] Wikipedia, 2012, "Miniaturized satellites," Wikimedia Foundation, Inc., [Online], URL: http://en.wikipedia.org/wiki/Miniaturized_satellite [Cited: May 17th, 2012].

[81] Tristancho, J., 2012, " Implementation of a femto-satellite and a mini-launcher," Master Thesis, Universitat Politècnica de Catalunya.

[82] CNES, 2012, "PARASOL," Centre National d'Études Spatiales, [Online], URL: http://smsc.cnes.fr/PARASOL/GP_satellite.htm [Cited: May 17th, 2012].

[83] Alfvén Laboratory, 2012, "The Astrid-2 Satellite," Royal Institute of Technology (KTH), [Online], URL: http://www.spp.ee.kth.se/res/tools/astrid-2/ [Cited: May 17th, 2012].

[84] Seager, S., 2012, "Exoplanet Space Missions," Massachusetts Institute of Technology, [Online], URL: http://seagerexoplanets.mit.edu/exoplanet.htm [Cited: May 17th, 2012].

[85] Swiss Space Center, 2012, "4th ESRD: 40th Anniversary of the First Moon Landing," Ecole Polytechnique Fédérale de Lausanne (EPFL), [Online], URL: http://space.epfl.ch /page-39470-en.html [Cited: May 17th, 2012].

[86] Stephenson, H., 2012, "The Next Big Thing is Small," NASA, [Online], URL: http:// www.nasa.gov/offices/oce/appel/ask/issues/38/38s_next_prt.htm [Cited: May 17th, 2012.

[87] California Polytechnic State University, 2009, "CubeSat Design Specification," Rev. 12.

[88] Department of Defense, 2001, "DoD Space Test Program - Secondary Payload Planner's Guide for Use on the EELV Secondary Payload Adapter," Ver.1.0.

[89] Jacobsen, K., 2005, "High resolution imaging satellite systems," EARSeL Workshop on remote sensing use of the third dimension for remote sensing purposes, Porto, Portugal.